

# Runaway Stars in the Galactic Halo: Their Origin and Kinematics

---

MANUEL DUARTE DE VASCONCELOS SILVA

---

*Centre for Astrophysics Research  
Science & Technology Research Institute  
Department of Physics, Astronomy and Mathematics  
· University of Hertfordshire ·*

Thesis submitted to the University of Hertfordshire in partial  
fulfilment of the requirements  
of the Degree of Doctor of Philosophy

· June 2011 ·



## Abstract

Star formation in the Milky Way is confined to star-forming regions (OB association, HII regions, and open clusters) in the Galactic plane. It is usually assumed that these regions are found preferably along spiral arms, as is observed in other spiral galaxies. However, young early-type stars are often found at high Galactic latitudes, far away from their birthplaces in the Galactic disc. These stars are called *runaway* stars, and it is believed that they were ejected from their birthplaces early in their lifetimes by one of two mechanisms: ejection from a binary system following the destruction of the massive companion in a supernova type II event (the binary ejection mechanism), or ejection from a dense cluster following a close gravitational encounter between two close binaries (the dynamical ejection mechanism).

The aims of our study were: to improve the current understanding of the nature of high Galactic latitude runaway stars, in particular by investigating whether the theoretical ejection mechanisms could explain the more extreme cases; to show the feasibility of using high Galactic latitude stars as tracers of the spiral arms. The main technique used in this investigation was the tracing of stellar orbits back in time, given their present positions and velocities in 3D space. This technique allowed the determination of the ejection velocities, flight times and birthplaces of a sample of runaway stars. In order to obtain reasonable velocity estimates several recent catalogues of proper motion data were used.

We found that the evolutionary ages of the vast majority of runaway stars is consistent with the disc ejection scenario. However, we identified three outliers which would need flight times much larger than their estimated ages in order to reach their present positions in the sky. Moreover, the ejection velocity distribution appears to be bimodal, showing evidence for two populations of runaway stars: a “low” velocity population (89 per cent of the sample), with a maximum ejection velocity of about  $300 \text{ km s}^{-1}$ , and a “high” velocity population, with ejection velocities of  $400 - 500 \text{ km s}^{-1}$ . We argue that the observed bimodality and maximum ejection velocity of  $\sim 500 \text{ km s}^{-1}$  can be interpreted as a natural consequence of a variation of the binary ejection mechanism. A possible connection between the “high” velocity population and the so-called *hypervelocity* stars is also explored, resulting in the conclusion that some stars previously identified as hypervelocity may be in fact runaway stars.

The feasibility of using stars as tracers of the spiral arms was tested on a local sample, in order to obtain better quality data and larger numbers. We found that the spiral arms pattern speeds estimated from this sample ( $24.9 \pm 5.2 \text{ km s}^{-1} \text{ kpc}^{-1}$ ) and from a selected sample of runaways ( $22.8 \pm 7.8 \text{ km s}^{-1} \text{ kpc}^{-1}$ ) are consistent within the errors and also consistent with other published estimates. We concluded that our estimates combined with the ones obtained in other studies suggest a value in the range  $20 - 25 \text{ km s}^{-1} \text{ kpc}^{-1}$  for the pattern speed. Moreover, we concluded that an adequate representation of the spiral arms is obtained given the former pattern speed estimate, even when applied to the sample of runaway stars.



*We are to admit no more causes of natural things than such as are both true and sufficient to explain their appearances.*

Sir Isaac Newton - *Philosophiae Naturalis Principia Mathematica* (1687)

*I tell you: one must still have chaos within oneself, to give birth to a dancing star.*

Friedrich Wilhelm Nietzsche - *Thus Spoke Zarathustra* (1885)



# Acknowledgments

This dissertation would not have been possible without the support, guidance and help of many people for whom I would like to express my gratitude.

I am extremely grateful to the University of Hertfordshire, and in particular to Prof. James Hough, former director of the Centre for Astrophysics Research, for offering me a STFC-equivalent studentship.

I would like to show my gratitude to my principal supervisor Dr. Ralf Napiwotzki for his continuous interest, guidance and support, until the very end. The many discussions on several Astrophysical topics were particularly helpful.

I would also like to thank my second supervisor Prof. Elias Brinks for helpful comments and being always available when I needed.

I am grateful to all my colleagues within the Centre for Astrophysics Research for the great atmosphere. I am especially indebted to Kieran Forde for being not only a good colleague but also a good friend whose help and encouragement in time of need I will never forget. I would like to thank Roberto Raddi and the rest of the Horsa Gardens “team” for their help and hospitality.

My deepest gratitude goes to João Neves and Ana Neves, Pedro Ferreira and Carla Gonçalves, and João Sousa for their hospitality and friendship.

I am also grateful to my *fiancée* Vânia Lima for her undying support and encouragement. Finally, I thank my parents for supporting me throughout all my studies at University and for providing a home in which to complete my writing up.

This research has made use of data obtained from the SuperCOSMOS Science Archive, prepared and hosted by the Wide Field Astronomy Unit, Institute for Astronomy, University of Edinburgh, which is funded by the UK Science and Technology Facilities Council. This research has made use of NASA’s Astrophysics Data System and of the SIMBAD database, operated at CDS, Strasbourg, France.



# Contents

<b>1</b>	<b>Runaway stars and the Milky Way</b>	<b>1</b>
1.1	Introduction . . . . .	1
1.2	Outline of the dissertation . . . . .	5
<b>2</b>	<b>The Milky Way</b>	<b>7</b>
2.1	Morphology . . . . .	7
2.2	The spiral arms . . . . .	8
<b>3</b>	<b>Early-type stars and runaway stars</b>	<b>13</b>
3.1	Overview . . . . .	13
3.2	Stellar evolution . . . . .	13
3.3	Observational properties . . . . .	16
3.4	High Galactic latitude runaway stars . . . . .	17
3.4.1	Definition and history . . . . .	17
3.4.2	Ejection mechanisms . . . . .	18
3.4.3	Hypervelocity stars . . . . .	19
<b>4</b>	<b>Dynamics in a gravitational potential</b>	<b>21</b>
4.1	Gravitational potential for spherical and cylindrical geometry . . . . .	21
4.1.1	Circular speed and perpendicular force . . . . .	22
4.1.2	Examples of systems with spherical geometry . . . . .	24

4.1.3	Examples of systems with cylindrical geometry . . . . .	25
4.2	The Milky Way gravitational potential . . . . .	26
4.2.1	Observational constraints . . . . .	28
4.2.2	Scale lengths . . . . .	30
4.2.3	Gravitational potential model . . . . .	30
<b>5</b>	<b>Orbit determination</b>	<b>37</b>
5.1	High Galactic latitude runaway stars . . . . .	37
5.1.1	Sample selection . . . . .	37
5.1.2	Abundances . . . . .	38
5.1.3	Temperature and surface gravity . . . . .	41
5.1.4	Projected rotation velocity . . . . .	42
5.1.5	Evolutionary status . . . . .	44
5.1.6	Age and mass . . . . .	45
5.1.7	Positions, distances and radial velocities . . . . .	47
5.1.8	Proper motions . . . . .	48
5.1.9	Full space coordinates and velocities . . . . .	52
5.2	Orbital analysis . . . . .	52
<b>6</b>	<b>Properties of the population of runaway stars</b>	<b>57</b>
6.1	Results . . . . .	57
6.1.1	Flight times . . . . .	57
6.1.2	Ejection velocities . . . . .	62
6.2	Birthplaces . . . . .	63
6.3	Discussion . . . . .	65
6.3.1	Influence of the gravitational potential . . . . .	65
6.3.2	Comparison with other studies . . . . .	66
6.3.3	The link with hypervelocity stars . . . . .	68

<b>7</b>	<b>Tracing the spiral arms</b>	<b>71</b>
7.1	Introduction . . . . .	71
7.2	The Hipparcos sample . . . . .	72
7.2.1	Sample selection . . . . .	72
7.2.2	Lutz-Kelker bias . . . . .	74
7.2.3	Bolometric and reddening corrections . . . . .	75
7.2.4	Ages . . . . .	77
7.3	Pattern speed determination . . . . .	77
7.3.1	Effect of age uncertainty . . . . .	80
<b>8</b>	<b>Spiral arms and pattern speed</b>	<b>83</b>
8.1	Results . . . . .	83
8.2	Discussion . . . . .	86
8.2.1	Large scale structure and small scale substructures . . . . .	86
8.2.2	Corotation radius . . . . .	88
8.2.3	Error associated with age determination . . . . .	89
8.3	Comparison with a simulated sample . . . . .	90
8.3.1	The simulation . . . . .	90
8.3.2	Simulation results and discussion . . . . .	93
<b>9</b>	<b>Summary and conclusions</b>	<b>97</b>
9.1	Summary . . . . .	97
9.2	Main results and conclusions . . . . .	98
9.3	The future . . . . .	100
9.3.1	Simulation of a population of runaway stars . . . . .	100
9.3.2	Runaway stars in nearby galaxies . . . . .	100
9.3.3	Gaia catalogue of runaway stars . . . . .	101
<b>A</b>	<b>Data for main sequence stars</b>	<b>103</b>



# List of Figures

1.1	Bayeux tapestry: appearance of Halley comet recorded. . . . .	2
1.2	M31 (Andromeda) galaxy image taken by GALEX. . . . .	3
2.1	M51 galaxy image taken by Hubble’s ACS instrument. . . . .	9
2.2	Kinematic density waves. . . . .	10
2.3	Spiral arms. . . . .	11
3.1	Post-HB evolution. . . . .	16
4.1	Rotation curve of Allen and Santillan (1991) model with shorter scale length. . . . .	31
4.2	Preliminary study of the sensitivity of the circular speed curve to the second disc component parameters. . . . .	32
4.3	Plot of the circular velocity. . . . .	34
4.4	Density contours of the updated model. . . . .	35
5.1	$T_{\text{eff}} - \log g$ diagram of the runaway stars sample. . . . .	42
5.2	Interpolation in the $T_{\text{eff}} - \log g$ plane. . . . .	45
5.3	Ages from different theoretical models compared. . . . .	46
5.4	Extinction and distance determination methods. . . . .	48
5.5	Plots comparing the proper motion estimates from Hipparcos and Tycho-2 catalogues. . . . .	49

5.6	Plots comparing the proper motion estimates from Hipparcos and UCAC 2 catalogues. . . . .	49
5.7	Plots comparing the proper motion estimates from Hipparcos and USNO-B catalogues. . . . .	50
5.8	Plots comparing the proper motion estimates from Hipparcos and Supercosmos catalogues ( $V = 5, \dots, 11$ ). . . . .	50
5.9	Plots comparing the proper motion estimates from UCAC 2 and Supercosmos catalogues, for stars fainter than $V = 14$ . . . . .	50
5.10	Flowchart of the orbit determination method. . . . .	54
6.1	Plot of flight times vs. evolutionary ages of runaway stars – I. . . . .	58
6.2	Plot of flight times vs. evolutionary ages of runaway stars – II. . . . .	59
6.3	Ejection velocity – Mass distribution. . . . .	62
6.4	Ejection velocity distribution. . . . .	64
6.5	Birthplaces of our sample of runaway stars. . . . .	64
6.6	Test of sensitivity to the Galactic potential. . . . .	66
7.1	Colour-magnitude diagram of the local Hipparcos sample. . . . .	73
7.2	Distribution of the relative error in parallax. . . . .	74
7.3	$(B - V)_0$ colours and Bolometric correction as a function of effective temperature. . . . .	76
7.4	Distribution of the Hipparcos sample absolute errors in the evolutionary age determination. . . . .	80
8.1	Birthplaces of Hipparcos sample stars. . . . .	84
8.2	Present position of Hipparcos sample stars' birthplaces. . . . .	85
8.3	Present position of Hipparcos sample stars' birthplaces (detail). . . . .	86
8.4	Present position of both the Hipparcos sample and runaways sample stars' birthplaces. . . . .	87

8.5	Simulated spiral arms. . . . .	92
8.6	Simulated stars in the solar neighbourhood according to arm of origin.	94
8.7	Plots comparing the observed and simulated distributions of the velocity's $x$ component of the local samples. . . . .	94
8.8	Plots comparing the observed and simulated distributions of the velocity's $y$ component of the local samples. . . . .	95
8.9	Plots comparing the observed and simulated distributions of the velocity's $z$ component of the local samples. . . . .	95



# List of Tables

4.1	Allen and Santillan (1991) model parameters . . . . .	28
4.2	Physical quantities that were used to constraint the parameters of the models, compared with the measured values. . . . .	33
4.3	Updated model parameters and total masses derived for each com- ponent. . . . .	34
4.4	Comparison of physical quantities computed from the model with measured values. . . . .	35
5.1	Initial sample, group A. . . . .	38
5.2	Initial sample, group B. . . . .	40
6.1	The flight times and evolutionary ages of SB 357, EC 20252–3137 and HIP 77131. . . . .	60
6.2	Runaway stars limiting magnitudes and completeness estimates. . .	67
7.1	Bolometric corrections. . . . .	76
8.1	Estimated pattern speed and phase. . . . .	86
A.1	Input data for stars belonging to group A. . . . .	104
A.2	Input data for stars belonging to group B. . . . .	106
A.3	Computed values for stars belonging to group A. . . . .	108
A.4	Computed values for stars belonging to group B. . . . .	110



# Chapter 1

## Runaway stars and the Milky Way

### 1.1 Introduction

The night sky has always been a source of wonder and awe, inspiration and sometimes even fear. Its study and careful observation has been for centuries the driving force behind philosophical speculation and scientific advance at the most fundamental levels. The precise cyclic yearly and daily motions of the – otherwise immobile<sup>1</sup> – stars was so impressive to the ancient Greeks that they named the entire Universe *κόσμος*, literally *order* in English. The night sky was viewed as perfect in opposition with the chaotic reality experienced on Earth. The position of stars and planets could be predicted, calendars could be created. It is not surprising, in this context that the sudden appearance of new celestial bodies was usually cast in bad light. In fact, the appearance of comets, for example, was usually seen as a harbinger of bad news or bad omens, as can be seen in Figure 1.1. Comets were strange bodies “polluting” the perfect heavens, they seemed out of place.

The Milky Way is one of the most striking features of the night sky. Yet, its nature and implication to humanity’s vision of the Cosmos remained hidden for most of Human history. In 1755, building on previous speculations by Thomas Wright, Immanuel Kant proposed that the Milky Way was an accumulation of stars in a disc-like shape with the Solar System placed inside this structure. Stars that were not in the disc were considered analogous to the comets in the Solar System, some kind of strange body outside the otherwise harmonious system. The concept of galaxy (*island universe* in Kant’s words) was thus born. It is interesting to note how the notions of a “perfect” system (the archetype being the Solar System) and the out-of-place, alien to the system, entities (the archetype being the comets) persisted, although they had lost most of their negative connotation by then.

---

<sup>1</sup>The lack of apparent proper motion led the ancients to refer to stars as *fixed* stars, in opposition to the planets which could be observed moving relative to the starry sky and were for this reason called *wandering* stars.

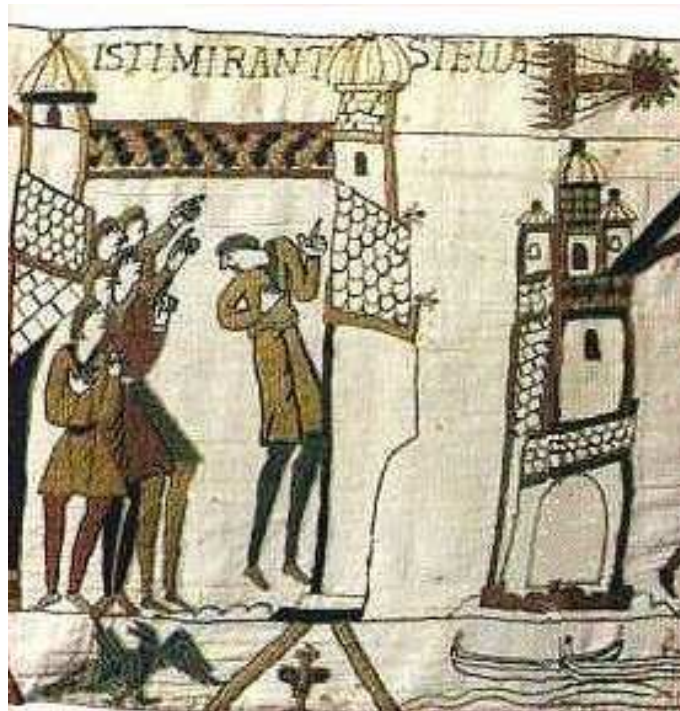


Figure 1.1: Comets were seen as anomalous stars, disrupting the otherwise harmonious heavens, usually considered harbingers of bad news. The appearance of the Halley comet in 1066 was recorded in the Bayeux tapestry, during the middle ages. *Isti Mirant Stella*, latin for “Those (men) marvelled at the star”. Source: <http://stardust.jpl.nasa.gov/news/news90.html>.

The understanding of galaxies continued to evolve until it received a major contribution by Baade in 1942. In that year he was able to resolve individual stars in the galaxy M31 (Andromeda; see Figure 1.2) and two of its companions for the first time. He observed that these stars were red giants, similar to the ones observed in globular clusters, in contrast to the blue giants that are the most luminous stars near the Sun. Baade concluded that stars in galaxies comprise two different populations: Population I stars typified by the stars in the Solar neighbourhood, and Population II stars typified by the stars in globular clusters. He further inferred that Population I stars are being formed in the present and Population II stars were formed in the past, because blue giants are usually associated with clouds of gas and dust, whereas red giants are not.

From the simple dichotomy stipulated by Baade, the concept of population grew into one of the most fundamental, if not the most fundamental, ideas used in the study of the origin and evolution of our Galaxy. Spectroscopic observations, combined with the then emerging theory of stellar evolution, and kinematical studies (based on ever-improving astrometric observations) eventually established the current general picture of stellar populations: Population I stars are young, metal-rich and have circular orbits in the plane of the Milky Way, whereas Population II stars are old, metal-poor and are on highly eccentric and/or inclined (in relation to the plane of the Milky Way) orbits. In other words, Population I stars correspond essentially to the stars in the disc of the Milky Way, whereas Population II stars

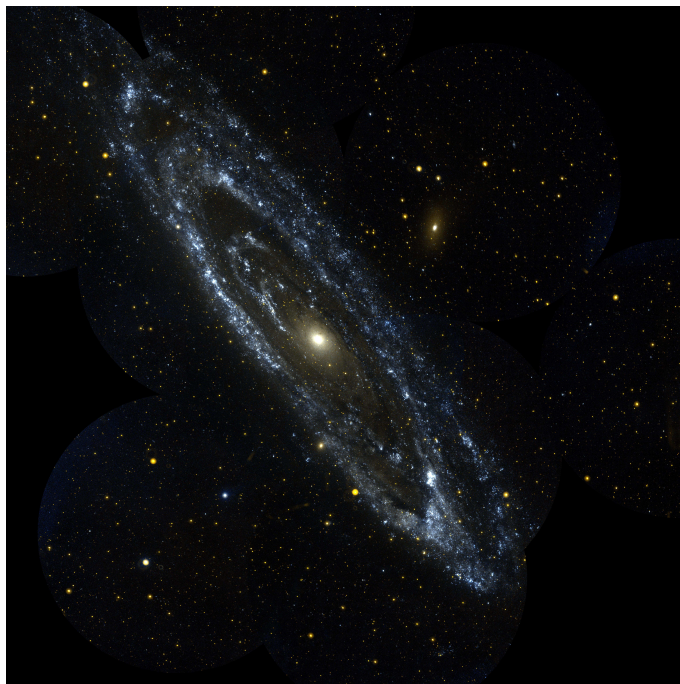


Figure 1.2: Image in ultraviolet light taken by the Galaxy Evolution Explorer (GALEX) telescope of the M31 galaxy (Andromeda). It is a mosaic composed by 10 different images taken in September 2003. The disc composed of young stars (Population I) is visible in blue and violet colours, whereas the bulge in the centre composed by older stars (Population II) is visible in red colour. Source: <http://photojournal.jpl.nasa.gov/catalog/PIA04921>.

comprise an *halo* of old stars surrounding the disc. In some ways this description is in agreement with the simple picture imagined by Kant. However, we will see that an analogy (in the sense that they appear out of place) to what he called “comets” of the Galaxy also exists.

A study of hot (blue) stars performed by Greenstein and Sargent (1974) presented a problem to the aforementioned picture of stellar populations. This study focused on 189 faint blue stars within 30 degrees of the Galactic poles, implying a location in the Galactic halo where Population II stars are expected to dominate. Although the presence of blue stars in the halo is not by itself problematic<sup>2</sup>, Greenstein and Sargent (1974) found the presence of stars indistinguishable from Population I stars, typical of the Galactic disc, not the halo. This difficulty was solved by identifying these displaced stars with the population of *runaway* stars.

The name *runaway star* was originally given only to stars that appeared to be leaving (with velocity vectors pointing away from) nearby stellar clusters. The concept was eventually generalised to include any young O-B type star (Population I) found far from their place of birth and/or that has higher than normal peculiar velocity. Even though runaway stars are interesting on their own merit (due to their somewhat exotic nature) we will show how they can be used to gain new

---

<sup>2</sup>Low mass stars emit blue light in later stages of their evolution: central stars of planetary nebulae and white dwarfs, for example.

insights into the nature of large-scale structure of the Galaxy.

According to the description of our Galaxy in terms of stellar populations, we have already mentioned that Population I stars are generally associated with the disc. More generally, star formation is thought to be confined to the Galactic disc. Moreover, in galaxies where star formation occurs, a spiral pattern (analogous to the one visible in Figure 1.2) is usually present. It is also usually observed that most blue light is emitted from these *spiral arms*, suggesting that most star formation is actually happening within them. Hence, it is natural to assume that our Galaxy also possesses some type of spiral arms.

Even though the existence of spiral arms in the Milky Way is usually assumed, it is impossible to observe the whole pattern directly as a result from our position within the Galactic plane. From our point of view, not only do the arms appear superimposed, but also most of the light emitted by them is absorbed by the great quantities of dust present in the disc's interstellar space. However, we have seen that some young stars "escape" from the disc: the high Galactic latitude runaway stars (e.g. Greenstein and Sargent, 1974). Since these runaway stars are found in the halo they are not as obscured by dust as stars in the disc. Hence they are visible at much larger distances. It is also important to note that it is estimated that there are approximately 5000 high Galactic latitude runaway stars in our Galaxy (in Silva and Napiwotzki, 2011, a density of  $\sim 8 \text{ kpc}^{-2}$  was derived).

We will propose that runaway stars can be used as tracers of the Milky Way's spiral arms. By using the technique of tracing their orbits back in time, we aim to show that it is possible to reconstruct the position of the spiral arms in different points in time. Our goal is to show the feasibility of this method not the delivery of a definite answer since better quality data would be needed to pursue the latter objective. This method has two advantages: high Galactic latitude runaway stars are not obscured by dust and move away from their place of birth allowing us to potentially probe spiral arms on the opposite side of the Galaxy; spiral arms can be reconstructed at different moments in the past, potentially allowing for an investigation of their own dynamics.

In summary, our objectives in this dissertation are:

- to improve the current understanding of the nature of high Galactic latitude runaway stars. In particular, we are interested in investigating the mechanisms responsible for their ejection from the Galactic disc (*ejection mechanisms*) through the analysis of their dynamics;
- to show the feasibility of using high Galactic latitude stars to trace the position of the spiral arms, and how they can be used to derive the spiral arms *pattern speed*.

The results pertaining to the first objective have already been published in Silva and Napiwotzki (2011).

## 1.2 Outline of the dissertation

In this dissertation, a sample of high Galactic latitude stars was selected in order to investigate whether their kinematical properties are consistent with the predictions by the theoretical ejection mechanisms. A second sample of local stars was selected to test the feasibility of using young early-type stars as tracers of the spiral arms. The spiral arms pattern speed was computed using this second sample, and the results compared with the ones obtained from the runaway sample. The main technique used was the tracing of stellar orbits back in time. The outline of this dissertation follows.

- In Chapter 2 we review the present knowledge of Galactic morphology and populations. Furthermore, the Milky Way's spiral arms are introduced as the focus of a very active area of research: we present its main assumptions, results and problems. In particular, we adopt the usual interpretation of the spiral arms as a density wave propagating with pattern speed  $\Omega_p$ .
- The place of high Galactic latitude runaway stars among the more general population of early-type main sequence stars is the theme of Chapter 3. We start the Chapter by reviewing the standard view of stellar evolution, and then describe the potential problem of confusion between high Galactic latitude runaway stars and late stages of evolution of low-mass stars and the methods used to solve it. Next, we present a condensed history of the high Galactic latitude runaway area of research, and its main problems, especially the relationship between the stars' kinematics and the ejection mechanisms, and the possible link between runaways and hypervelocity stars.
- Since the main analytical tool used is the tracing of stellar orbits back in time, Chapter 4 is dedicated to the review of the most important results of gravitational potential theory, and the description of the procedure we applied to obtain a gravitational potential model of the Galaxy. Special emphasis is given to the relationship between the gravitational potential and the rotation curve of the Galaxy. Also, the observational constraints to the gravitational potential are discussed.
- In Chapter 5 we describe the method used to select the sample of high Galactic latitude runaway stars used to investigate the properties of the general population, and the method used to derive the positions and velocities at the time of ejection of the runaways belonging to the selected sample, by tracing their orbits back in time. We also describe the methods used to obtain the present atmospheric and kinematical parameters.
- The results (ejection velocities, flight times and birthplaces) of the kinematical analysis carried out on the sample of runaway stars are presented in Chapter 6. These results were published in Silva and Napiwotzki (2011).

- The local sample of early-type stars used to test the feasibility of using stars as spiral arm tracers is presented in Chapter 7. We also describe the method used to estimate the spiral arms pattern speed.
- In Chapter 8, we present the estimated pattern speed, and corresponding spiral arms position. The comparison between the results obtained with the two samples are discussed. We also discuss other results from the literature. Finally, a simulation produced in order to test our assumptions is also discussed.
- We finish by presenting our main conclusions in Chapter 9.

# Chapter 2

## The Milky Way

### 2.1 Morphology

The morphology of our Galaxy, the Milky Way, is still a matter of debate, but some aspects of it are thought to be well understood. The description of the Galaxy's structure and evolution presented here are based on Robin et al. (2003), the review by Majewski (1993), and references therein, unless otherwise noted. At the most basic level the Galaxy is an interacting collection of stars, gas, dust and dark matter. If we restrict our attention to the stellar component we can observe a well defined structure. This structure is divided into four components, which can be distinguished by their morphology, age, metal content, and kinematics. The oldest and biggest component is the spherical halo that surrounds the entire Galaxy, having a diameter of about 100 kpc and being very metal-poor. It is also the region where we find most globular clusters of our Galaxy. In the centre, we have another old spherical component, the central bulge, containing stars with a large range of metallicities. It is now believed that the bulge is actually dominated by a bar-like structure (cf. Binney et al., 1997 and references therein). Around the central bulge we have then the thin and thick discs. The thin disc is the youngest component, followed by the thick disc. The thin disc is also the most metal-rich component, whereas the thick disc is less metal-rich but still has higher metallicity than the halo. Nevertheless, the exact separation between these two disc components remains a matter of contention, as it is difficult to define where one ends and the other starts. For example, Jurić et al. (2008) find a local density of the thick disc equal to 12 per cent of the local density of the thin disc, whereas for Robin et al. (2007) the former is only 1.15 per cent of the latter. The thick disc scale heights corresponding to these estimates are respectively 3.6 kpc and 1.2 kpc, suggesting a degeneracy between the local density and the scale height of the thick disc.

The stars which compose the Galaxy are usually divided into two different populations: Population I stars are young, metal-rich and are the stars found in OB associations, open clusters and HII regions, while Population II stars are old, metal-poor and are typically found in globular clusters. These differences are

interpreted in an evolutionary framework, where the halo stars were formed first, in the initial collapse of the proto-Galaxy, the thick disc stars were formed next, followed by the thin disc stars. However, note that it is argued that the halo was formed by a series of accretion events (Klement, 2010). Nowadays, star formation appears to be confined to the star forming regions in the spiral arms of the thin disc. The difference in metallicities is due to the enrichment of the interstellar medium (ISM) caused by successive supernova events. In this framework, Population I stars are to be identified with the thin and thick disc populations, and the Population II stars to the halo and bulge populations.

This picture is confirmed by the different kinematics: stars in the thin disc (usually identified as Population I) essentially rotate around the centre of the Galaxy, with very little velocity dispersion, whereas stars in the halo usually have a high perpendicular velocity component and high velocity dispersion. This is because young stars born in the disc have essentially the same dynamics as the rotating gas clouds while the stars in the halo still reflect the dynamics of the initial collapse.

## 2.2 The spiral arms

Spiral arms are readily visible in face-on external spiral galaxies as exemplified by the galaxy M51 (see Figure 2.1). As in the case of this galaxy, they are usually traced, in visible light, by the luminous young O-B stars, and the HII regions ionized by these hot stars ( $H\alpha$  emission). In other words, star formation occurs mostly in the spiral arms. It is assumed that this is true also in our own Galaxy. Hence, many attempts have been made to obtain a similar map of the spiral arms in our Galaxy. However, because of our position within the Galactic plane, the spiral arms are heavily obscured by dust and appear superimposed along our line of sight making it difficult to distinguish them. Consequently the precise shape and number of arms remains a matter of contention.

Russeil (2003) fitted arms with logarithmic spiral<sup>1</sup> shape to the distribution of a catalogue of HII star-forming complexes. Distances to the complexes were computed either from observations (spectroscopic and photometric) of the hot exciting stars, whenever possible. In cases where the radial velocity was the only information available, distances were computed using the kinematical distance method. The best fit obtained is a pattern of four spiral arms with initial radius  $r_0$  varying between 3.5 kpc and 4.5 kpc, and a pitch angle varying between  $9.1^\circ$  and  $12.1^\circ$  for the different arms.

Vallée (2008) proposed a cartographic model consisting on four arms with a logarithmic spiral shape, having a pitch angle  $p = 12.8^\circ$  and  $r_0 = 2.1$  kpc. The

---

<sup>1</sup>A logarithmic spiral is defined, in the usual cylindrical coordinates  $(r, \theta)$ , by:  $r(\theta) = r_0 \exp(b\theta)$ , where  $r_0$  is the initial radius and  $b = \tan p$ . The pitch angle,  $p$ , is the complement of the angle between the tangent to the spiral and the tangent to a circle with radius  $r(\theta)$ . A logarithmic spiral is thus defined by the two parameters:  $r_0$  and  $p$ .



Figure 2.1: Image of the galaxy M51, together with its companion NGC 5195. The spiral arms are populated by luminous, young, blue stars and the associated reddish HII regions of ionized gas. This is a false colour Hubble Space Telescope where the  $H\alpha$  emission line is emphasized. Source: <http://apod.nasa.gov/apod/ap050428.html>.

parameters were estimated by combining the results from many different studies of the spiral arm structure of our Galaxy. The tracers used on these different studies range from molecular gas ( $H_2$  and CO) and dust to the optical observation of open clusters and HII regions. For this reason, these can be considered the best estimates of the present position of the spiral arms.

More recently, Lépine et al. (2011) observed the spiral arms as traced by emission from the CS molecule. Newly born stars radiate the surrounding gas (HII regions) and dust. The molecules that are associated with the dust in star-forming regions consequently emit infrared radiation. The results obtained in this paper are generally consistent with the ones obtained by Russeil (2003): three arm segments are visible on each side of the Galactic Centre (compare Figure 4 of the former with Figure 5 of the latter). However, a departure from the simple logarithmic spiral model was found, as some arm segments are almost straight lines.

The spiral arms are interpreted in a theoretical framework first proposed by Lin and Shu (1964). In this framework, the arms are not a material structure, but a stationary *density wave* rotating as rigid body with angular speed  $\Omega_p$ . As the wave propagates in the Galactic disc it creates overdense regions triggering a burst of star formation, originating the observed accumulation of young stars along the arms. This theory has the advantage of avoiding the so-called “winding” problem<sup>2</sup>. These waves have probably a kinematical nature (see Toomre, 1977 for a good review). Stellar orbits of the type shown in Figure 2.2 of successive increasing radii can be organized in such way as to produce a *locus* resembling a spiral pattern, as can be seen in Figure 2.3. Such spiral wave patterns rotate rigidly with the pattern speed  $\Omega_p$  in the condition that the orbits have the same

<sup>2</sup>The “winding” problem affects material spiral arms in a disc in differential rotation. The arm winds up because points closer to the centre rotate faster than points further away.

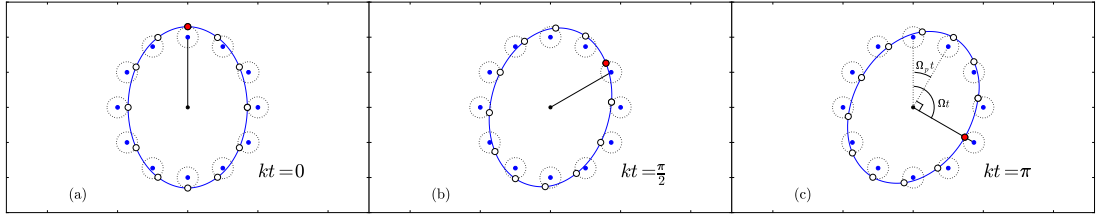


Figure 2.2: Shown in panel (a) are 12 test particles travelling clockwise with mean angular speed  $\Omega$  around the Galactic Centre in similar and nearly circular orbits (after Toomre, 1977). These orbits are doubly periodic: there is a periodic radial excursion, here represented by the dotted *epicycles* along which the particles move counterclockwise with period  $2\pi/k$  around their mean orbital positions (or *guiding circles*); the rotation of the guiding circles around the Galactic Centre with period  $2\pi/\Omega$  constitutes the other periodic motion. Between panels (a) and (b) the particles have travelled  $\pi/2$  along the epicycles as can be seen in the particle highlighted in red. The *locus* of the test particles positions is an ellipse which precesses with speed  $\Omega_p$ . In other words, in a frame of reference rotating with speed  $\Omega_p$  these orbits will appear to be closed. The value of  $\Omega_p t$  can be easily seen to be  $\Omega t - \pi/2$  by comparing panels (a) and (c).

precession speed (equal to the pattern speed) at all radii. This condition is fulfilled for orbits of the type represented in Figure 2.2, with  $\Omega_p = \Omega(R) - k(R)/2$  (Kalnajs, 1973).

The determination of the spiral pattern speed  $\Omega_p$  has been the subject of many different studies. The different methods used to estimate the value of  $\Omega_p$  are reviewed by Gerhard (2010). The most direct method consists in finding the birthplaces of open clusters or individual young stars by computing their orbits and following them backwards in time. The position of the birthplaces coincides with the position of the spiral arms, assuming that star formation occurs mostly in the spiral arms, hence the pattern speed can be estimated comparing the present position of the arms with their position at the time of birth of the clusters or stars. This method was applied to a sample of local young stars by Yuan (1969) who obtained  $\Omega_p = 13.5 \text{ km s}^{-1} \text{ kpc}^{-1}$ , assuming a model with two arms. More recently, Amaral and Lépine (1997) and Dias and Lépine (2005) applied the same method, now assuming models with 4 arms, to samples of open cluster finding  $\Omega_p \simeq 20 \text{ km s}^{-1} \text{ kpc}^{-1}$  and  $\Omega_p \simeq 24 \text{ km s}^{-1} \text{ kpc}^{-1}$ , respectively. Another method consists in fitting a kinematic model (including the kinematic response to a spiral arm perturbation) to the observed kinematics of OB stars and Cepheids. This method was applied by Fernández et al. (2001), who obtained a value of  $\Omega_p \simeq 30 \text{ km s}^{-1} \text{ kpc}^{-1}$ .

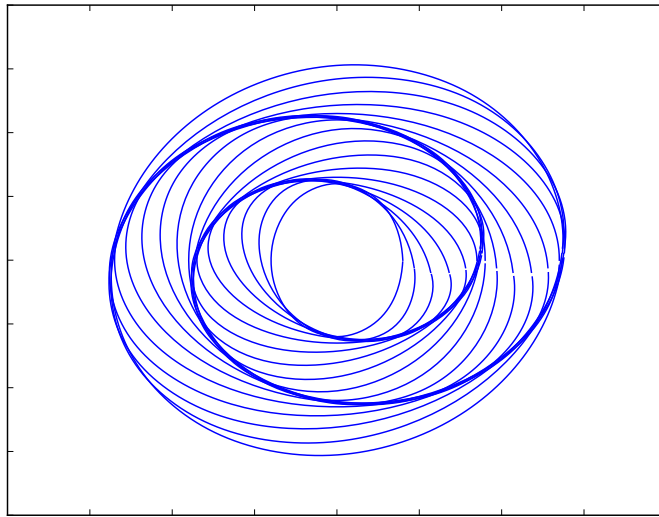


Figure 2.3: A spiral pattern is produced by rotating the major axis of uniformly filled orbits like the one seen in Figure 2.2, at different radii (after Kalnajs, 1973). This pattern is wavelike in nature, travelling with speed  $\Omega_p$ , assuming all orbits have the same precession rate.



# Chapter 3

## Early-type stars and runaway stars

### 3.1 Overview

Before describing the population of runaway stars in more detail, it is useful to summarise the stellar evolution of stars of different masses. This is also a good way to introduce some aspects responsible for problems related to the identification of runaway stars at high Galactic latitudes. The definition of runaway stars is then given, and an historical perspective of the evolution of the concept leads us to an introduction to the problems and methods in the field.

### 3.2 Stellar evolution

Stellar evolution depends essentially on the initial mass of the star. As such, stars are usually grouped in three different groups, according to their initial mass: low-mass, intermediate-mass and massive. The difference between low-mass and intermediate mass is related to whether the star develops a degenerate core after it finishes burning hydrogen in its core, whereas the difference between massive and intermediate-mass stars is related to whether they end their lives as a black hole or neutron star (massive stars), or a white dwarf (intermediate-mass stars). The limiting masses between the different groups are somewhat uncertain, however the following masses are indicative (after Iben, 1991):  $2 M_{\odot}$  and  $6 - 8 M_{\odot}$  are respectively the lower and upper limits to the mass of intermediate mass stars.

The following summaries of stellar evolution follow the discussion by Iben (1991) and, in the case on low-mass stars, the study by Dorman et al. (1993).

**Intermediate-mass star** Approximately 80 per cent of the nuclear lifetime is spent on the *main sequence* (MS) converting hydrogen into helium inside a convective core. When the hydrogen in the core is almost exhausted, the burning of hydrogen in a thin shell above the helium core starts. This increases the size of the helium core until it reaches the Schönberg-Chandrasekhar limit and starts to

collapse. From this moment the evolution proceeds on the faster Kelvin-Helmholtz time scale to the *red giant branch (RGB)*. During this phase, the envelope expands because of the rapid increase in the rate of energy generation by the hydrogen-burning shell, causing a decrease in the effective temperature. The ensuing increase in opacity causes a convection zone to develop near the surface. This convection zone grows inward until it eventually reaches zones rich in elements produced by the CNO cycle (in particular nitrogen), bringing them to the surface. This process results in a measurable modification in the abundances of carbon and nitrogen in the surface and is known as the *first dredge-up*. The envelope eventually cools enough that the opacity decreases again. This is the moment the star finally enters the RGB, evolving nearly vertically in the H-R diagram. When the core reaches a temperature of  $\sim 10^8$  K and a density of  $\sim 10^4$  g cm $^{-3}$  the triple alpha process is initiated, marking the onset of core helium burning. The core expands again and the envelope contracts resulting in an increase of the effective temperature. This phase lasts for about 10 per cent of the total MS lifetime and is known as the *red clump*. As in the case of hydrogen burning, when the helium in the core is almost depleted, the burning of helium starts in a shell above the helium core. The helium core heats as it contracts while the hydrogen envelope (which is still the main source of energy at this point) expands and cools. The result is that the hydrogen ceases to burn in this exterior shell. The star then evolves again in the direction of the RGB. As the effective temperature decreases, a convective zone develops in the envelope, growing inward. This convective zone eventually reaches zones rich in helium and CNO reaction products, bringing helium and nitrogen to the surface in what is called the *second dredge-up*. From this point, the luminosity increases again and the star ascends what is known as the *asymptotic giant branch (AGB)*. Furthermore, the carbon/oxygen core becomes so dense that the electrons become degenerate, which in effect means that the core is indistinguishable from a hot white dwarf. As the star ascends the AGB, hydrogen and helium are burned alternately in shells, hundreds of neutron-rich isotopes are created (s-process), and convective layers appear (as before) bringing these elements to the envelope in a series of *third dredge-up* processes. This final phase is usually called thermally pulsing AGB and culminates with the ejection of the envelope. The result is a hot central star (the core of the star before the envelope ejection) surrounded by an ionized shell of gas (the ejected envelope), a *planetary nebula*. The hot central star then contracts at constant luminosity, travelling horizontally along the H-R diagram, until it becomes a white dwarf. This phase is known as the post-AGB (PAGB).

**Massive star** In the case of a massive star, after the exhaustion of hydrogen in the core, the switch to helium burning happens before the star reaches the RGB. The effective temperature continues to drop as the helium-burning core contracts (while most of the luminosity is provided by an hydrogen-burning shell) and the envelope expands. When the helium in the core is almost exhausted the central temperature and density are so high that carbon burning starts almost

immediately. What follows is a succession of nuclear reaction sequences producing elements close to the iron peak of the *binding energy* curve. The core temperature eventually becomes so high that the process of *photodisintegration* starts, breaking the nuclei of elements present in the core into essentially protons and neutrons. As the photodisintegration reaction removes photons from the core, the contribution to the total pressure holding the outer core given by the radiation pressure plummets. Moreover, the free electrons, which until this moment were helping in supporting the core through electron degeneracy pressure, are captured by this fresh population of protons. The collapse of the core is then inevitable and it happens so quickly that the inner core decouples from the outer core. The density inside the inner core eventually becomes large enough (corresponding to a mass larger than the Chandrasekhar limit) that the neutrons become degenerate stopping the collapse. This sudden event results in a shock wave travelling outward in the direction of the infalling outer core and envelope. When this shock wave encounters the infalling material the latter is ejected in a violent explosion known as a *Type II supernova*. The inner core becomes either a neutron star or a black hole depending on the mass of the star: if the initial mass is too large, the neutron degeneracy is not enough to stop the collapse and a black hole is formed, otherwise the remnant will be a neutron star.

**Low-mass star** The evolution of a low-mass star during the RGB phase differs from that of an intermediate-mass one. In the case of the latter, the hydrogen-depleted core quickly collapses and heats enough to start helium burning at the tip of the RGB. On the other hand, in the case of a low mass star, the core does not heat quickly enough and eventually it becomes electron-degenerate effectively stopping the collapse. However, the hydrogen-burning shell continues to produce helium which is deposited in the core. Thus, the mass of the core increases, causing a gradual increase in temperature, until it reaches a critical limit ( $\sim 0.5 M_{\odot}$ ) when the helium is finally ignited in a sudden episode called the *helium core flash*. The star then enters the core helium burning phase: if the star is metal-rich it will occupy the red clump, as the intermediate-mass stars, whereas if it is metal-poor it will move to the *horizontal branch* sequence, covering a much wider range in effective temperatures. Since the mass of the core does not depend on the initial mass of the star, for the reason presented before, the evolutionary path after the core helium burning phase will essentially be a function of the envelope mass. If the envelope mass is greater than a critical value  $M_{\text{env}} \sim 0.05 M_{\odot}$ , there will be enough hydrogen fuel for the star to ascend the AGB until the thermally pulsing AGB phase and consequent formation of a planetary nebula before entering the PAGB phase, just like an intermediate-mass star. On the other hand, if the envelope mass is lower than the critical value than the star is said to be part of the extreme horizontal branch (EHB) and there are two possible scenarios (see Figure 3.1): the star may evolve in the direction of the AGB but because the hydrogen-burning shell is quickly consumed it never enters the thermally pulsing AGB and goes directly to the PAGB phase; or, if the envelope mass is sufficiently small, the effective temperature never decreases enough for the star to approach the AGB,

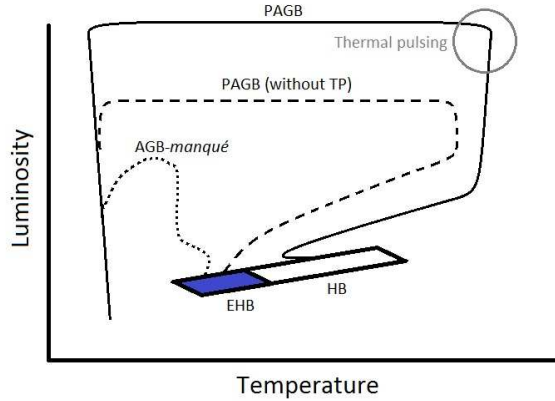


Figure 3.1: The different evolutionary paths of a low-mass star after the HB stage (after Dorman et al., 1993). Depending on the mass of the envelope there are three possibilities: if the envelope mass is greater than a critical mass  $M_{env} \sim 0.05 M_{\odot}$ , it will ascend the AGB and go through the thermally pulsing AGB phase, before entering the PAGB (solid line); if the envelope mass is lower than the critical mass but enough to develop a convective envelope it will ascend part of the AGB, but without entering the thermally pulsing AGB phase (dashed line); finally, if the mass is not enough to develop a convective envelope, the star will not ascend the AGB but it will remain hot throughout its post-HB evolutionary phase, before entering directly the white dwarf cooling sequence (dotted line).

in which case it will evolve as an hot star until it enters the white dwarf cooling sequence directly (such evolutionary path is known as *AGB-manqué*). It is also relevant to note that the effective temperature of stars as they enter the HB is inversely proportional to the envelope mass.

### 3.3 Observational properties

The classification of the evolutionary status of a star (i.e. whether it is on the MS, RGB, HB, AGB or PAGB phases) is immediate if its total luminosity, effective temperature and metallicity are known, as it is then possible to place them in the H-R diagram. However, what is usually obtained from observations are the effective temperature and the surface gravity (the abundances of elements present in the photosphere may also be obtained). Nevertheless the luminosity may be easily calculated from:

$$L = 4\pi R^2 \sigma T_{\text{eff}}^4, \quad (3.1)$$

if the mass is known, because  $g = GM/R^2$ . Thus it is usual to use the measured surface gravity as a proxy for luminosity. The problem is that the mass is usually not known, consequently it is possible to confuse low-mass dense stars with high-mass with lower density. This problem was pointed out by several studies on the nature of early-type stars found in the halo (e.g. Tobin, 1987; Hambly et al., 1997; Ramspeck et al., 2001a). In fact, the evolutionary tracks of hot low-mass stars on the HB and stars on the PAGB cross the evolutionary tracks of main sequence OB stars, on a  $T_{\text{eff}} - \log g$  diagram.

Thus, in order to discriminate the evolutionary status of a star other observable quantities are needed. We have seen in the last section that the abundances of elements in the photosphere change as the star evolves due to the several dredge-up events. Additionally, abundances in the photospheres of hot HB stars have many peculiarities (relative to MS stars), including underabundance of helium and overabundance of heavy elements, because of processes like gravitational settling or radiative levitation, collectively known as diffusion processes (see Behr, 2005, Moehler et al., 2000 and references therein). Hence, a careful study of the abundances in the photosphere of a star is in principle enough to discriminate its evolutionary status. Another useful indicator is the projected rotation velocity as it is observed that evolved stars rotate slower than stars still on the MS (see Magee et al., 1998; Behr, 2003a and references therein). This is quite fortunate, because a high projected rotation velocity hinders the measurement of abundances.

These two indicators were used in most studies of runaway stars at high Galactic latitudes, e.g. Martin (2004), Lynn et al. (2004a), Lynn et al. (2004b), Magee et al. (2001), Ramspeck et al. (2001b), Rolleston et al. (1999), Rolleston et al. (1997), Saffer et al. (1997).

## 3.4 High Galactic latitude runaway stars

### 3.4.1 Definition and history

Runaway stars are normal blue young stars which have very high peculiar velocities and are found far from their places of birth. A number of runaways are known to exist in the halo presenting some difficulties for the accepted picture of star formation in our Galaxy. Two scenarios have been proposed to explain the ejection of these stars from their places of birth in the spiral arms to their present positions in the halo: the Binary Ejection Mechanism (BEM) and the Dynamical Ejection Mechanism (DEM). The two scenarios make different predictions about the ejection velocity distribution.

As mentioned in the previous section, star formation is thought to occur mostly in the spiral arms of the Galactic disc, in particular in open clusters and OB associations, and most young stars have circular orbits around the Galactic Centre, having essentially no velocity dispersion. The fact that they have so small velocities relative to their standards of rest (a frame of reference which co-rotates with the disc, centred in the star's position), means they would, in principle, not be able to move very far away from the place where they are born, in their short lifetimes (around  $10^8$  years for a B star). Given that the velocity dispersion of OB stars is around  $13 \text{ km s}^{-1}$  (Gies and Bolton, 1986), a star should only migrate about 1 kpc away from its place of birth.

In fact, several studies (Karimova and Pavlovskaya, 1984; Stone, 1979, 1991), have shown that the residuals of the OB stars space velocities are best fitted with the sum of two Maxwellian distributions, one corresponding to “small” velocity

component (with a velocity dispersion of about  $10 \text{ km s}^{-1}$ ), and one to a “high” velocity component (with a velocity dispersion of about  $30 \text{ km s}^{-1}$ ). It should be mentioned that these studies focus on stars which are still in or close to the disc of the Galaxy (most have a Galactic latitude close to  $0^\circ$ ), although they are far from the associations where they were born.

A study undertaken by Greenstein and Sargent (1974) analysed a sample of 189 faint blue (FB) stars in the Halo (most stars within  $30^\circ$  of the Galactic poles). This study claimed that 26 per cent of the sample consisted of B stars spectroscopically indistinguishable from normal main sequence stars. Also, it was found that these “normal” stars had abnormally high space velocities (a velocity dispersion of  $80 \text{ km s}^{-1}$ ) and were at a mean distance to the disc of 4 kpc. Since then, many more studies (Conlon et al., 1988, 1990; Ramspeck et al., 2001b and references therein) have confirmed their identification as normal young stars. If these stars were really formed in the disc and then ejected by some mechanism to their present positions in the halo, then they must have left the disc with velocities exceeding  $100 \text{ km s}^{-1}$ , or even several times that, in the more extreme cases. These halo stars correspond to runaway stars which have velocities in high end tail of the velocity distribution.

### 3.4.2 Ejection mechanisms

Two ejection mechanisms have been proposed:

1. **the binary ejection mechanism (BEM)**: this was first proposed by Blaauw (1961) to explain the ejection of runaway O and B stars out of the Galactic plane. In this scenario the secondary star of a close binary receives its ejection velocity when the primary explodes as a supernova. Because one of the stars explodes, this model predicts that runaway stars should never be found in binaries (composed of two main sequence stars). Calculations by Portegies Zwart (2000) predict a negative mass-ejection velocity correlation (secondary stars with lower masses receive the greatest kicks) and a maximum ejection velocity of  $\lesssim 300 \text{ km s}^{-1}$ . Similar results were found by Leonard and Dewey (1993). More recently, Przybilla et al. (2008) estimated that velocities up to  $\simeq 400 \text{ km s}^{-1}$  are possible in binaries containing an early B and a Wolf-Rayet star.
2. **the dynamical ejection mechanism (DEM)**: this was first proposed by Poveda et al. (1967) as an alternative to produce runaway stars. Dynamical interactions between stars inside young, open clusters can give large kicks to one or both stars involved in a collision, i.e. a close encounter. The large ejection velocities are achieved most efficiently by collisions of two close binaries (since they have larger cross-sections for the collision). Calculations by Leonard and Duncan (1990) predict a binary fraction among runaway stars of about 10 per cent, a negative mass-ejection velocity correlation, and a maximum ejection velocity of  $\lesssim 200 \text{ km s}^{-1}$ . Later simulations by Leonard

(1991), conducting a larger number of experiments, revised the value of the maximum ejection velocity to  $\lesssim 400 \text{ km s}^{-1}$ , although very rare events producing velocities up to  $\lesssim 1000 \text{ km s}^{-1}$  are possible (by setting the parameters *a posteriori* to maximize the velocity). More recently, Gvaramadze et al. (2009) have shown that collisions between binaries and very massive stars ( $M \gtrsim 50 M_{\odot}$ ) can also eject stars with velocities up to  $300 - 400 \text{ km s}^{-1}$ .

Both mechanisms were found to operate in nature in a study by Hoogerwerf et al. (2001) by tracing back in time the orbits of runaway stars to their parent clusters. Two main sequence runaway stars were traced back to the same region of the Orion association Ori OB1, which is evidence for the DEM. In contrast, a runaway star and a pulsar were traced back to the same region of the Sco OB2 association, which is evidence for the BEM. This study used proper motion (high precision astrometry was made available by Hipparcos) and radial velocity data to trace back in time the orbits of runaway stars to the parent cluster. This method makes it possible to estimate the moment in time when the star left the cluster and also the velocity at that instant (the ejection velocity). Since the orbits are computed in a realistic Galactic potential, actual estimates of these quantities were obtained instead of lower limits as was done in previous studies which used only radial velocity information and/or ignored the Galactic potential. In this work we use a similar method but we apply it to distant stars.

The predicted ejection velocity distribution is similar in both models but there are some differences, in particular the DEM predicts an enhanced high velocity tail. Studies in the past have not been able to properly constrain the ejection velocity distribution for two reasons: small, biased samples, and lack of proper motion measurements for the more distant stars. Since the more distant stars correspond to the higher velocities, this second aspect is of particular relevance. This is made clear if we remember that the more systematic studies to date were based on Hipparcos data (Martin, 2006; Allen and Kinman, 2004), with a limiting magnitude of  $V \simeq 12.4$  and complete only up to  $V \simeq 9$ . On the other hand, studies based on the Palomar-Green (Green et al., 1986) and Edinburgh-Cape (Stobie et al., 1997) surveys reach fainter magnitudes but many stars in these studies have unreliable ejection velocity estimates due to the lack of proper motion measurements.

### 3.4.3 Hypervelocity stars

Hypervelocity stars are a different class of stars moving with even higher velocities than runaway stars, in unbound orbits. They are generally believed to have been ejected by the Supermassive Black Hole in the centre of the Milky Way (Brown et al., 2007b), the so-called Hills mechanism (Hills, 1988).

Evidence in recent studies for a link between runaway stars and hypervelocity stars has been mounting up. A systematic search for hypervelocity stars undertaken by Brown et al. (2007a) resulted in the finding of seven stars still bound to the Galaxy. Although these stars were still interpreted as hypervelocity stars

(based on their high spatial velocities and large distances) and consequently assumed to have been ejected from the centre of the Galaxy, it is possible that at least some of them were ejected far from the Galactic Centre as well, since no dynamical analysis was performed to verify their places of origin. The hypervelocity stars HD 271791 and HIP 60350 were determined to have been ejected from regions far from the Galactic Centre and with velocities compatible with present models (Heber et al., 2008; Przybilla et al., 2008) and for HIP 60350 (Irrgang et al., 2010).

# Chapter 4

## Dynamics in a gravitational potential

### 4.1 Gravitational potential for spherical and cylindrical geometry

The main technique used in this dissertation in the kinematical study of certain stellar populations is the reconstruction of their orbits in the past. In this chapter we will introduce the tools and concepts needed to perform the kinematical analysis of a massive body under the influence of the gravitational force. In our presentation of this topic we follow the standard reference in the field of galactic dynamics, the book by Binney and Tremaine (2008).

The motion of every star in any galaxy, and in ours in particular, is determined by the combined action of Newton's gravitational forces exerted on it by all the massive objects (stars, dark matter and gas clouds) in the galaxy. Thus, in order to compute the net acceleration on any given star we would need, in principle, to compute the individual contributions from all the gravitational point sources and add them all together. However, given the large number of point sources in a galaxy ( $\sim 10^{11}$ ), this approach is not practicable. Instead, this discrete distribution of mass is usually approximated by a smooth continuous mass (density) distribution,  $\rho(\mathbf{x})$ . An orbit is defined as the path described by a star as it moves through the galaxy. The aim of this section is to show how to compute the orbit of a star in the presence of the gravitational potential  $\Phi(\mathbf{x})$  created by a mass distribution  $\rho(\mathbf{x})$ .

Before introducing the formalism of potential theory used in the remainder of the chapter, we will justify the approximation of the discrete mass distribution found in reality by a smooth mass distribution  $\rho(\mathbf{x})$ .

The net force  $\mathbf{F}(\mathbf{x})$  on a particle of mass  $m$  that is created by the density distribution  $\rho(\mathbf{x}')$  is given by the sum of all the small contributions from the volume elements  $d^3\mathbf{x}'$ :

$$\mathbf{F}(\mathbf{x}) = mG \int \rho(\mathbf{x}') \frac{\mathbf{x}' - \mathbf{x}}{|\mathbf{x}' - \mathbf{x}|^3} d^3\mathbf{x}', \quad (4.1)$$

where  $G$  is the constant of gravitation. It is useful to define the *gravitational field*  $\mathbf{g}(\mathbf{x})$  given by:

$$\mathbf{F}(\mathbf{x}) = m\mathbf{g}(\mathbf{x}). \quad (4.2)$$

Moreover, since the gravitational force is conservative we know that we can write the gravitational field as the gradient of a scalar field. Thus

$$\mathbf{g}(\mathbf{x}) = -\nabla\Phi. \quad (4.3)$$

The scalar field  $\Phi(\mathbf{x})$  is the *gravitational potential*. It is usually more convenient to compute the gravitational potential instead of either the force or the field, as it is a scalar field. In fact, it can be shown that the potential  $\Phi(\mathbf{x})$  is related to the mass density  $\rho(\mathbf{x})$  by the *Poisson equation*:

$$\nabla^2\Phi(\mathbf{x}) = 4\pi G\rho(\mathbf{x}). \quad (4.4)$$

This equation can be solved for a given mass density distribution  $\rho(\mathbf{x})$  and appropriate boundary condition<sup>1</sup>.

### 4.1.1 Circular speed and perpendicular force

Before proceeding, it is useful to define some physical quantities that are often encountered when analysing the properties of potential-density pairs according to Equation (4.4).

In the special case of a test particle in a circular orbit of radius  $r$  it is possible to derive a simple expression for its speed  $v_c(r)$ , the *circular speed*. Since the particle's centripetal acceleration  $v_c^2/r$  as to be balanced by the absolute value of the gravitational acceleration (as given by Equation 4.2) we have:

$$v_c^2 = r|\mathbf{g}|. \quad (4.5)$$

This equation can be solved exactly in some important particular cases. When the potential has a spherical symmetry,  $\Phi$  is a function of radius only. Thus, from Equation (4.3) follows:

$$v_c^2 = r \frac{d\Phi(r)}{dr}. \quad (4.6)$$

Another important case is that of an axisymmetric potential, a simple approximation to the disc of spiral galaxies like our own. In this case,  $\Phi(r, \phi, z)$  does not depend on the azimuthal coordinate  $\phi$ , and the perpendicular force (per unit mass)  $K_z = d\Phi/dz$  is zero in the equatorial plane ( $z = 0$ )<sup>2</sup>, hence the circular speed is given by Equation (4.6) once again.

<sup>1</sup>The usual boundary condition for a closed system is  $\lim_{x \rightarrow +\infty} \Phi(\mathbf{x}) = 0$ .

<sup>2</sup>This is true when the mass distribution is symmetrical around the equatorial plane,  $z = 0$ , as is usually assumed in most galactic models.

The circular speed  $v_c$  is an important tool in studying the potential of spiral galaxies, and ours in particular, as most stars in the equatorial plane of the disc have circular, or almost circular orbits. The measured  $v_c(r)$  for a given galaxy is called its *rotation curve* and is one of the main constraints on the potential of galaxies, in particular their discs, and also their mass through Poisson's Equation (4.4).

Another important quantity, in the case of axisymmetric potentials models for galactic discs, is the aforementioned perpendicular force  $K_z = d\Phi/dz$ . Its relevance becomes clear if we write Poisson's Equation (4.4) for a system consisting of an axisymmetric disc. In this case, using cylindrical coordinates, we have (as detailed in e.g. Binney and Tremaine, 2008; Kuijken and Gilmore, 1989):

$$\frac{1}{r} \frac{\partial}{\partial r} \left( r \frac{\partial \Phi}{\partial r} \right) + \frac{\partial^2 \Phi}{\partial z^2} = 4\pi G \rho(r, z). \quad (4.7)$$

Given Equation (4.6), this can be written in terms of the circular speed and the perpendicular force  $K_z$ . Thus,

$$2 \frac{v_c}{r} \frac{\partial v_c}{\partial r} + \frac{\partial K_z}{\partial z} = 4\pi G \rho(r, z). \quad (4.8)$$

It is now useful to introduce the two functions <sup>3</sup>:

$$\begin{aligned} A(r) &= \frac{1}{2} \left( \frac{v_c}{r} - \frac{dv_c}{dr} \right), \\ B(r) &= -\frac{1}{2} \left( \frac{v_c}{r} + \frac{dv_c}{dr} \right). \end{aligned} \quad (4.9)$$

Now, since

$$A^2(r) = \frac{1}{4} \left( \frac{v_c^2}{r^2} - 2 \frac{v_c}{r} \frac{dv_c}{dr} + \left( \frac{dv_c}{dr} \right)^2 \right)$$

and

$$B^2(r) = -\frac{1}{4} \left( \frac{v_c^2}{r^2} + 2 \frac{v_c}{r} \frac{dv_c}{dr} + \left( \frac{dv_c}{dr} \right)^2 \right),$$

we have:

$$A^2(r) - B^2(r) = -\frac{v_c}{r} \frac{dv_c}{dr}.$$

---

<sup>3</sup>The relevance of this functions is easily understood if we compute their value when  $r$  is the radius of the Sun's orbit,  $r_0$ . In that case  $\Omega_0 = v_c^0/r_0 = A(r_0) - B(r_0)$ , and  $dv_c/dr|_{r_0} = -(A(r_0) + B(r_0))$ , so we find that  $A$  and  $B$  correspond to the so-called *Oort constants*, at the Sun's radius. Note also that a flat rotation curve implies that  $A \simeq -B$ , and vice-versa.

Hence, Equation (4.8) can be rewritten as:

$$\rho(r, z) = \frac{1}{4\pi G} \frac{\partial K_z}{\partial z} - \frac{1}{2\pi G} (A^2(r) - B^2(r)). \quad (4.10)$$

The integral of Equation (4.10) from  $z = -1.1$  to  $z = 1.1$  yields an expression for the (integrated) surface mass density within 1.1 kpc of the Galactic disc<sup>4</sup>:

$$\Sigma_z(r) = \frac{K_z}{2\pi G} - z \frac{A^2(r) - B^2(r)}{\pi G}, \quad (4.11)$$

assuming that the value of  $(A^2(r) - B^2(r))$  is roughly constant in the range of interest<sup>5</sup>. Note that Equation (4.11) takes a much simpler form in galaxies with flat rotation curves ( $A(r) \simeq -B(r)$ ), as the second term on the right-hand side vanishes.

### 4.1.2 Examples of systems with spherical geometry

As was discussed in Section 2.1, our Galaxy can be roughly divided into three components: a disc component (can be further decomposed into the *thin* and the *thick* discs), the bulge at the centre and an halo (composed of stars and dark matter) around the disc. Consequently, it is interesting and illustrative to see a few examples of solutions of the Poisson equation for both spherical and cylindrical geometries.

**Plummer model** There are some systems that are adequately described by a mass density distribution  $\rho$  roughly constant up to radius  $b$  and then smoothly decreasing to zero in the limit of large radii. The Plummer model is a potential with these properties and it is given by:

$$\Phi(r) = -\frac{GM}{\sqrt{r^2 + b^2}}, \quad (4.12)$$

where  $G$  is the constant of gravitation,  $b$  is a scale length setting the linear scale of the system, and  $M$  is the total mass of the system. From Equation (4.4) we can compute the density distribution corresponding to this potential:

$$\rho(r) = \frac{3Mb^2}{4\pi} \frac{1}{(r^2 + b^2)^{5/2}}. \quad (4.13)$$

The potential-density pair given by Plummer's model can be appropriate to describe spherical systems like globular clusters and the bulge of spiral galaxies, for example.

---

<sup>4</sup>The integrated surface mass density within  $\pm Z$  of the disc,  $\Sigma_Z(r)$  is given by:  $\Sigma_Z(r) = \int_{-Z}^Z \rho(r, \theta, z) dz$ . The conventional integration limit is  $|Z| = 1.1$  kpc, so that most of the disc mass is accounted for.

<sup>5</sup>Kuijken and Gilmore (1989) show this approximation is good for the region of interest ( $|z| \lesssim 1.1$  kpc).

**Power-law density models** The luminosity profiles of many galaxies can be approximated by a power-law. This motivates the use of spherical mass density distributions where the density falls off as a power of the radius:

$$\rho(r) = \rho_0 \left( \frac{r_0}{r} \right)^\alpha. \quad (4.14)$$

Since the system represented by this density distribution has spherical symmetry we know that only the mass interior to radius  $R$  matters as far as the system dynamics are concerned. For this reason it is useful to consider the total mass contained in a sphere of given radius. By integrating Equation (4.14) we find:

$$M(r) = \frac{4\pi\rho_0 r_0^\alpha}{3-\alpha} r^{3-\alpha}. \quad (4.15)$$

By Poisson's equation (Equation 4.4), we have:

$$\frac{\partial}{\partial r} \left( r^2 \frac{\partial \Phi}{\partial r} \right) = 4\pi G \rho_0 r_0^\alpha r^{2-\alpha}. \quad (4.16)$$

From the previous equation we can compute the circular speed (Equation 4.6) by integrating once and the potential by integrating twice. The first integration yields:

$$v_c^2 = r \frac{\partial \Phi}{\partial r} = \begin{cases} \frac{4\pi G \rho_0 r_0^\alpha}{3-\alpha} r^{2-\alpha} & \text{for } \alpha \neq 2 \\ 4\pi G \rho_0 r_0^\alpha & \text{for } \alpha = 2 \end{cases} \quad (4.17)$$

So we conclude that when the constant  $\alpha = 2$  the system's rotation curve is flat. From Equation (4.15) we can see that  $\alpha = 2$  implies a total enclosed mass  $M(r) \sim r$ .

Now we can integrate Equation (4.17) between  $r$  and the radius  $r_0$  to find the potential difference:

$$\Phi(r) - \Phi(r_0) = \begin{cases} \frac{v_c^2(r_0) - v_c^2(r)}{\alpha-2} & \text{for } \alpha \neq 2 \\ v_c^2 \ln(r/r_0) & \text{for } \alpha = 2 \end{cases} \quad (4.18)$$

### 4.1.3 Examples of systems with cylindrical geometry

**Kuzmin model** The simplest model of a disc is one where the mass is distributed only in the plane perpendicular to the axis of symmetry. The potential generated by such infinitely thin disc can be written (in cylindrical coordinates) as:

$$\Phi(r, z) = -\frac{GM}{\sqrt{r^2 + (a + |z|)^2}} \quad (4.19)$$

with  $a \geq 0$  since its Laplacian  $\nabla^2 \Phi$  is equal to zero for all  $z \neq 0$ . The associated surface density (note that in this case the mass is not distributed in a volume, but only in the plane) is

$$\Sigma_K(r) = \frac{aM}{2\pi(r^2 + a^2)^{3/2}}. \quad (4.20)$$

**Miyamoto-Nagai model** The Miyamoto-Nagai potential is essentially a generalization of the Kuzmin potential. In cylindrical coordinates it is written:

$$\Phi(r, z) = -\frac{GM}{\sqrt{r^2 + (a + \sqrt{z^2 + b^2})^2}}. \quad (4.21)$$

This potential reduces to the Plummer potential (Equation 4.12) when  $a = 0$ , and to the Kuzmin potential when  $b = 0$ . Thus it is possible to model the potential generated by any type of mass distribution, from a thin disk (Kuzmin model) to a spherical system (Plummer model), by choosing appropriate values for the parameters  $a$  and  $b$ . In other words, a low  $b/a$  ratio implies a “disc-like” distribution, whereas a high  $b/a$  ratio implies a “sphere-like” distribution.

The mass density distribution associated with this potential can be computed from Poisson’s equation (Equation 4.4). Thus:

$$\rho(r, z) = \frac{b^2 M}{4\pi} \times \frac{ar^2 + (a + 3\sqrt{z^2 + b^2})(a + \sqrt{z^2 + b^2})^2}{[r^2 + (a + \sqrt{z^2 + b^2})^2]^{5/2} (z^2 + b^2)^{3/2}}. \quad (4.22)$$

It is also relevant to compute the circular speed when  $z = 0$ . From Equation (4.6) we have<sup>6</sup>:

$$v_c^2 = r \frac{d\Phi(r)}{dr} = \frac{r^2 GM}{(r^2 + (a + \sqrt{z^2 + b^2})^2)^{3/2}}. \quad (4.23)$$

## 4.2 The Milky Way gravitational potential

In this section we will describe the construction of the dynamical model of our Galaxy that was used to determine the orbits of stars. Then we discuss the observational constraints that the model must be able to reproduce. After that a discussion on the problem of determination of the disc scale-length follows, whose importance will be explained in the next paragraph. Finally, in the last section we present the model proper, describing the method used to construct it.

The model developed in this section is based on the dynamical mass model created by Allen and Santillan (1991) – hereafter referred to as the *default model* – which has been used as a basis for several dynamical studies (e.g. Irrgang et al., 2010; Ramspeck et al., 2001b). It is constructed as a sum of three independent components corresponding roughly to the bulge, disk, and halo populations, with

<sup>6</sup>Note that  $d\Phi/dz \sim z$ , so only the radial component of the gradient of the potential is non-zero when  $z = 0$ .

the dark mass contribution included in the Halo component. The model successfully reproduces the Galactic rotation curve and its main advantage is the fact that the functional form of the gravitational potential for the three components is quite simple, being also fully analytical, continuous, and with continuous derivatives everywhere. Unfortunately, it was found to be outdated in terms of some of its parameters, in particular the disc scale-length. Hence the inclusion of a discussion on this important parameter. Since the model we developed is an updated version of the model by Allen and Santillan (1991), it will be referred to as the *updated model*. A brief summary of the default model follows.

The first component of the default model (representing the bulge) is a spherical mass distribution, given by the Plummer model (see Equation (4.12)). The potential is given by:

$$\Phi_1(r, z) = -\frac{M_1}{(r^2 + z^2 + b_1^2)^{1/2}}, \quad (4.24)$$

and the density distribution by:

$$\rho_1(r, z) = \frac{3b_1^2 M_1}{4\pi(r^2 + z^2 + b_1^2)^{5/2}}. \quad (4.25)$$

This distribution, as the distribution of the second component (disc), is written in cylindrical galactic coordinates. The units for all three components are kpc for distance, galactic mass units (1 galactic mass unit =  $2.32 \times 10^7 M_\odot$ ) for mass and second for time. In this system of units  $G = 1$ , and velocities are in units of  $100 \text{ km s}^{-1}$ . The free parameters in the first component are  $M_1$ , which is proportional to the total mass of the component, and  $b_1$ , which is a scale length.

The second component (representing the disc) is a mass distribution derived from a Miyamoto-Nagai disk potential (Equation 4.21). It is given by:

$$\rho_2(r, z) = \left( \frac{b_2^2 M_2}{4\pi} \right) \left( \frac{a_2 r^2 + [a_2 + 3(z^2 + b_2^2)^{1/2}] [a_2 + (z^2 + b_2^2)^{1/2}]^2}{[r^2 + [a_2 + (z^2 + b_2^2)^{1/2}]^2]^{5/2} (z^2 + b_2^2)^{3/2}} \right). \quad (4.26)$$

The free parameters are  $M_2$ , which is proportional to the total mass of the component,  $a_2$  and  $b_2$ , are scale lengths, corresponding to the “radial” scale length (sometimes simply called scale length) and the scale height respectively.

The third component (representing the halo) is based on a two-power density type model. In spherical coordinates we have:

$$\rho_3(R) = \frac{M_3}{4\pi a_3 R^2} (R/a_3)^{\gamma-1} \frac{\gamma + (R/a_3)^{\gamma-1}}{[1 + (R/a_3)^{\gamma-1}]^2} \quad (4.27)$$

The free parameters are  $M_3$ , which is proportional to the total mass of the

Table 4.1: Default model parameters.

Component	Mass ( $M_{\odot}$ )	Parameters
Central mass	$1.41 \times 10^{10}$	$M_1 = 606.0$ $b_1 = 0.3873$
Disc	$8.56 \times 10^{10}$	$M_2 = 3690.0$ $a_2 = 5.3178$ $b_2 = 0.2500$
Halo	$8.002 \times 10^{11}$	$\gamma = 2.02$ $M_3 = 4615.0$ $a_3 = 12.0$

component,  $a_3$ , which is a scale length, and the power-law exponent  $\gamma$ . The total mass of this component is given by:

$$M(R) = \frac{M_3 (R/a_3)^\gamma}{1 + (R/a_3)^{\gamma-1}}. \quad (4.28)$$

As seen before, this model has the property that its total mass is proportional to  $R$  for large values of  $R$ , which is needed to guarantee a non-Keplerian rotation curve for the outer parts of the galaxy.

### 4.2.1 Observational constraints

Any dynamical model of our Galaxy must be able to fit a number of observational constraints. These constraints are:

1. The distance from the Sun to the Galactic Centre  $r_0$  (the *solar circle* radius).
2. The measured rotation curve  $v_c(r)$  and the local circular speed  $v_0 = v_c(r_0)$  (speed of the LSR<sup>7</sup>). Note that the  $v_c$  curve depends on the value of  $v_0$ .
3. The values of the Oort constants  $A$  and  $B$ .
4. The total density near the Sun  $\rho(r_0)$ , the total surface density between heights  $z = -1.1$  kpc and  $z = 1.1$  kpc of the Galactic plane near the Sun,  $\Sigma_{1.1}(r_0)$ , and the contribution of the disc component to the latter density.
5. The total mass of the Galaxy within a radius of 100 kpc

<sup>7</sup>The Local Standard of Rest (LSR) is an inertial frame of reference centered on the Sun which rotates with the local circular speed around the Galactic Centre in the direction of Galactic rotation.

The quantities  $r_0$ ,  $v_0$  and the Oort constants  $A$  and  $B$ , are all interrelated because  $v_0/r_0 = A - B$ <sup>8</sup>. Hence the determination of the local circular speed and distance to the Galactic Centre constrains the value of the Oort constants, and vice-versa. A review of various distance determination methods by Reid (1993) suggests a value of  $r_0 = 8.0 \pm 0.5$  kpc for the distance to the Galactic Centre. Moreover, a direct measurement of this distance was made by Eisenhauer et al. (2003) by observing the orbit of a star around the massive black hole in the Galactic Centre, and its value is  $r_0 = 7.94 \pm 0.42$  kpc. Observations of the proper motion of the massive black hole also allowed Reid et al. (1999) to determine a local circular speed value of  $v_0 = 219 \pm 20$  km s<sup>-1</sup>. However, some authors favour higher values for the local circular speed, for example, Miyamoto and Zhu (1998) suggests  $v_0 = 268.7 \pm 11.9$  km s<sup>-1</sup> (assuming  $r_0 = 8.5$  kpc), derived from the proper motions of a sample of Hipparcos O-B stars. Nevertheless, from the Hipparcos proper motions of a sample of Cepheid stars, Feast and Whitelock (1997) derives an angular velocity  $\Omega_0 = v_0/r_0 = 27.19 \pm 0.87$  km s<sup>-1</sup> kpc<sup>-1</sup> (corresponding to a local circular speed  $v_0 \simeq 218$  km s<sup>-1</sup> for a value of  $r_0 = 8$  kpc), and Oort constants  $A = 14.82 \pm 0.84$  km s<sup>-1</sup> kpc<sup>-1</sup> and  $B = -12.37 \pm 0.64$  km s<sup>-1</sup> kpc<sup>-1</sup>.

The traditional value of the local circular speed used in studies of the Galaxy's rotation curve is  $v_0 = 220$  km s<sup>-1</sup>. Using this value, Fich et al. (1989) and Brand and Blitz (1993) derive a rotation curve from observations of CO sources and HII regions, respectively. These studies suggest that the rotation curve is approximately flat up to a distance of  $\sim 17$  kpc from the Galactic Centre.

The local mass density obtained by Creze et al. (1998) from a sample of Hipparcos A stars was  $\rho_0 = 0.076 \pm 0.015$  M<sub>⊙</sub> pc<sup>-3</sup>. On the other hand, Holmberg and Flynn (2000) obtained  $\rho_0 = 0.102 \pm 0.010$  M<sub>⊙</sub> pc<sup>-3</sup> from a sample of Hipparcos A and F stars.

The local surface density between heights  $z = -1.1$  kpc and  $z = 1.1$  kpc determined by Holmberg and Flynn (2004) from a sample of Hipparcos K giant stars was  $\Sigma_{1.1}(r_0) = 74 \pm 6$  M<sub>⊙</sub> pc<sup>-2</sup>. The dynamical contribution of the disc to this total was estimated to be  $56 \pm 6$  M<sub>⊙</sub> pc<sup>-2</sup>, which is comparable to an estimated  $53$  M<sub>⊙</sub> pc<sup>-2</sup> in visible matter. This result agrees quite well with a study by Kuijken and Gilmore (1991), who obtained the estimate  $\Sigma_{1.1}(r_0) = 71 \pm 6$  M<sub>⊙</sub> pc<sup>-2</sup> from a study of K dwarf stars. This time, the estimated contribution from the disc was  $48 \pm 9$  M<sub>⊙</sub> pc<sup>-2</sup>.

Estimates of the total mass of Galaxy have a very wide range: Wilkinson and Evans (1999) estimates  $M_{\text{halo}} \sim 1.9_{-1.7}^{+3.6} \times 10^{12}$  M<sub>⊙</sub>, Smith et al. (2007) estimates  $M_{\text{halo}} \sim 1.42_{-0.54}^{+1.14} \times 10^{12}$  M<sub>⊙</sub>, and Xue et al. (2008) estimates  $M_{\text{halo}} \sim 1.0_{-0.2}^{+0.3} \times 10^{12}$  M<sub>⊙</sub>. Other estimates are reviewed by Xue et al. (2008).

After considering all these studies, the estimates of the observational constraints adopted in our study were:  $r_0 = 8$  kpc,  $v_0 = 220$  km s<sup>-1</sup>,  $A = 14.8 \pm 0.8$  km s<sup>-1</sup> kpc<sup>-1</sup>,  $B = -12.4 \pm 0.6$  km s<sup>-1</sup> kpc<sup>-1</sup>,  $\rho_0 = 0.102 \pm 0.010$  M<sub>⊙</sub> pc<sup>-3</sup>,

<sup>8</sup>This is only strictly true under the assumptions that the potential is axisymmetric and that the spatial distributions are smooth (Olling and Dehnen, 2003).

$\Sigma_{1.1}(r_0) = 74 \pm 6 \text{ M}_\odot \text{ pc}^{-2}$  and  $M_{\text{halo}} \sim 1 \times 10^{12} \text{ M}_\odot$ . We also assumed an approximately flat rotation curve. We gave higher priority to: direct measurements, measurements relying on Hipparcos data (for consistency), and lower measurement errors.

### 4.2.2 Scale lengths

The distribution of star density within the disc (as a function of the distance to the centre) is usually described, in observational studies, by an exponential law (Jurić et al., 2008 and references therein) of the type:

$$\rho(r) \sim e^{-\frac{r}{h_r}}, \quad (4.29)$$

where  $h_r$  is the scale length. Thus, when  $r = h_r$  the density has decreased by  $e^{-1}$  relative to its value in the centre. The parameter  $a_2$  in Equation (4.26) has the same property and also functions as a scale length.

The parameters  $M_2$ ,  $a_2$  and  $b_2$  of the default model were determined in the following way (Allen and Santillan, 1991):  $M_2$  and  $(a_2 + b_2)^2$  were obtained from a fit to the Galactic rotation curve, then individual solutions for  $a_2$  and  $b_2$  were obtained from Equation (4.26), by substitution, assuming a local density of  $0.15 \text{ M}_\odot \text{ pc}^{-3}$  (cf. Table 4.1). The scale length obtained after this procedure was  $a_2 = 5.3178 \text{ kpc}$ .

However, most recent studies have systematically found a smaller scale length. Drimmel and Spergel (2001) found  $h_r \sim 2.25 \text{ kpc}$  from a fit of a dust model to near and far-infrared data. Robin et al. (2003) found  $h_r = 2.5 \pm 0.5 \text{ kpc}$  from a fit of a dynamical model to Hipparcos data. Jurić et al. (2008) found  $h_r = 2.6 \pm 0.5 \text{ kpc}$  for a thin disc component, and  $h_r = 3.6 \pm 0.7 \text{ kpc}$  for a thick disc component, from a direct fit to stellar counts of M dwarfs detected by the Sloan Digital Sky Survey (SDSS). Finally, Sale et al. (2010) found  $h_r = 3.0 \pm 0.3 \text{ kpc}$  from a direct fit to stellar counts of A dwarfs detected by the INT/WFC Photometric H $\alpha$  Survey of the Northern Galactic Plane (IPHAS).

The larger scale length obtained by Allen and Santillan (1991) was probably a result of an overestimation of the local mass density, because, as we have seen, more recent estimates point to a value of  $\rho_0 = 0.102 \pm 0.010 \text{ M}_\odot \text{ pc}^{-3}$ , or less (cf. Section 4.2.1). For this reason, we decided to adopt the value  $h_r = 3 \text{ kpc}$  for the scale length (also note that we are assuming only one disc component that represents both the thin and the thick discs). By assuming this scale length, a value for the local density, and a value for the local circular speed, we were able to obtain the parameter  $M_2$  (and other parameters), essentially inverting the method used by Allen and Santillan (1991).

### 4.2.3 Gravitational potential model

In this section we finally describe the method used to construct the updated model, and the model itself.

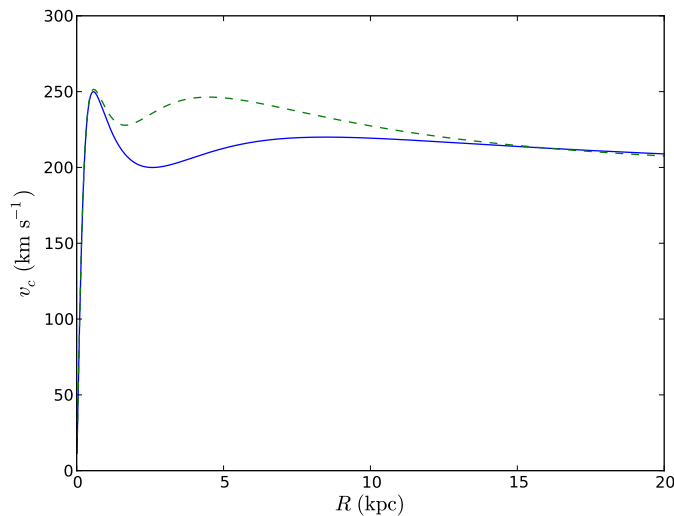
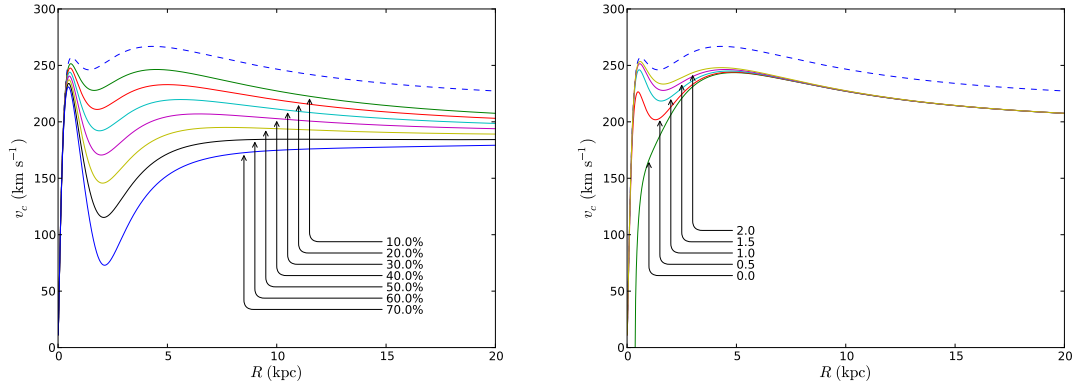


Figure 4.1: Plot comparing the rotation curves of the original default model (solid line) and the default model with the shorter scale length  $h_r = 3$  kpc (dashed line).

The reduction of the scale length created a problem: as the mass is now much more concentrated towards the centre, the velocity curve starts to deviate from the desired flatness (see Figure 4.1). This effect can be counterbalanced by reducing the value of the  $M_2$  parameter, but only at the expense of reducing the local mass density and local circular speed down to values much below the observed ones.

As a means of reducing the mass concentrated near the centre of the galaxy we introduced a second disk component, with negative mass, analogous to the “hole” component used by Robin et al. (2003) in their mass model. In this case this component can also be thought as a “hole” in the original disc, at least in the sense that the disc density is greatly reduced in the central regions. This new component has a functional form equal to the “real” disc component, hereafter “first disc component”, only with a negative sign, which ensures that we keep the simplicity and good mathematical properties of the default model. We designate the new disc component by “second disc component”. The second disc component was implemented as a new distribution of the form given by Equation (4.26), but with a negative sign. The disc component in the updated model is then the sum of the first and second disc components. To avoid undesirable physical consequences, special attention is required to ensure that the total mass density is positive everywhere. To distinguish the parameters of the first and second disc components a superscript with the number 1 or 2, respectively, is used.

The procedure adopted to construct the updated model consisted in fitting some of the model parameters to the observational constraints (cf. Section 4.2.1). Instead of fitting the model to all the observational constraints at the same time we used an approach similar to the one used by Allen and Santillan (1991) and fitted the model to the local mass density and local circular speed only (for the assumed galactocentric distance). The other observational constraints were compared with the values given by the model in the end to check for consistency. Moreover, since



(a) Influence of the second component's mass.

(b) Influence of the second component's scale length.

Figure 4.2: Preliminary study of the sensitivity of the circular speed curve to the second disc component parameters  $M_2^2$  and  $a_2^2$ . In (a) we have rotation curves resulting from a  $M_2^2$  parameter varying between 10 and 70 per cent of  $M_2^1$ . In (b) we have rotation curves resulting from a  $a_2^2$  parameter varying between 0 and 2 kpc.

only the disc and halo components were expected to have a large influence in the outcome, we fitted only the  $M_2^2$ ,  $a_2^2$ ,  $M_2^1$ ,  $M_3$  and  $\gamma$  parameters. A more detailed explanation of the procedure follows:

1. the first disc component scale length,  $a_2^1$  was set to 3 kpc, for the reason explained before.
2. the second disc component was established first, by choosing suitable parameters to satisfy two conditions: reduce the disc mass accumulated in the centre by as much as possible, while keeping the rotation curve as flat as possible in the region between 5 – 20 kpc. The scale height was kept fixed and equal to the one in the first disc component. The parameter  $M_2^2$  was chosen to be a percentage of the parameter  $M_2^1$ .
3. keeping the second disc and bulge components fixed, a first attempt at fitting a flat curve on the interval 5 – 20 kpc, and slowly decreasing until 100 kpc, by varying the first disc mass (parameter  $M_2^1$ ), and the halo component mass and power law exponent (parameters  $M_3$  and  $\gamma$ , respectively). The estimate obtained for the parameter  $M_3$  resulting from this fit was taken as definitive.
4. finally, estimates of the  $\gamma$  and  $M_2^1$  (and so also of  $M_2^2$ ) parameters were obtained by simultaneously fitting a flat curve on the interval 5 – 20 kpc, imposing the observed local circular velocity, and the observed local density.

The second disc component parameters were  $a_2^2$ ,  $b_2^2$ , and  $M_2^2$ . These parameters were chosen in the beginning with the purpose of defining a second disc component capable of solving the aforementioned mass concentration problem, and avoiding negative density in the centre. A preliminary study of the sensitivity of the circular speed curve to these parameters was done with the goal of finding parameters

Table 4.2: Physical quantities that were used to constraint the parameters of the models, compared with the measured values.

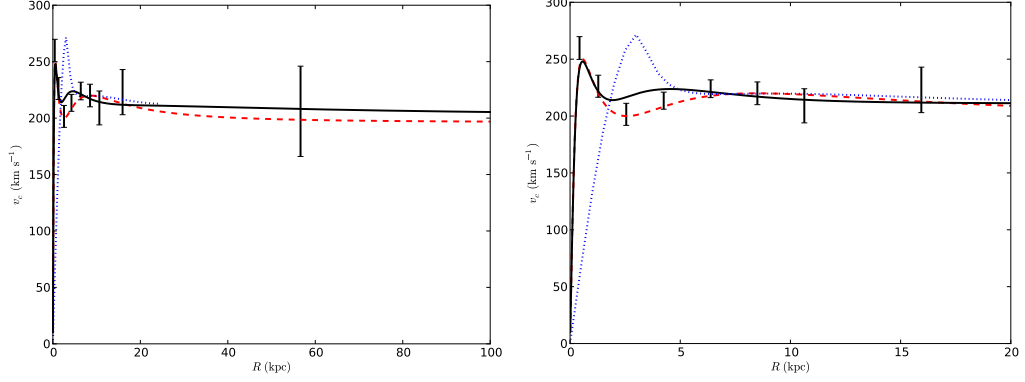
	default		updated		reference
	model		model		values
$r_0$ (kpc)	8.5	8.0	8.5	8.0	8.0
$\rho_0$ ( $M_\odot \text{ pc}^{-3}$ )	0.15	0.16	0.096	0.112	$0.102 \pm 0.010$
$v_c^0$ ( $\text{km s}^{-1}$ )	220	220	217	218	220

capable of fulfilling these requirements. After setting the  $a_2^1$  scalelength to 3 kpc, the  $M_2^2$  parameter of the second disc component was made to vary between the percentages of 10 – 70 per cent, as can be seen in Figure 4.2. In the same manner, we varied the parameter  $a_2^2$  in the interval 0 – 2 kpc, as shown in Figure 4.2. The method adopted was of an iterative nature, initial values for  $a_2^2$  and  $M_2^2$  were chosen and, in the event of obtaining an unsatisfactory result in the end, changed in the next iteration of the procedure. The initial choice for  $M_2^2$  was of 10 per cent of  $M_2^1$ , as this appeared to be enough to bring the rotation curve down to acceptable values (see Figure 4.2 (a)). The parameter  $a_2^2$  has little influence on the rotation curve, with the exception of the inner 3 kpc, as can be seen in Figure 4.2 (b). The initial choice was  $a_2^2 = 1.5$  kpc, to avoid an excessive concentration of “negative mass” in the centre. In the end, we were able to obtain a good overall fit so we did not perform another iteration of this step and so this were the final choices.

The  $M_3$  parameter was obtained by fitting the rotation curve (with the second disc component already included) to a set of artificial points equal to  $220 \text{ km s}^{-1}$  in regular intervals up to 20 kpc, and to  $210 \text{ km s}^{-1}$ , in regular intervals, after that and up to 100 kpc, to find a flat curve consistent with the observed local circular velocity and slowly decreasing for large distances. The curve was fitted by varying  $M_3$ ,  $\gamma$  and  $M_2^1$ , as mentioned before. This first fit was performed using an implementation of the Levenberg-Marquardt algorithm in the script language PYTHON called CURVEFIT, part of the SCIPY package.

The parameters  $M_2^1$  and  $\gamma$  were obtained by fitting the rotation curve, given the  $M_3$  value computed in the previous step, to artificial points, equal to  $220 \text{ km s}^{-1}$  in regular intervals, up to 20 kpc, and to the observed local density and local circular velocity (Table 4.2). The simultaneous fit to these three different constraints was realised using an implementation of the Nelder-Mead simplex algorithm in PYTHON called FMIN, part of the SCIPY package. The fit to a flat curve, the value of the circular velocity and the value of the local density were given weights of 75, 20 and 5 per cent respectively.

A summary of the updated model parameters, obtained through the described fitting procedure, can be seen in Table 4.3, together with the mass of each component. The quality of the model can be judged from Figure 4.3 and from Table 4.4. In Figure 4.3 we can see a comparison between the updated model and the default and Robin et al. (2003) models. The updated model behaves similarly to the others in the critical region between 5 – 20 kpc. Within 5 kpc the behaviour is



(a) Rotation curve up to a 100 kpc radius. (b) Rotation curve up to a 20 kpc radius.

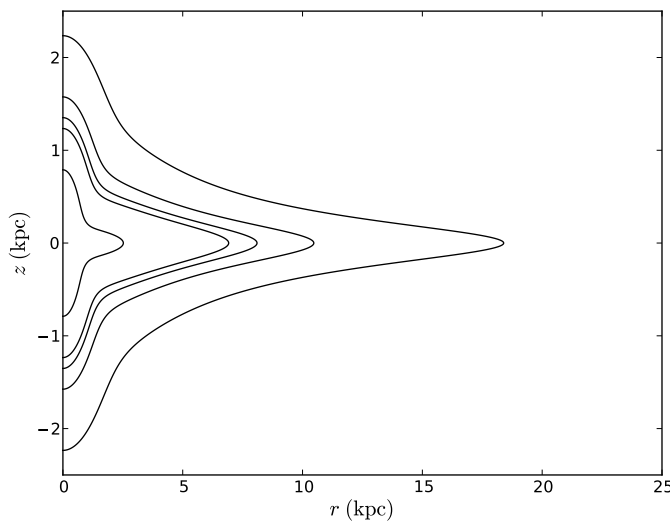
Figure 4.3: Plot of the circular velocity as a function of radius. The dashed line corresponds to the default model, the dotted line corresponds to the Robin et al. (2003) model, the solid line corresponds to the updated model, and the error bars are data points from Fich et al. (1989).

Table 4.3: Updated model parameters and total masses derived for each component.

Component	Mass ( $M_{\odot}$ )	Parameters
Central mass	$1.41 \times 10^{10}$	$M_1 = 606.0$ $b_1 = 0.3873$
First disk	$7.14 \times 10^{10}$	$M_2^1 = 3079.0$ $a_2^1 = 3.0$ $b_2^1 = 0.25$
Second disk	$7.14 \times 10^9$	$M_2^2 = 307.9$ $a_2^2 = 1.5$ $b_2^2 = 0.25$
Halo	$9.00 \times 10^{11}$	$\gamma = 2.79$ $M_3 = 4761.1$ $a_3 = 12.0$

Table 4.4: Comparison of physical quantities computed from the model with measured values.

	default		updated		reference
	model		model		values
$r_0$ (kpc)	8.5	8.0	8.5	8.0	8.0
$\Sigma_0$ ( $M_\odot \text{pc}^{-2}$ )	83	93	62	71	$74 \pm 6$
$A$ ( $\text{km s}^{-1} \text{kpc}^{-1}$ )	13.0	13.5	13.6	14.5	$14.8 \pm 0.8$
$B$ ( $\text{km s}^{-1} \text{kpc}^{-1}$ )	-12.9	-13.9	-11.9	-12.7	$-12.4 \pm 0.6$
$v_e^0$ ( $\text{km s}^{-1}$ )	536	541	550	555	$550 \pm 50$
$M_{\text{total}}$ ( $M_\odot$ )	$9.00 \times 10^{11}$		$1.00 \times 10^{12}$		$\simeq 1.00 \times 10^{12}$

Figure 4.4: Density contours of the updated model. The density levels correspond to the densities 1, 0.15, 0.1, 0.05 and  $0.01 M_\odot \text{pc}^{-3}$  as we move away from the centre.

similar to the default model, which should not be surprising, since it based on it. Note in particular that the agreement with the observed data points is quite good, although no effort was made to fit them directly. In Figure 4.4 we can verify that the density contours of the bulge and disc components indeed resemble a disc as intended.

In Table 4.4 we can verify that the agreement of quantities computed from the model – local surface density, Oort’s  $A$  and  $B$  constants, escape velocity, and total mass of the Galaxy – is very good, in particular when compared with the performance of the default model. Note that the default model was fine-tuned assuming a distance of the Sun from the Galactic Centre of 8.5 kpc, whereas we assumed a distance of 8.0 kpc. We conclude that the updated model is a better representation of the Galactic gravitational potential than the default model.



# Chapter 5

## Orbit determination

### 5.1 High Galactic latitude runaway stars

#### 5.1.1 Sample selection

Candidate runaway stars were compiled from previous studies. We only selected stars for which a spectroscopic analysis is published, so we could be sure of their main sequence status and know their atmospheric parameters. The quality of the analysis for the different samples is not homogeneous so we found it convenient to separate the list of candidate stars in two groups. We have included in the first group (Group A, Table 5.1) the samples selected from the Palomar-Green (PG) survey (Saffer et al., 1997), the Edinburgh-Cape (EC) survey, and the sample from Ramspeck et al. (2001b). In the second group (Group B, Table 5.2) we have included the samples from the papers by Conlon et al. (1990), Martin (2004), and Behr (2003a).

The “complete” sample of 28 stars selected by Saffer et al. (1997) from the PG survey and the sub-samples, including a “complete” sample of 13 stars, selected by Rolleston et al. (1997), Magee et al. (2001), and Lynn et al. (2004b) from the EC survey, constitute our main sources of candidates since they provide good coverage (in a statistical sense) of both hemispheres. The PG sample was studied in a series of papers: Hambly et al. (1997), Rolleston et al. (1999), and Lynn et al. (2004a). These studies performed high resolution spectroscopic analyses, including the determination of radial velocities and atmospheric parameters, and detailed abundance analyses. The EC sample was similarly studied in the corresponding papers.

We have also included candidates found in four other sources. The sample from Ramspeck et al. (2001b) which is of special interest because it includes many candidates at high distances (up to 7 kpc) from the Galactic plane (if they are indeed on the main sequence). Another important source is the study by Conlon et al. (1992) which contains seven candidates, many of which appear to be at very high distances from the plane (more than 4 kpc).

The sample of Conlon et al. (1990) provides 32 candidates which are also part

of the Hipparcos catalogue. These 32 stars were studied in a series of papers (Keenan et al., 1982; Keenan and Dufton, 1983; Keenan et al., 1986; Conlon et al., 1988). Finally we have included a few candidates found in Martin (2004) and Behr (2003a). Martin (2004) performed an extensive analysis of his candidates. It should be noted that the study by Behr (2003a) focuses on the distribution of the projected rotational velocity of Blue Horizontal Branch stars, hence its atmospheric parameters estimates are not appropriate for the parameter range of runaway stars. It is important to note that there are overlaps between these different samples. The total number of initial candidate stars was then 174.

### 5.1.2 Abundances

An abundance analysis was, in general, part of all the spectroscopic studies. This analysis uses the respective atmospheric parameters estimates and assumes an LTE atmosphere. The abundance pattern permitted us to distinguish MS stars from BHB stars, as the atmospheres of the latter are dominated by diffusion and show strong deviations from the approximately solar mix seen in MS stars. In particular, helium is usually depleted, and metals depleted or enhanced, depending on the evolutionary history, and balance between the effects of diffusion and levitation of the heavier metals due to radiation pressure (Behr, 2005). In the case of PAGB stars, some elements can be modified by dredge ups, but the absence of a strong modification of the abundance pattern is usually not conclusive. The abundances found in the literature were compared with the normal abundances for B stars, found in Kilian (1992, 1994).

Table 5.1: Group A stars, including stars from the Palomar-Green (PG) survey (Saffer et al., 1997), the Edinburgh-Cape survey, and the sample from Ramspeck et al. (2001b). The “?” symbol indicates no data was available, whereas a “(?)” is used to distinguish cases where a MS status is less well established. One  $\checkmark$  corresponds to  $40 \text{ km s}^{-1} \leq v \sin i < 70 \text{ km s}^{-1}$ , two  $\checkmark$  correspond to  $70 \text{ km s}^{-1} \leq v \sin i < 150 \text{ km s}^{-1}$ , and three  $\checkmark$  to  $v \sin i > 150 \text{ km s}^{-1}$ .

Name	Parallax < $2\sigma$	$v \sin i$	Consistent abundances	Inconsistent with PAGB nature	Verdict	References
PG 0122+214	?	$\checkmark\checkmark$	Yes	Yes	MS	(6),(7)
PG 1511+367	?	$\checkmark\checkmark\checkmark$	Yes	Yes	MS	(6)
PG 1533+467	?	$\checkmark\checkmark\checkmark$	Yes	Yes	MS	(6)
PG 1610+239	?	$\checkmark\checkmark$	Yes	Yes	MS	(6)
PHL 159	?	-	?	Yes	MS (?)	(6)
PHL 346	?	$\checkmark$	Yes	No	MS	(6)
SB 357	?	$\checkmark\checkmark\checkmark$	Yes	Yes	MS	(2),(6)
BD -15 115	Yes	-	Yes	Yes	MS	(2),(5),(6),(8)
HS 1914+7139	?	$\checkmark\checkmark\checkmark$	Yes	Yes	MS	(6)
PG 0009+036	?	$\checkmark\checkmark\checkmark$	?	Yes	MS	(3)
PG 0855+294	?	$\checkmark\checkmark$	Yes	Yes	MS	(3),(7)
PG 0914+001	?	$\checkmark\checkmark\checkmark$	?	Yes	MS	(3)
PG 0934+145	?	-	No	Yes	Non-MS	(3)
PG 0936+109	?	-	No	Yes	Non-MS	(3)
PG 0954+049	?	?	No	Yes	Non-MS	(3)
PG 0955+291	?	$\checkmark\checkmark\checkmark$	Yes	Yes	MS	(3)
PG 1011+293	?	-	No	Yes	Non-MS	(3)
PG 1205+228	Yes	$\checkmark\checkmark\checkmark$	Yes	Yes	MS	(1),(3),(7)
PG 1209+263	?	$\checkmark\checkmark$	No	Yes	MS	(3)
PG 1212+369	?	?	No	?	Non-MS	(3)

Continued on next page

Table 5.1 – continued from previous page

Name	Parallax < $2\sigma$	$v \sin i$	Consistent abundances	Inconsistent with PAGB nature	Verdict	References
PG 1213+456	?	?	No	Yes	Non-MS	(3)
PG 1243+275	?	?	No	No	Non-MS	(3)
PG 1310+316	?	?	No	Yes	Non-MS	(3)
PG 1332+137	Yes	✓✓	Yes	Yes	MS	(3),(7),(8)
PG 1351+393	?	?	No	Yes	Non-MS	(3)
PG 2111+023	?	✓✓	Yes	Yes	MS	(3)
PG 2120+062	?	-	Yes	No	Non-MS	(3)
PG 2128+146	?	-	No	No	Non-MS	(3)
PG 2134+049	?	-	No	No	Non-MS	(3)
PG 2146+087	?	-	No	Yes	Non-MS	(3)
PG 2159+051	?	-	No	Yes	Non-MS	(3)
PG 2214+184	?	-	No	Yes	Non-MS	(3)
PG 2219+094	?	✓✓✓	Yes	Yes	MS	(3),(6),(7)
PG 2229+099	?	-	No	Yes	MS (?)	(3)
PG 2237+178	?	?	?	?	?	(3)
PG 2345+241	?	-	Yes	Yes	MS	(3),(7)
PG 2351+198	?	-	No	Yes	Non-MS	(3)
PG 2356+167	?	-	No	Yes	Non-MS	(3)
EC 04420-1908	?	✓✓✓	Yes	Yes	MS	(5)
EC 01483-6804	?	-	No	No	Non-MS	(5)
EC 05515-6231	?	✓	No	Yes	MS (?)	(5)
EC 06012-7810	?	-	No	Yes	Non-MS	(5)
EC 09470-1433	?	-	Yes	Yes	Non-MS	(5)
EC 19071-7643	Yes	-	Yes	Yes	MS	(5)
EC 19337-6743	No	✓✓✓	Yes	Yes	MS	(5)
EC 19476-4109	Yes	✓✓	Yes	Yes	MS	(5)
EC 19489-5641	?	?	?	?	?	(5)
EC 19490-7708	?	-	No	Yes	Non-MS	(5)
EC 19579-4259	?	-	No	Yes	Non-MS	(5)
EC 19586-3823	?	✓✓✓	Yes	Yes	MS	(5)
EC 19596-5356	?	✓✓✓	Yes	Yes	MS	(9)
EC 20011-5005	?	-	Yes	Yes	MS	(5)
EC 20089-5659	?	✓✓	Yes	Yes	MS	(5)
EC 20104-2944	?	✓	Yes	Yes	MS	(5)
EC 20252-3137	?	✓	No	Yes	MS (?)	(5)
EC 20485-2420	?	-	No	No	Non-MS	(5)
EC 03240-6229	?	✓✓✓	Yes	Yes	MS	(4)
EC 03462-5813	Yes	✓✓✓	Yes	Yes	MS	(4)
EC 05229-6058	?	-	No	No	Non-MS	(4)
EC 05438-4741	?	-	Yes	Yes	MS	(4)
EC 05490-4510	?	-	No	Yes	MS (?)	(4)
EC 05515-6107	?	✓✓✓	Yes	Yes	MS	(4)
EC 05582-5816	?	✓✓✓	Yes	Yes	MS	(4)
EC 06387-8045	?	✓✓✓	Yes	Yes	MS	(4)
EC 09414-1325	?	✓✓✓	Yes	Yes	MS	(4)
EC 09452-1403	?	✓✓	?	Yes	MS (?)	(4)
EC 10087-1411	?	✓✓✓	Yes	Yes	MS	(4)
EC 10500-1358	?	✓✓	Yes	Yes	MS	(4)
EC 10549-2953	?	✓✓✓	Yes	Yes	MS	(4)
EC 11074-2912	?	-	No	Yes	Non-MS	(4)
EC 13139-1851	?	✓	Yes	Yes	MS	(4)
EC 20140-6935	Yes	✓	Yes	Yes	MS	(4)
EC 20153-6731	?	✓✓	Yes	Yes	MS	(4)
EC 20292-2414	Yes	✓✓✓	Yes	Yes	MS	(4)
EC 20411-2704	?	-	Yes	Yes	Non-MS	(4)
EC 23169-2235	?	✓✓	Yes	Yes	MS	(4)

References: (1) Conlon et al. (1990); (2) Conlon et al. (1992); (3) Saffer et al. (1997); (4) Rolleston et al. (1997); (5) Magee et al. (2001); (6) Ramspeck et al. (2001b); (7) Behr (2003a); (8) Martin (2004); (9) Lynn et al. (2004b).

Table 5.2: Group B stars, including the samples from the papers of Conlon et al. (1990), Martin (2004), and Behr (2003a). The symbols have the same meaning as in Table 5.1.

Name	Parallax < $2\sigma$	$v \sin i$	Consistent abundances	Inconsistent with PAGB nature	Verdict	References
PB 5418	?	✓	Yes	Yes	MS	(2)
Ton S 195	?	-	No	Yes	Non-MS	(2)
Ton S 308	?	✓✓	Yes	Yes	MS	(2)
PHL 2018	?	✓✓✓	Yes	Yes	MS	(2)
BD -2 3766	Yes	✓✓✓	Yes	Yes	MS	(2),(8)
BD +00 0145	?	-	No		Non-MS	(7)
BD +36 2242	Yes	✓✓	?	Yes	MS (?)	(7)
HD 7374	No	-	?	Yes	Non-MS	(7)
HD 27295	No	-	?	Yes	Non-MS	(7)
HD 128801	No	-	No	Yes	Non-MS	(7)
HD 135485	No	-	No	Yes	Non-MS	(7)
PG 1530+212	?	✓✓	?	Yes	MS (?)	(7)
HIP 1241	Yes	✓✓	No	Yes	MS (?)	(7),(8)
HIP 1511	Yes	-	No	Yes	Non-MS	(8)
HIP 1904	Yes	?	Yes	Yes	MS	(1)
HIP 2702	Yes	-	Yes	Yes	MS	(1),(5)
HIP 3812	Yes	✓✓✓	Yes	Yes	MS	(1),(5)
HIP 6419	Yes	?	?	Yes	?	(1),(8)
HIP 11809	Yes	✓✓✓	Yes	Yes	MS	(1),(8)
HIP 11844	Yes	✓✓	Yes	Yes	MS	(8)
HIP 12320	Yes	✓✓✓	Yes	Yes	MS	(1),(8)
HIP 13800	Yes	-	Yes	Yes	MS	(2),(7)
HIP 15967	Yes	-	No	Yes	Non-MS	(8)
HIP 16130	Yes	✓	Yes	Yes	MS	(1),(8)
HIP 16466	No	-	Yes	Yes	Non-MS	(1)
HIP 16758	Yes	✓✓	No	No	MS (?)	(1),(5)
HIP 28132	Yes	✓✓	Yes	Yes	MS	(8)
HIP 37903	Yes	✓✓✓	Yes	No	MS	(8)
HIP 41979	Yes	-	No	Yes	Non-MS	(8)
HIP 45904	Yes	✓✓✓	No	Yes	MS (?)	(7),(8)
HIP 48394	Yes	✓✓✓	No	Yes	MS (?)	(8)
HIP 50750	Yes	?	?	Yes	?	(8)
HIP 51624	Yes	?	?	No	?	(1)
HIP 52906	Yes	✓✓✓	Yes	Yes	MS	(1),(8)
HIP 55051	Yes	✓✓✓	?	No	MS (?)	(1)
HIP 55461	Yes	✓✓	Yes	Yes	MS	(1),(7),(8)
HIP 56322	Yes	✓✓✓	Yes	Yes	MS	(7),(8)
HIP 58046	Yes	✓✓✓	Yes	Yes	MS	(1),(7),(8)
HIP 59067	Yes	✓✓	Yes	Yes	MS	(1),(7),(8)
HIP 59955	Yes	✓✓✓	Yes	Yes	MS	(1),(8)
HIP 60578	Yes	-	?	Yes	?	(7),(8)
HIP 60615	Yes	✓	No	Yes	Non-MS	(1),(7),(8)
HIP 61800	Yes	✓✓✓	Yes	Yes	MS	(8)
HIP 65388	Yes	-	No	Yes	Non-MS	(8)
HIP 69247	Yes	-	No	Yes	Non-MS	(8)
HIP 70275	Yes	✓	?	Yes	MS (?)	(1),(7),(8)
HIP 71667	Yes	✓✓	?	Yes	MS (?)	(7),(8)
HIP 75577	Yes	-	Yes	Yes	Non-MS	(7),(8)
HIP 76161	Yes	?	Yes	No	MS (?)	(8)
HIP 77131	Yes	✓✓✓	No	No	MS (?)	(8)
HIP 77716	Yes	-	No	No	Non-MS	(7),(8)
HIP 79649	No	✓✓	Yes	Yes	MS (?)	(1),(8)
HIP 81153	Yes	✓✓	No	No	MS (?)	(8)
HIP 82236	Yes	?	?	Yes	?	(8)
HIP 96130	No	✓	Yes	Yes	MS (?)	(8)
HIP 98136	Yes	✓✓	Yes	No	MS (?)	(8)
HIP 104931	Yes	?	?		?	(8)
HIP 105912	Yes	✓✓	Yes	No	MS (?)	(1)
HIP 107027	Yes	✓✓✓	Yes	No	MS (?)	(1),(8)
HIP 108215	Yes	✓✓✓	Yes	Yes	MS	(1)
HIP 109051	Yes	✓✓	Yes	Yes	MS	(8)
HIP 111396	Yes	-	Yes	Yes	MS	(1),(7),(8)

Continued on next page

Table 5.2 – continued from previous page

Name	Parallax < $2\sigma$	$v \sin i$	Consistent abundances	Inconsistent with PAGB nature	Verdict	References
HIP 111563	Yes	✓✓	Yes	No	MS (?)	(1)
HIP 112790	Yes	✓✓	Yes	Yes	MS	(1),(8)
HIP 113735	Yes	?	Yes	Yes	MS	(1)
HIP 114569	Yes	✓✓	No	Yes	MS (?)	(1),(8)
HIP 114690	Yes	✓✓✓	Yes	Yes	MS	(1)
HIP 115347	Yes	-	Yes	No	MS (?)	(1)
HIP 115729	Yes	-	Yes	Yes	MS	(1),(7),(8)

References: (1) Conlon et al. (1990); (2) Conlon et al. (1992); (3) Saffer et al. (1997); (4) Rolleston et al. (1997); (5) Magee et al. (2001); (6) Ramspeck et al. (2001b); (7) Behr (2003a); (8) Martin (2004); (9) Lynn et al. (2004b).

### 5.1.3 Temperature and surface gravity

Temperatures and gravities were computed from Strömberg  $uvby\beta$  photometry (Moon and Dworetzky, 1985 calibration; recalibrated and implemented by Napitowitzki et al., 1993) whenever it was available. This technique is based on the use of two colour indices (Strömberg, 1966):

1. the  $\beta$  index which measures the magnitude difference corresponding to the ratio of intensities measured by a set of filters centered on the  $H_\beta$  Balmer line with 30 Å and 150 Å, respectively;
2. the  $c_1 = (u - v) - (v - b)$  index which measures the size of the Balmer *jump*, i.e. the discontinuity in a star's spectrum *spectrum* at the wavelength corresponding to the ionisation energy of the first excited state of the hydrogen atom.

It has been shown (Moon and Dworetzky, 1985 and references therein) that, in early type stars, the index  $\beta$  is a good indicator of the surface gravity (because of changes in the wings of the  $H_\beta$  line caused by pressure broadening), whereas the index  $c_1$  is a good indicator of the effective temperature (because in hot stars the size of the Balmer jump depends on the fraction of hydrogen atoms in the first excited state, and thus mainly on the ionisation of hydrogen). The main sources of photometry were Hauck and Mermilliod (1998) and Mooney et al. (2000), the latter concentrating only on stars from the PG survey.

The temperature and gravity estimates obtained in spectroscopic studies were also considered, whenever available. These estimates always assume LTE model atmospheres (with the exception of Lynn et al., 2004b). There are two groups of estimates: those based on medium-resolution spectroscopy and estimates based on high-resolution spectroscopy. Those based on high resolution spectroscopy were preferred, followed by the estimates obtained from the Strömberg  $uvby\beta$  photometry. The assumed errors on  $\log g$  (using the  $\beta$  filter) and  $T_{\text{eff}}$  photometric estimates were of 0.2 dex and 10 per cent, respectively. The errors on  $\log g$  and  $T_{\text{eff}}$  estimates taken from the literature range between  $\simeq 0.1 - 0.25$  and  $\simeq 10 - 20$  per cent, respectively. Martin (2004) estimated  $\log g$  by searching the closest match in a

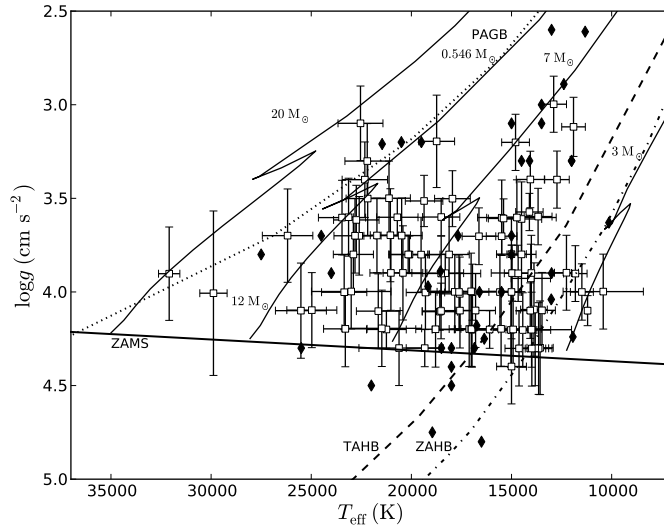


Figure 5.1:  $T_{\text{eff}} - \log g$  diagram. The white squares with error bars represent stars classified as main sequence. The black diamonds represent stars classified as evolved stars, mostly blue horizontal branch. Also shown are theoretical tracks for masses in the range  $3 - 20 M_{\odot}$  (Schaller et al., 1992) as solid lines. The zero age horizontal branch (ZAHB) is shown as a dashed-dotted line and the terminal age horizontal branch (TAHB) is shown as a dashed line, both for a Helium mass fraction of  $Y = 0.247$  and  $[\text{Fe}/\text{H}] = -1.48$  (Dorman et al., 1993). Note that the tracks for the runaway stars are for solar metallicity, in contrast with the (low) metallicity assumed for the HB stars, which is appropriate for halo metal-poor stars. The theoretical track of a PAGB star of  $0.546 M_{\odot}$  (Schönberner, 1979) is shown as a dotted line.

model grid. This method is of low precision since it can easily produce large errors, potentially twice the size of the separation between grid points which was 0.25 dex. Results from other investigations were preferred if available.

#### 5.1.4 Projected rotation velocity

A high projected rotation velocity, or  $v \sin i$ , where  $i$  is the angle between the line of sight and the rotation axis, is an excellent indicator of a young age as old evolved stars do not rotate as fast as young objects. The maximum rotation velocity for a blue HB star appears to be around  $30 - 40 \text{ km s}^{-1}$  (Behr, 2003a). As such, we have considered a star with a projected rotation velocity in excess of  $40 \text{ km s}^{-1}$  to be likely a young object, a star with a projected rotation velocity in excess of  $70 \text{ km s}^{-1}$  to be very likely a young object, and a star with a projected rotation velocity in excess of  $150 \text{ km s}^{-1}$  to be extremely likely a young object. This is noted in Tables 5.1 and 5.2 by 1, 2 or 3 ticks respectively.

It is known that a high rotation velocity will make a star appear cooler and more luminous (lower surface gravity implying a larger radius) if observed at high inclination angles (Frémat et al., 2005; Wenske and Schönberner, 1993). This effect is sometimes called *gravitational darkening* and is caused by the increasing effective gravitational acceleration as a function of the latitude, with the equatorial regions becoming cooler than the polar regions of the star. The selected sample contains

three Be stars: SB 357 (Ramspeck et al., 2001b), PG 0914+001 (Rolleston et al., 1999) and HIP 3812 (Magee et al., 2001). Typical rotation velocities of a Be star are very high (on average 88 per cent of the break-up velocity according to Frémat et al., 2005), we would expect significant effects due to gravitational darkening. Indeed, if the measured surface gravity for PG 0914+001 is taken at face value then the estimated critical velocity ( $v_{\text{crit}} = 273 \text{ km s}^{-1}$ ) will be lower than the measured projected rotation velocity ( $v \sin i = 325 \text{ km s}^{-1}$ ), which strongly suggests that the surface gravity has been underestimated implying a luminosity overestimate. This would also explain the very large distance derived for the star PG 0914+001 of  $\simeq 35 \text{ kpc}$ , based on a low measured surface gravity. Although the gravitational darkening effect is more important in Be stars, because of their high rotation velocity, it should not be ignored in normal B stars as pointed out by Wenske and Schönberner (1993). According to Abt et al. (2002) B stars rotate with velocities of 40 – 50 per cent of the critical velocity on average (depending on the exact spectral type). On the other hand, the effect only becomes significant for velocities greater than  $\simeq 60$  per cent of the critical velocity (Frémat et al., 2005).

We have corrected the Be stars observed temperatures and surface gravities using the theoretical models by Frémat et al. (2005) assuming a rotation velocity of 99 per cent of the break-up velocity. Although there is some indication that many Be stars are actually rotating slower than this (88 per cent is the most probable value according to Frémat et al., 2005, and 70 per cent the lower limit according to Ekström et al., 2008), we know that at least in the case of PG 0914+001 the rotation must be very close to critical because of the high  $v \sin i$ . The case for rotation close to the critical velocity is weaker for the two other Be stars, but the same correction is applied due to consistency considerations. Nevertheless, the difference between a correction assuming a rotation of 99 and 80 per cent of critical velocity is minimal for these two other Be stars ( $\sim 0.1 \text{ dex}$  for  $\log g$  and 1000 K for  $T_{\text{eff}}$ ).

In the case of the normal B stars, the gravitational darkening effect only becomes significant for velocities greater than 60 per cent, as was mentioned previously. Nevertheless, the model for 80 per cent of break-up velocity was preferred because some stars have a projected rotation velocity value incompatible with a rotation velocity lower than 60 per cent of the critical velocity. Both approaches produce similar results (the corrections for  $\log g$  and  $T_{\text{eff}}$  are, on average, 0.1 dex and 400 K for the 60 per cent case, and 0.1 dex and 485 K for the 80 per cent case).

In principle we would like to correct the gravitational darkening effect for all the stars in the sample, but, since the true rotation is unknown for any given star, the correction is done in a statistical sense only. The chosen model implies a very large true rotation velocity (80 per cent of the critical rotation velocity), hence we would overestimate the correction for most stars with small  $v \sin i$  values. To account for this problem we have done the correction only for stars with  $v \sin i$  larger than 35 per cent of the break-up velocity. Moreover, the correction was not applied in cases where rotation velocity measurements were not available (HIP 1904, HIP 113735 and HD 138503), and when the effective temperature was

much higher than the maximum temperature (27000 K) available in the theoretical model grid (HD 140543 and HD 149363).

### 5.1.5 Evolutionary status

In principle, it should be possible to identify main sequence stars from the position they occupy on a  $T_{\text{eff}} - \log g$  diagram, however the region of the diagram which corresponds to O and B stars is crossed by low mass stars in post main sequence evolutionary stages (Tobin, 1987). Low mass stars (initial mass  $M \lesssim 2 M_{\odot}$ ) will evolve to the horizontal branch after the helium flash. Stars in the horizontal branch phase burn helium in the core and hydrogen in a shell. The effective temperature of a star when it enters the horizontal branch will be directly linked to the mass lost during the red giant phase. The Horizontal Branch (hereafter HB) stars which occupy the region of interest ( $10000 \text{ K} < T_{\text{eff}} < 30000 \text{ K}$ ) correspond to the hotter end of this mass sequence and are called Blue Horizontal Branch stars (hereafter BHB stars). The post-HB evolution of these stars depends on the mass of the envelope which determines the strength of the Hydrogen burning shell (Dorman et al., 1993): when the envelope mass is greater than a given critical mass, the star will evolve to the AGB, and after a period of rapid mass loss, it will enter the Post-AGB (hereafter PAGB) phase; on the other hand, when the envelope mass is less than the critical value, the star will either not reach the tip of the AGB, or not even enter the AGB, staying hot until it enters the white dwarf cooling sequence. Since BHB stars have envelopes with small masses they correspond to this second group.

Stars in our sample were classified as main sequence stars or old evolved stars based on their position on the  $T_{\text{eff}} - \log g$  diagram, abundance pattern, projected rotation velocity, and parallax. In Figure 5.1, we show a  $T_{\text{eff}} - \log g$  diagram with the stars that were selected from the initial sample. These are the stars which, to the best of our knowledge, are on or near the main sequence and whose orbits were computed, as described in Section 5.2. Also shown in Figure 5.1 are theoretical tracks for main sequence (hereafter MS) (Schaller et al., 1992), low mass PAGB stars (Schönberner, 1979) and the zero age horizontal branch (Dorman et al., 1993), giving an indication of the regions occupied with stars in different evolutionary stages.

By applying the selection *criteria*, we have classified 96 stars of the initial sample of 174 as being likely or very likely on the main sequence. The remaining 78 stars are most likely halo population, evolved stars, mostly stars on the horizontal branch judged from their position on the  $T_{\text{eff}} - \log g$  diagram. The 96 selected stars have been further classified according to how strong their case for being on the main sequence is. In the more convincing cases there is good evidence for a normal abundance pattern, and/or for high rotation velocity, whereas the less convincing cases either present weaker evidence for normal abundance coupled with low or non-measured rotation velocity. These two cases correspond to the verdicts of MS and MS (?) in Tables 5.1 and 5.2, respectively.

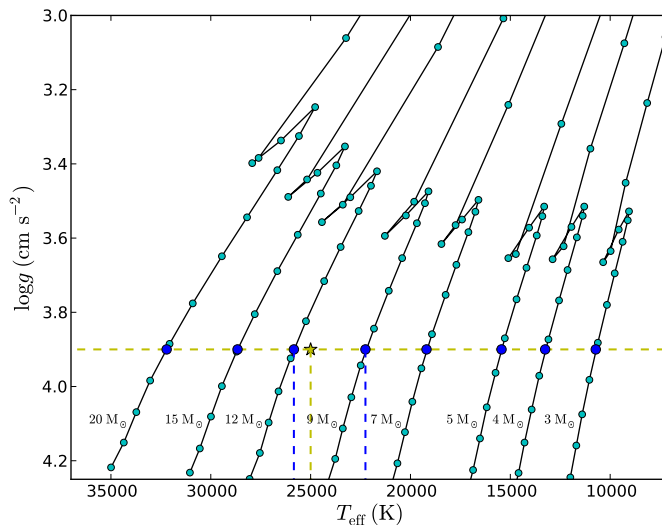


Figure 5.2: Illustration of the interpolation procedure used to obtain estimates of masses and ages. In yellow we have a star with surface gravity  $g_*$  and effective temperature  $T_*$ . The yellow horizontal line (corresponding to the surface gravity  $g_*$ ) crosses the evolutionary tracks (Schaller et al., 1992) in the points marked as blue dots, which were determined by interpolation. The two tracks neighbouring the star can be determined from the position of the star in the temperature sequence represented by the blue dots, as shown by the vertical dashed lines. Having determined the neighbouring tracks, the ages and masses can be obtained by performing a bilinear interpolation in the box enclosing the star (as can be verified in Figure).

The selected sample of high Galactic latitude runaway stars covers a range in magnitudes of  $6.5 < V < 14.5$ , which corresponds to a range in heights above the Galactic plane of  $0.3 - 30.5$  kpc.

### 5.1.6 Age and mass

The masses and ages were obtained by interpolating between the theoretical evolutionary tracks of Schaller et al. (1992) (Schaller tracks). We note that for this reason, the age of a star is more properly termed *evolutionary age*. The tracks were converted from the  $T_{\text{eff}} - L$  plane to the  $T_{\text{eff}} - \log g$  plane. A metallicity corresponding to  $Z = 0.02$  (close to solar) was assumed.

The interpolation procedure, for a star with surface gravity  $g_*$  and effective temperature  $T_*$ , consisted in the following steps (illustrated in Figure 5.2):

1. for every evolutionary track, the effective temperature corresponding to  $g_*$  was computed by doing a linear interpolation along the track, creating a decreasing sequence of temperatures;
2. from the placement of  $T_*$  in that temperature sequence, the two tracks neighbouring the point  $(T_*, g_*)$  were determined;
3. as ages and masses are a function of surface gravities and effective temperature, they were computed by performing a bilinear interpolation in the box

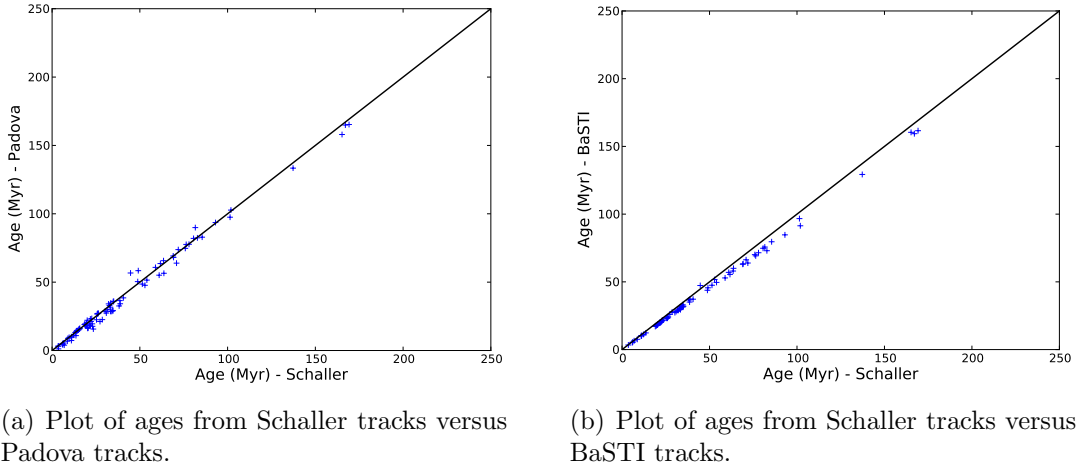


Figure 5.3: Comparison of age estimates for our sample of runaway stars. Ages obtained from Schaller et al. (1992) tracks are compared with ages interpolated from the Padova tracks (Bressan et al., 1993) (a), and the BaSTI tracks (Pietrinferni et al., 2004) (b).

enclosing the point  $(T_*, g_*)$ , formed by two points from the right neighbouring track and two points from the left neighbouring track;

4. in situations of degeneracy (for example when the point lied inside the “hook” in the end of the main sequence), it was assumed that the star was in the longest lasting evolutionary stage.

As a test of the uncertainty caused by different input physics, the evolutionary ages were compared to different estimates obtained using the theoretical tracks by Bressan et al. (1993) (Padova tracks), which are the same as the tracks by Girardi et al. (2000) during the main sequence phase, and to the theoretical tracks by Pietrinferni et al. (2004) (BaSTI tracks). This latter tracks are only available for stars with less than  $10 M_{\odot}$  (note that this covers 80 per cent of the sample). Both comparisons can be seen in Figure 5.3. In the case of the Padova tracks, the relative difference between the two determinations is typically less than 10 per cent for stars older than 50 Myr and less than 20 per cent for stars younger than 50 Myr. Note that the increased discrepancy for younger stars can be partly attributed to the fact that the two models start at different evolutionary stages. In the case of the BaSTI tracks, the relative differences in evolutionary age are typically less than 10 per cent for all stars (masses lower than  $10 M_{\odot}$ ). In both comparisons, the differences can at least partly be explained by the different treatment of the overshooting into the convective layers. Note that these differences between sets of theoretical tracks are in most cases much smaller than the errors in the determination of the evolutionary age, resulting from the uncertainty in the effective temperature and surface gravity determinations.

### 5.1.7 Positions, distances and radial velocities

The distance is one of the most crucial quantities in these type of dynamical analyses. Not only does it define the position in three-dimensional space (together with the coordinates) but also the velocity vector, since the proper motions must be multiplied by the distance to find the tangential velocity component.

The method used to obtain the distances was similar to the one adopted by Napiwotzki (2001):

1. the stellar radius  $R_*$  can be obtained from the estimated surface gravity and mass (Sections 5.1.3 and 5.1.6 respectively), since  $g = G \frac{M}{R_*^2}$ ;
2. the emitted  $V$  band flux at the star's surface,  $F_V$ , was estimated from LTE model atmospheres (Kurucz, 1979), for the estimated effective temperature (Section 5.1.3);
3. the flux received at a distance of 10 pc from the source,  $f_{V;10}$ , is given by  $f_{V;10} = \pi F_V (R_*/10 \text{ pc})^2$ , thus the absolute magnitude,  $M_V$  can be easily computed given an appropriate calibration (Heber et al., 1984);
4. finally, the distances were derived from the distance modulus<sup>1</sup>, given the measured apparent magnitude  $V$ , via

$$d = 10^{\frac{V - M_V + 5}{5}}. \quad (5.1)$$

It is important to note that the apparent magnitudes were corrected for interstellar reddening using either Strömgen  $uvby\beta$  photometry (Napiwotzki et al., 1993 re-calibration for B stars of the Moon and Dworetzky, 1985 original calibration) when available, or the reddening maps of Schlegel et al. (1998). These reddening maps include the total Galactic reddening in any given direction. However we are dealing with stars in the Halo only and most reddening occurs in the disc. This was verified by comparing the Strömgen  $uvby\beta$  photometry reddening estimates with the Schlegel values, which were in good agreement as can be seen in Figure 5.4.

Ideally we would like to test the accuracy of the spectroscopic distance determination by comparing with distances obtained from trigonometric parallaxes. However, even the accuracy achievable with Hipparcos is not sufficient for the sample of runaway stars. Only seven stars have parallax errors below 50 per cent and the best case corresponds to an error  $> 30$  per cent. However, we could carry out a test of the spectroscopic method using the sample of early type stars from the Table 4 of Napiwotzki et al. (1993). Parameters were derived in a fashion similar to many investigations of runaway stars:  $T_{\text{eff}}$  was determined from Strömgen photometry and  $\log g$  from Balmer line fitting. All these stars have accurate Hipparcos

<sup>1</sup>The distance modulus is the difference between the apparent magnitude and the absolute magnitude.

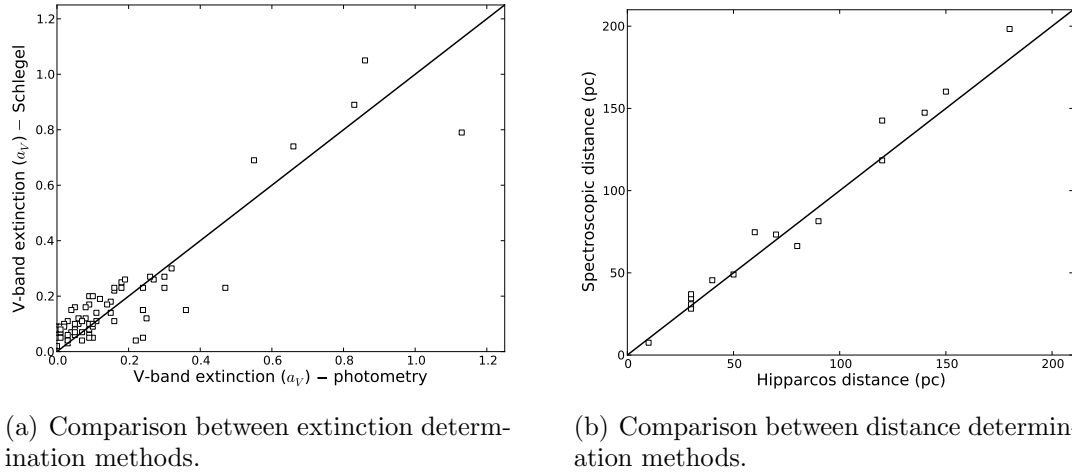


Figure 5.4: Comparison of extinction and distance determination methods. In (a), extinctions determined through Strömgren photometry are compared with extinctions obtained from the reddening maps of Schlegel et al. (1998), for our sample of runaway stars. In (b), distances computed using the spectroscopic method described here are compared with distances obtained from trigonometric parallaxes, for a sample of B stars from Napiwotzki et al. (1993).

parallaxes. We found that the ratio of distances determined using our method and the trigonometric parallax determination is on average 1.03, with a standard deviation of 0.11. This dispersion is of the same order of the expected error in distance corresponding to the best determinations of  $\log g$ , which is  $\sim 10$  per cent for an error of 0.1 dex. In Figure 5.4 a plot of the comparison between the two methods is shown. The linear relationship between the two quantities is easily visible.

Current positions in equatorial coordinates were obtained from the Hipparcos and the UCAC 2 catalogues, using the equinox 2000.0 transformation as given by SIMBAD<sup>2</sup>. Radial velocities were obtained from a variety of spectroscopic studies, as detailed in Table 5.1 and Table 5.2.

### 5.1.8 Proper motions

The sources used for the proper motions were: the UCAC 2 catalogue (Zacharias et al., 2004), the USNO-B catalogue (Monet et al., 2003), the Tycho-2 catalogue (Høg et al., 2000), the Hipparcos catalogue, the SuperCOSMOS science archive (Hambly et al., 2001), the NPM2 catalogue (Hanson et al., 2004) and the SPM catalogue, version 3.3 (Girard et al., 2004). The minimum number of proper motion sources for each star is 1, and the average is 3.6.

The different sources were compared to each other on a one-to-one basis, in the form of the plots seen in Figures 5.5, 5.6, 5.7, and 5.8, to assess their quality and consistency. In this investigation, the Hipparcos catalogue was taken as a reference, since it is believed that it consists of particularly good observations. It

<sup>2</sup><http://simbad.u-strasbg.fr/simbad/>

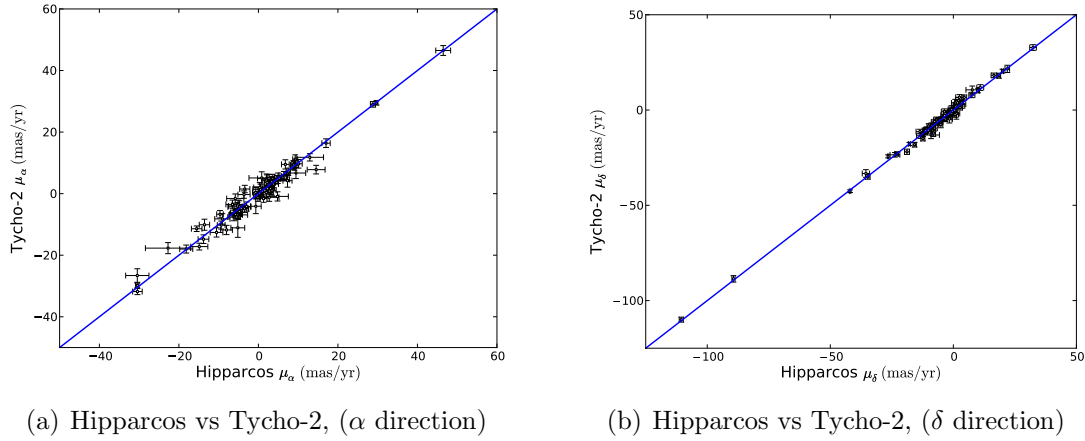


Figure 5.5: Plots comparing the proper motion estimates from Hipparcos and Tycho-2 catalogues. Note that the Tycho-2 catalogues uses the Hipparcos observations for one epoch. The  $\alpha$  component is multiplied by  $\cos(\delta)$ .

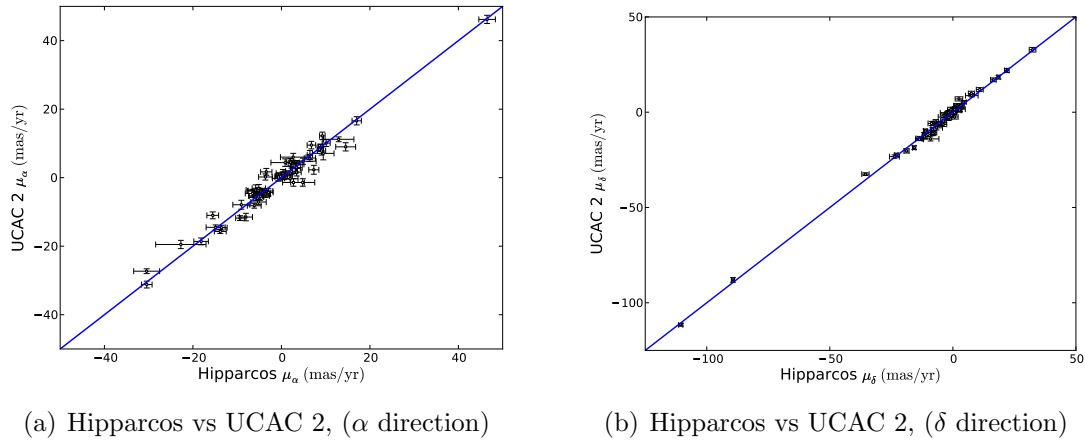


Figure 5.6: Plots comparing the proper motion estimates from Hipparcos and UCAC 2 catalogues. The  $\alpha$  component is multiplied by  $\cos(\delta)$ .

was observed that the UCAC 2, USNO-B, and the Tycho-2 catalogues had a particularly good correspondence with Hipparcos and between themselves. However, NPM2, SPM and Supercosmos deviate from the expected straight line, although they give consistent estimates within (huge) errors, with the exception of Supercosmos whose measurements deviated substantially from other sources. By looking at the actual images it was visible that for brighter stars the image tends to get saturated and makes it difficult to determine the centre of the stars. We found that a trend exists in the quality of Supercosmos proper motion estimates with visual magnitude. The correlation with the other catalogues becomes worse with increasing brightness, within the relevant interval here considered ( $5 \lesssim V \lesssim 15$ ). Taking this into consideration it was decided that the proper motion estimates for stars with visual magnitudes up to  $V = 14$  are good enough within (huge) errors (see Figure 5.9).

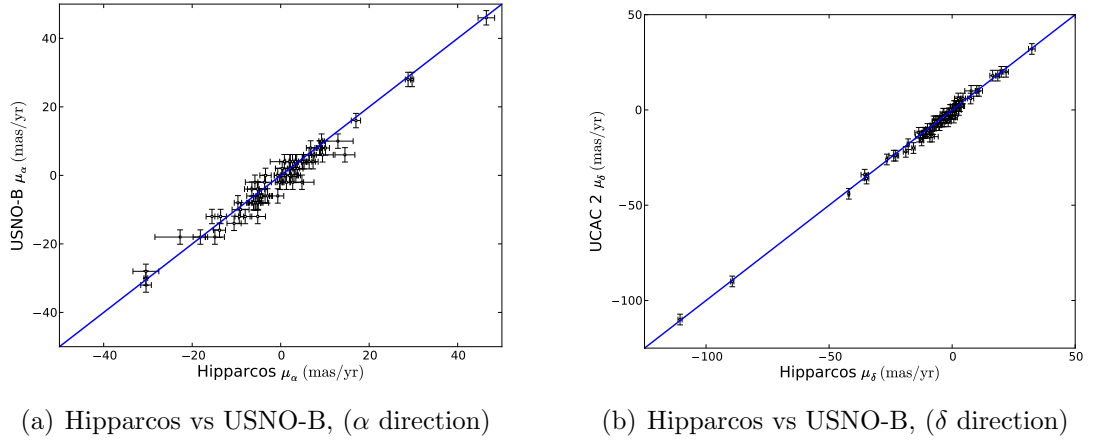


Figure 5.7: Plots comparing the proper motion estimates from Hipparcos and USNO-B catalogues. The  $\alpha$  component is multiplied by  $\cos(\delta)$ .

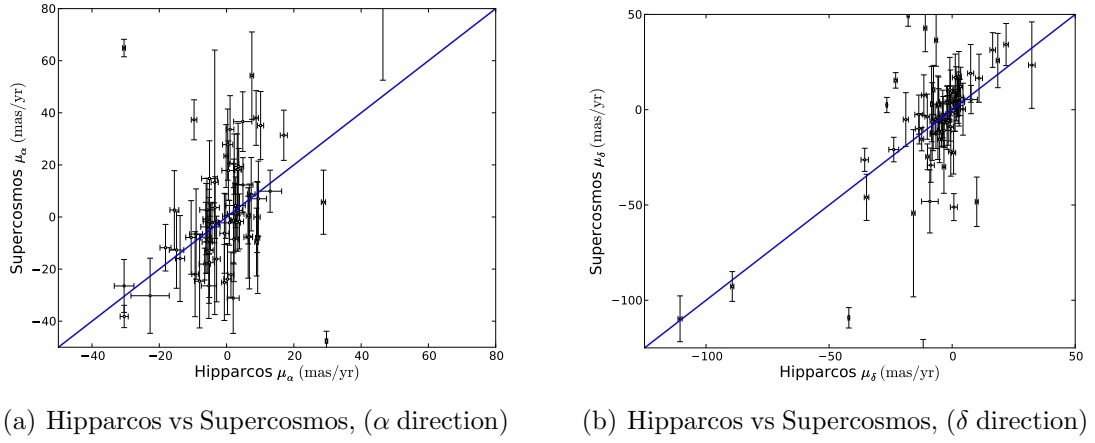


Figure 5.8: Plots comparing the proper motion estimates from Hipparcos and Supercosmos catalogues ( $V = 5, \dots, 11$ ). The  $\alpha$  component is multiplied by  $\cos(\delta)$ .

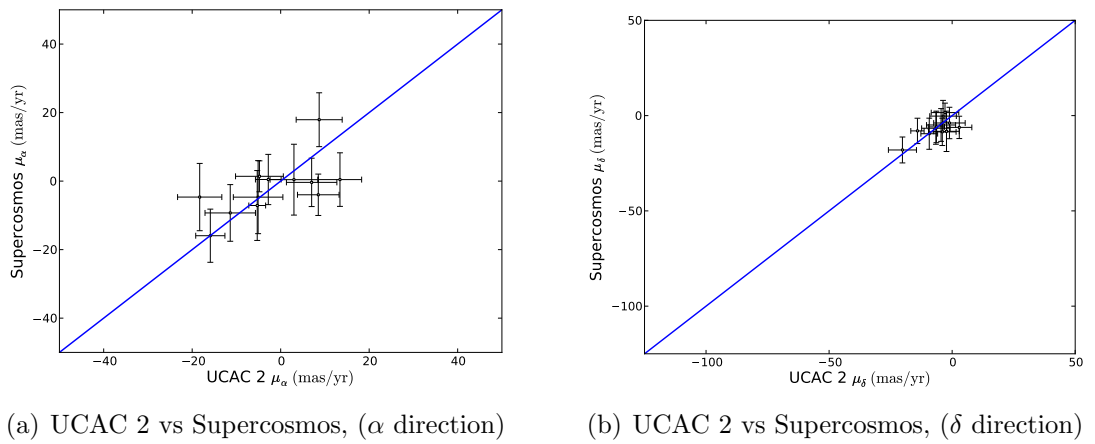


Figure 5.9: Plots comparing the proper motion estimates from UCAC 2 and Supercosmos catalogues, for stars fainter than  $V = 14$ . The  $\alpha$  component is multiplied by  $\cos(\delta)$ .

Then we needed to find an estimate for the measurement errors of the USNO-B and NPM2 catalogues, as these were unavailable for a great number of objects in the USNO-B case, and for all objects in the NPM2 case. The method used was to compute the distance to the estimates from other catalogues, weighting this distance with the measurement errors, and then finding the weights which gave a reduced  $\chi^2$  statistic closest to 1.

The next step was to compute a weighted average  $\langle \mu_x \rangle$ , where  $x$  corresponds to the  $\alpha$  or to the  $\delta$  direction, estimating each star's proper motion by combining all available observations. In this it was assumed all observations are independent, what we know is not entirely true, but should be a good enough approximation. If we denote the standard deviation of this weighted average by  $\sigma_{\mu_x}$  we have:

$$\langle \mu_x \rangle = \frac{\sum_{i=1}^n \mu_{x,i} / \sigma_{\mu_{x,i}}^2}{\sum_{i=1}^n 1 / \sigma_{\mu_{x,i}}^2} \quad (5.2)$$

and

$$\sigma_{\mu_x} = \frac{1}{\sqrt{\sum_{i=1}^n 1 / \sigma_{\mu_{x,i}}^2}}, \quad (5.3)$$

where  $\mu_{x,i}$  and  $\sigma_{\mu_{x,i}}$  are respectively the  $i^{\text{th}}$  proper motion measurement and its associated error, in the  $x$  direction, for a given star.

The final step was to apply a criterium capable of eliminating outliers. The expected deviation of a single observation from the true value is  $\sigma_{\mu_{x,i}}^2$ . Given the estimate of the true value,  $\langle \mu_x \rangle$ , the observed deviation is, for a single observation:

$$\Delta_{\mu_{x,i}}^2 = (\mu_{x,i} - \langle \mu_x \rangle)^2. \quad (5.4)$$

If the measurements are consistent with each other, then the quantity

$$\Delta_{\text{check}} = \frac{1}{n} \sum_{i=1}^n \Delta_{\mu_{x,i}}^2 / \sigma_{\mu_{x,i}}^2 \quad (5.5)$$

should be equal to 1. This corresponds to the situation where, in a statistical sense, the deviations of the measurements to the "true" value are equal to the expected value. The criterion was then to check when the quantity  $\Delta_{\text{check}} > 1$ , and in those cases to look at the individual measurements and eliminate the outliers. This was done with two caveats:

- in those situations where we only had two measurements nothing could be done because it is impossible to decide which one to eliminate;
- in some situations, where  $\Delta_{\text{check}}$  was greater than, but close to 1, it was impossible to select a single significant outlier, so sometimes the criterion was relaxed to reject values when  $\Delta_{\text{check}} \gtrsim 1.5$ .<sup>3</sup>

---

<sup>3</sup>Also, it should be noted that statistically the event  $\Delta_{\text{check}} \gtrsim 1$  should happen a few times.

### 5.1.9 Full space coordinates and velocities

The observed coordinates, proper motions and (heliocentric) radial velocities are based on the equatorial coordinate system. However, it is more convenient to work in a galactocentric frame of reference system in studies of the Galaxy. Thus, the observed coordinates and velocities were converted to a three-dimensional galactocentric Cartesian coordinates,  $(X, Y, Z)$ , this was a right-handed frame of reference where the  $X$  axis passes through the position of the Sun, pointing towards the Galactic Centre, and  $Z$  points to the North Galactic Pole. Furthermore, since this frame of reference is inertial, the velocities had to be corrected for the motions of the Local Standard of Rest (LSR) and that of the Sun relative to the LSR. The velocity of the LSR is simply given by the value of the velocity curve at the solar circle radius,  $v_{\text{LSR}} = v_c(8 \text{ kpc})$ . The adopted velocity of the Sun relative to the LSR was the one derived by Dehnen and Binney (1998) from the kinematics of a local Hipparcos sample, corresponding to the components  $(11.0, 5.3, 7.0)$  ( $\text{km s}^{-1}$ ). The velocities in the new frame of reference were thus given by:  $(V_x + 11.0, V_y + 5.3 + v_c(8 \text{ kpc}), V_z + 7.0)$  ( $\text{km s}^{-1}$ ). Note that, more recently, Schönrich et al. (2010) estimated the velocity of the Sun relative to the LSR to be  $\sim (11.1, 12.4, 7.25)$  ( $\text{km s}^{-1}$ ), about  $7 \text{ km s}^{-1}$  larger than the value we used for the azimuthal direction. However, this difference is too small to be important for our purposes.

Note that the velocity in the equatorial coordinate system is decomposed in two components: a component along the line of sight (given by the measured radial velocity) and the tangential component. The tangential component is further decomposed in two orthogonal directions: a direction parallel to the celestial equator (the proper motion  $\mu_\alpha$ ), and the perpendicular direction passing through the celestial poles (the proper motion  $\mu_\delta$ ). Thus the tangential component is given by:  $v_\theta = d\mu_\alpha + d\mu_\delta$ , where  $d$  is the distance to the star.

## 5.2 Orbital analysis

The method used to estimate the ejection velocities consists in tracing the orbits of the stars backwards in time until the first intersection with the Galactic plane. The present space velocity is obtained from the radial velocity and proper motion (given the distance), which are available for every star in our sample. Given the velocity and the position of the star, we integrated the orbit in the Galactic gravitational potential after inverting the velocity direction (to go back in time). This is essentially the method used to good effect by Hoogerwerf et al. (2001), and Ramspeck et al. (2001b), among others. The final output variables are then: the instant of intersection with the Galactic plane (which is equal to the time the star spent on the orbit after ejection, the *flight time*), the velocity at that instant (the *ejection velocity*), and the coordinates of the intersection of the orbit with the Galactic plane (the *birthplace*).

The orbits were computed using the program ORBIT6 developed by Oden-

kirchen and Brosche (1992). This program integrates the orbits of test particles in a modified version of the Allen and Santillan (1991) potential, where the disc has a scale-length of 3 kpc. The modifications made to the original Galactic potential are detailed in Section 4.2.3. The program takes as input the spatial coordinates and full space velocity (Section 5.1.9).

The error in the output variables is a complicated function of the errors in the observed input variables. However, it is important to have an estimate of the errors in the ejection velocities and flight times, especially because most previous studies did not perform an error analysis, with the notable exception of the studies by Martin (2006) and Ramspeck et al. (2001b). For this reason, the orbit determination procedure was implemented within a Monte Carlo scheme where the errors in the input variables were propagated along all the intermediate steps resulting in a *distribution* for each output variable, instead of a single value. The errors could then easily be computed from these distributions. Thus, the orbit of a given star was computed 10000 times in this Monte Carlo scheme, with each iteration consisting in the following steps (summarised in Figure 5.10):

1. the input variables were assumed to have Gaussian errors, thus in the beginning of each iteration a sample of the input variables was drawn randomly from the corresponding Gaussian distributions<sup>4</sup>;
2. ages and masses were obtained from the atmospheric parameters, as explained in Section 5.1.6;
3. distances were obtained from the atmospheric parameters, as explained in Section 5.1.7;
4. the input coordinates and velocities were converted to a galactocentric frame of reference (Section 5.1.9), using the distance computed in the previous step;
5. the orbits were integrated, given the positions and velocities computed in the previous step, using the ORBIT6 program with a time step of 0.2 Myr;
6. the velocity of the star when it reached the Galactic plane, after being corrected for the rotation of the Galactic disc (i.e. the velocity of the standard of rest at point of intersection), was taken as the ejection velocity;
7. the time since the beginning of the integration until the crossing of the plane was taken as flight time;
8. the point of intersection of the orbit with the Galactic disc was taken as the birthplace.

This procedure was implemented in a FORTRAN program. The orbit integration stopped, on any given iteration, when the orbit reached the Galactic plane (which

---

<sup>4</sup>Gaussian distribution with average given by the measured value and standard deviation given by the error.

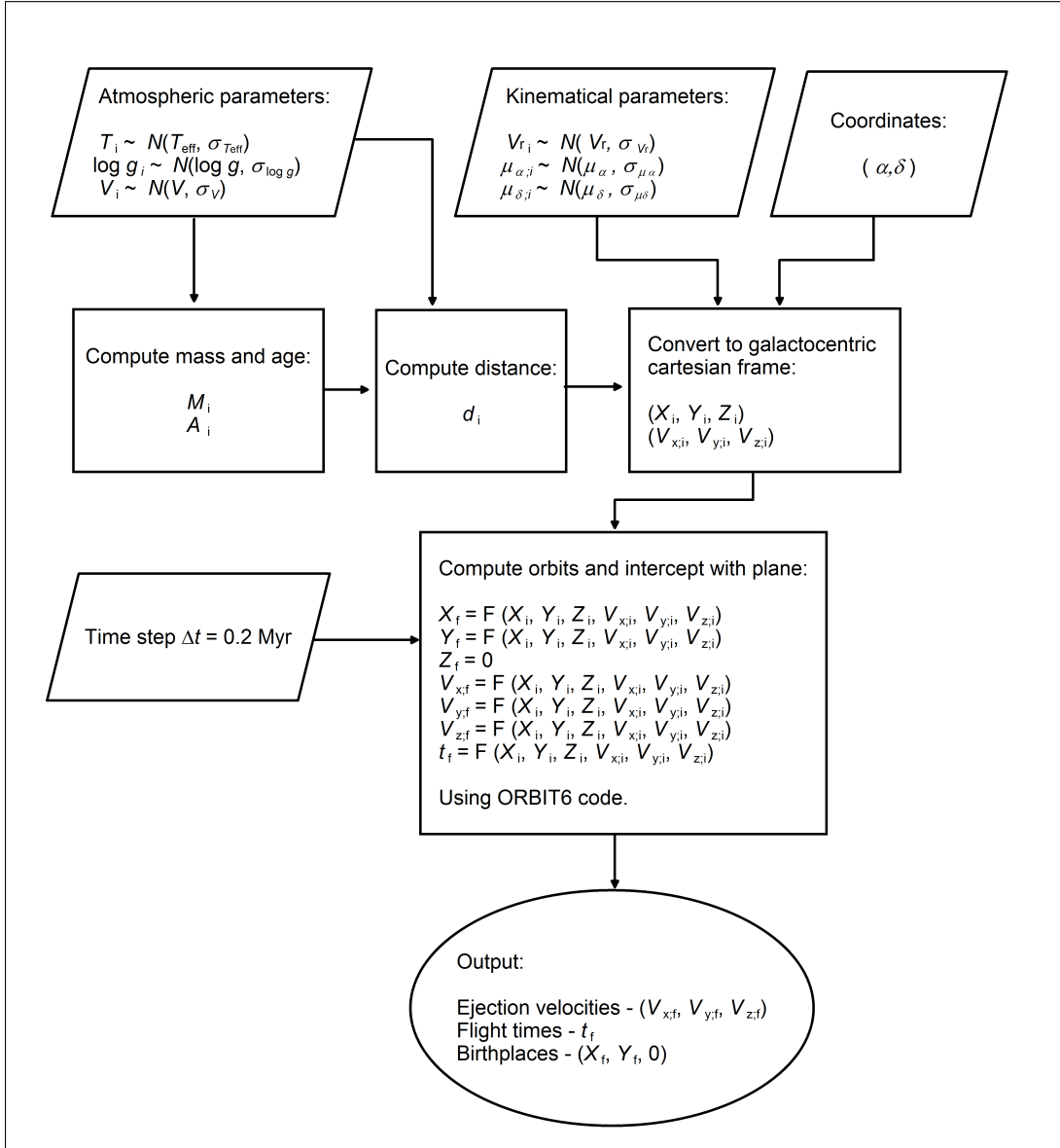


Figure 5.10: Flowchart summarising the method adopted to compute the ejection velocity, flight time and birthplace of a runaway star. The method was implemented within a Monte Carlo scheme where on each iteration the input variables would be randomly chosen from a Gaussian distribution with standard deviation given by the estimated observational error. The error in the output variables, resulting from the propagation of the initial errors, was then estimated from the final distribution. The flowchart represents one such iteration of the Monte Carlo scheme.

corresponds to  $Z = 0$  in the galactocentric Cartesian reference frame) or when the flight time exceeded 250 Myr (to avoid the program running forever in those situations where the simulated star did not reach the plane), whichever happened first. Instances with the star not reaching the Galactic plane within 250 Myr were not included in the calculation of velocities and flight times.

In the end, error in all output variables were estimated from their distributions. After some trials, it was realised that most of the time the distributions were highly asymmetrical, hence the errors were estimated in two different ways. The first estimate was the usual standard deviation, whereas the second estimate was based on the 16th and the 84th percentiles (thus emulating the standard deviation somehow). For the same reason, the mean is used as a measure of central tendency value in the first case, and the median in the second case.



# Chapter 6

## Properties of the population of runaway stars

### 6.1 Results

The final results of the analysis described in Section 5.2, applied to the 96 main sequence stars selected from the initial sample of 174, are the flight time (i.e. the time spent in the orbit since ejection until the present), the ejection velocity (i.e. the orbital velocity for  $Z = 0$ , relative to the star's standard of rest at the moment of ejection) and spatial  $(X_0, Y_0)$  coordinates of the ejection point, and their associated errors. In this Chapter we present the results and briefly discuss them. Tables with the computed values are shown in Appendix A.

#### 6.1.1 Flight times

If the disc ejection hypothesis is correct it follows that the computed flight times must be less than, or equal, to the corresponding evolutionary ages (cf. Section 5.1.6). The flight times of all stars in our sample are plotted in Figure 6.1. We consider them to be consistent within the errors if the flight time estimate minus its error, is equal to or lower than the evolutionary age estimate plus its error. We find that the flight times are consistent with the computed evolutionary ages to within the errors for 83 per cent of the sample and to within twice the errors for 97 per cent of the sample (corresponding to only three discrepant objects). Moreover, we note that for most stars  $T_f \simeq T_1$ , as it is expected from theory for both the BES and DES mechanisms. Portegies Zwart (2000) estimates, for the BES, that a late-type B star (mass in the interval 3–5  $M_\odot$ ) will spend more than 75 per cent of its lifetime as a runaway star, and Leonard and Duncan (1990) estimate, for the DES, a time for ejection from a cluster of the order of 10 million years, corresponding to more than 75–80 per cent of the lifetime spent as runaway, in the case of late-type B star. The fact that we find this agreement with theory suggests that the models are adequate or conversely, if we assume the models are correct, that the method used to compute the flight times does not have a fatal flaw. In particular, we are led to believe that the assumed Galactic potential (cf.

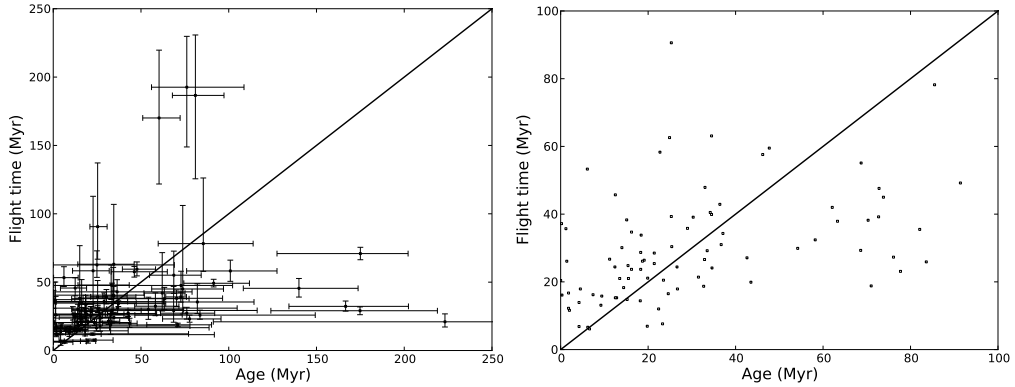


Figure 6.1: Flight time *versus* evolutionary ages with and without error bars, for easier visualization. Note that the *right* plot has a smaller scale, focusing on the “noisier” region up to 100 Myr.

Section 5.2 and Section 4.2.3) is realistic enough for our purposes. This conclusion is supported by the discussion on the sensitivity of the orbits to changes in the Galactic potential in Section 6.3.1.

In spite of this overall good agreement of observations and theoretical expectation, we find three stars in our sample for which the computed flight time is in serious disagreement (more than twice the errors in both directions) with our estimate of their evolutionary age (see Figure 6.2). Taken at face value this could indicate that these stars were born in the Galactic halo, a scenario proposed by Hambly et al. (1996) for the star PHL 346. If confirmed, this could have very important consequences for our understanding of star formation. However, first we have to consider other possible mechanisms and effects capable of extending the lifetime of main sequence B stars. These are:

**Rotation induced mixing:** early-type stars have generally high rotation velocities, in particular in the case of Be stars which rotate with velocities near the critical velocity. The centrifugal forces created by the fast rotation create extra mixing acting as an extra *overshoot* diffusing the elements produced in the core. This effect would increase the lifetime of a B star at most by 20–25 per cent (Maeder and Meynet, 2000).

**Lower than solar metallicity:** as mentioned in Section 5.1.6, ages were computed assuming a metallicity close to solar. A significant scatter of metallicities is observed for young stars in the disc. The metallicity distribution, as derived by Fuhrmann (2004) from a sample of main sequence stars from B to G spectral types within 25 pc of the Sun, has a standard deviation of 1.4 times the solar metallicity, which is comparable to the radial scatter in the thin disc (Cescutti et al., 2007). This effect is relevant because stars with lower metallicities stay longer on the main sequence, and the correspondent ZAMS (zero age main sequence) is bluer, implying longer lifetimes for given effective temperatures and surface gravities, when compared with stars with higher metallicity.

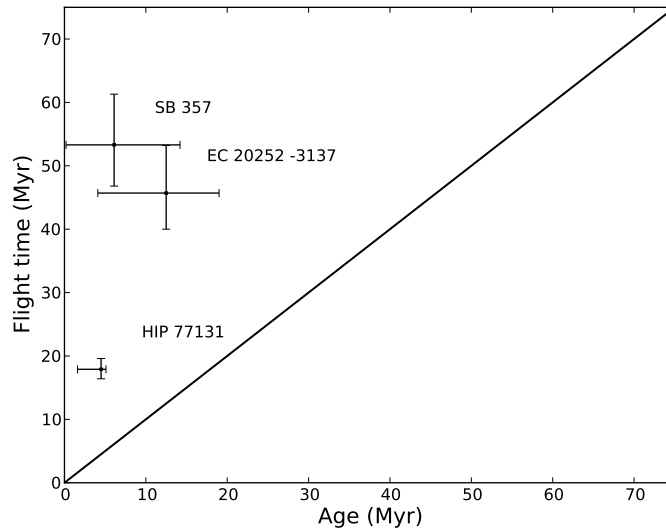


Figure 6.2: Flight time *versus* evolutionary ages including error bars. Only stars deviating more than twice the errors in both directions are plotted.

**Blue straggler:** the DEM may result in the ejection of a binary which could then merge after the ejection, creating a rejuvenated star analogous to the blue stragglers observed in clusters. This situation would be effectively the same as a star with a mass equal to the sum of the two stars in the progenitor binary being ejected from a position higher above the Galactic plane. Moreover, since the binary stars would have a spectral type later than B (to be able to produce a B star after the merger) this would increase dramatically the lifetime of the system. However, the ejection of intact binaries is predicted to be a rare event and the ejection velocities lower than about  $100 \text{ km s}^{-1}$  (Leonard and Duncan, 1990). More recently Perets (2009) has demonstrated that this mechanism could explain, in principle, the extreme youth of these distant stars, but the problem with the small numbers and velocities still remains.

The alternatives to these mechanisms would be a formation in the halo scenario, or errors in the analysis of the stars' atmospheres (which would propagate to the estimated distance) and/or errors in the measurement of proper motions. The three stars under consideration (Figure 6.2), that have flight times higher than the evolutionary ages within two times the errors, are: SB 357, EC 20252–3137 and HIP 77131. Although a few 2-sigma outliers are expected (about five in a sample of 100 objects), these stars have small errors, which makes it difficult to explain the discrepancies as statistical fluke. The estimated evolutionary ages for SB 357, EC 20252–3137 and HIP 77131 are  $6.1^{+8.1}_{-5.9}$  Myr,  $12.5^{+6.5}_{-8.4}$  Myr and  $4.5^{+0.6}_{-2.9}$  Myr, and the flight times  $53.3^{+8.0}_{-6.5}$  Myr,  $45.7^{+7.8}_{-5.7}$  Myr and  $17.9^{+1.7}_{-1.5}$  Myr respectively. We have computed the ages the stars would have if we take into account the maximum effects of metallicity and rotation. The results are summarized in Table 6.1. A more detailed discussion of each star follows:

Table 6.1: The flight times and evolutionary ages of SB 357, EC 20252–3137 and HIP 77131 if we assume a mass fraction of metals of  $Z = 0.008$ , and we take into account the effect of rotation. The first column gives the flight times, the second gives the ages adjusted for rotation, the third gives the ages for low metallicity, and the fourth gives the age for metallicity together with effect of rotation. All ages are given in Myr. The evolutionary ages for low metallicities were estimated from evolutionary tracks by Fagotto et al. (1994). We have assumed rotation increases the lifetimes by 25 per cent (cf. Maeder and Meynet, 2000).

Star	flight time	rotation	metallicity	metallicity and rotation
SB 357	$53.3^{+8.0}_{-6.5}$	$7.6^{+10.2}_{-7.3}$	$18^{+10}_{-12}$	$22.5^{+12.5}_{-15}$
EC 20252–3137	$45.7^{+7.8}_{-5.7}$	$15.6^{+8.2}_{-10.5}$	$22^{+4}_{-11}$	$27.5^{+5}_{-13.8}$
HIP 77131	$17.9^{+1.7}_{-1.5}$	$5.6^{+0.8}_{-3.6}$	$6^{+3}_{-1.5}$	$7.5^{+3.8}_{-1.9}$

**SB 357** This is a Be star, that is unlikely to be much evolved beyond the terminal age of the main sequence (Fabregat and Torrejón, 2000; McSwain and Gies, 2005). However a high value for the projected rotation velocity also means that no metal abundances were determined for this star, although the Helium abundance appears to be normal (Ramspeck et al., 2001b). The ages given in Table 6.1 are justified by the fact that this star is a fast rotator coupled with the fact that there is no evidence for Solar metallicity. However, even when both effects are combined, the difference between ages and flight times is still significant within (the equivalent to)  $1.5 \sigma$ . A different possibility is that the gravitational darkening may have been overestimated in this particular case. If the correction is ignored the computed flight time is  $65^{+11.9}_{-9}$  Myr, whereas the age is at most (assuming a low metallicity and adding the effect of rotation)  $46^{+7.8}_{-2.3}$  Myr, implying that even in this situation the difference is still significant within the error bounds. We note, however, that since SB 357 is a Be star this is a situation where the correction is the most important. As a final test, we compared the age estimate with the one obtained using the theoretical tracks by Bressan et al. (1993), but this increases the discrepancy even more since this new determination is a factor of 2 smaller than the original one. Nevertheless, it is also true that the estimate of the surface gravity, which relied on the fitting of the Balmer lines with synthetic ones derived from model atmospheres, are subject to systematic effects caused by the emission in the Balmer lines (Levenhagen and Leister, 2006). Thus, it is possible that the assumed atmospheric parameters may be inaccurate (note the discrepancy between the estimates by Conlon et al., 1992, and Ramspeck et al., 2001b), leading to an underestimation of the evolutionary age.

**EC 20252–3137** The classification of this star as being on the main sequence appears to be solid. It is rotating with a (projected) velocity of  $60 \text{ km s}^{-1}$  and has a normal abundance pattern, although there is some evidence for slightly supersolar metallicities (Magee et al., 2001). Given this evidence for high metallicity the as-

assumption of low metallicity is completely arbitrary. Moreover, the lack of evidence for a very high rotation velocity may mean that the increase in lifetime due to rotation may be much smaller than 25 per cent in this case, implying small effects from extra mixing in the stellar interior. Even if we ignore these considerations, the corrections just barely make the ages and flight times consistent within (the equivalent to)  $2\sigma$ . Since this star was not corrected for the gravitational darkening effect, given the small rotation velocity, it is possible that the difference between age and flight time has been overestimated. If the correction is applied then the flight time increases to  $46.2_{-5.6}^{+8.2}$  Myr and the age at most to  $22.5_{-10}^{+10}$  Myr (assuming a low metallicity and adding the effect of rotation). Once again, we also compared the age determination with the one obtained from the tracks by Bressan et al. (1993) but this determination (11.9 Myr) is very similar to the original one. We note again that the difference in this situation is still significant within the errors.

**HIP 77131** This star was classified as being on the main sequence based on the very high (projected) velocity of  $250 \text{ km s}^{-1}$ . The abundances of the elements N, C, and Si were measured by Martin (2004) and, although the abundances of nitrogen and carbon are consistent with a main sequence status, silicon appears to be overabundant. As in the case of EC 20252–3137, the assumption of low metallicity is not justified in this instance, but even if it were the flight time is still inconsistent with the evolutionary age as can be seen in Table 6.1. Since this star was not corrected for the gravitational darkening effect, as explained in Section 5.1.4, once again the difference between age and flight time may have been overestimated. The correction for HIP 77131 was done assuming, for the purpose of this analysis, 0.1 dex for the gravity and 3000 K for the effective temperature, based on a rough extrapolation (assuming a constant function) from the values corresponding to the highest temperature on the theoretical model (Frémat et al., 2005). The flight time obtained after the correction was  $17.9_{-1.5}^{+1.7}$  Myr, which is still inconsistent with the corrected age of  $6.3_{-2}^{+4}$  Myr (computed assuming low metallicity and adjusted for increased lifetime due to high rotation, after correction for the gravitational darkening effect), even within twice the error bounds. Again in this case we compared the original age estimate with the one obtained using the theoretical tracks by Bressan et al. (1993) but this determination (4.2 Myr) is very similar to the original one.

In summary, all three stars appear to be inconsistent with ejection from the disc even if we consider effects which would potentially explain an increase of their lifetime. In all cases new observations to confirm the atmospheric parameters are highly warranted, in particular in the case of HIP 77131 since it would be very important to have spectroscopic estimates. In that respect, the least intriguing case is probably the star SB 357, considering the difficulty in obtaining accurate atmospheric parameters because of the effect of emission in Balmer lines and the lack of metal lines caused by the high velocity rotation, since this is a Be star. This is in contrast to the other two stars (EC 20252–3137 and HIP 77131), which are therefore stronger candidates for stars formed in the halo. Note that the

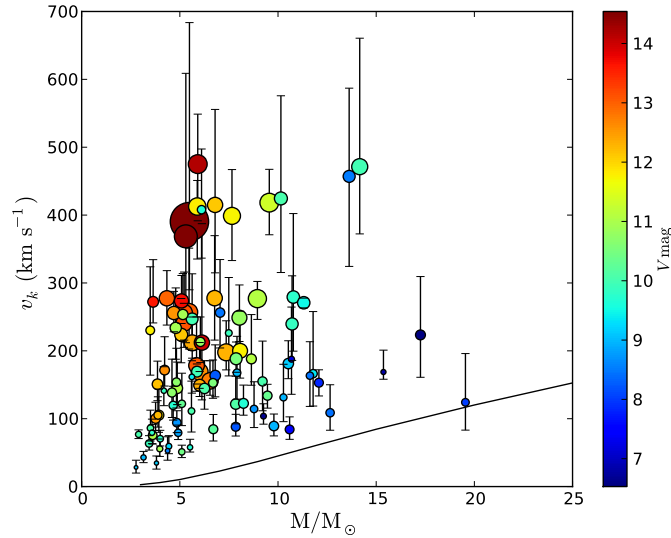


Figure 6.3: Ejection velocity – Mass distribution. The apparent visual magnitude is given by the grayscale, from black to white, black being the brightest and white the faintest. The size of the circles is proportional to the height above the Galactic plane. The line indicates the minimum velocity needed to reach a height of 1 kpc.

blue straggler scenario is not discussed because mass/luminosity ratios, rotation velocities, and chemical abundances of B type blue stragglers in open clusters are indistinguishable from “normal” stars (Schönberner and Napiwotzki, 1994; Andrievsky et al., 2000; Schönberner et al., 2001). However, as was mentioned before in this section, the ejection of an intact binary with a high ejection velocity should be an extremely rare occurrence. The estimated fraction of binaries among runaway stars is of  $\sim 1$  per cent (Perets, 2009 and references therein), which is a factor of three lower than implied by the observed fraction (3 in 96 stars), assuming all of them are merging on the required timescales.

### 6.1.2 Ejection velocities

Simulations for both ejection mechanisms (Leonard and Duncan, 1990; Portegies Zwart, 2000) predict a two dimensional mass-energy distribution. In particular, this distribution should show an inverse relation between mass and ejection velocity. It is known that runaway stars will usually be observed near the apex of their orbits, where the velocity is the lowest, (see Martin, 2006) – explaining why the distribution of measured (heliocentric) radial velocities in our sample has an average of only  $41 \text{ km s}^{-1}$ . Hence, stars with high ejection velocities will typically be further away than stars with lower ejection velocities. This fact introduces a potential bias in the detection of the highest ejection velocity stars, i.e. the stars which constitute the tail of the ejection velocity distribution, where the two ejection mechanisms are expected to differ.

The mass-ejection velocity distribution for our sample is shown in Figure 6.3, with the size of the symbols being proportional to the (vertical) distance to the disc

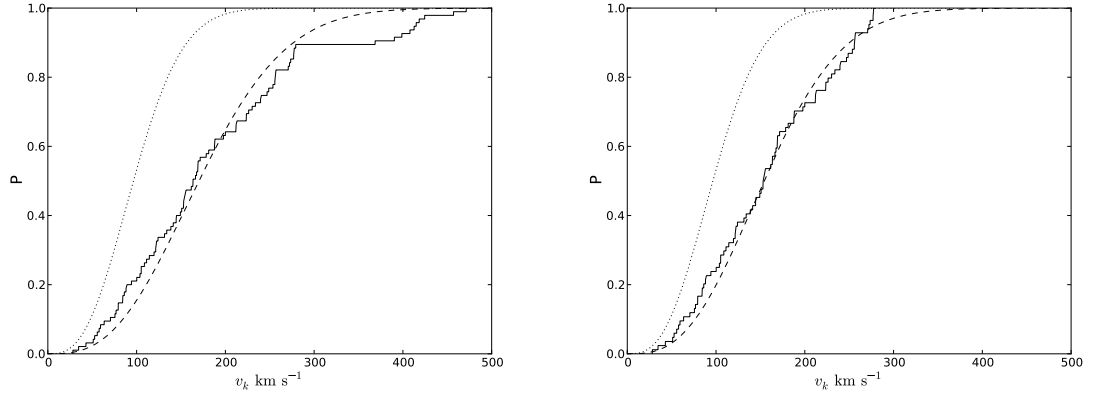
(larger symbols meaning higher distances), and the colour indicating the apparent visual magnitude. The minimum velocity needed for a star to reach a height of 1 kpc above the disc is shown as a solid line, explaining why no stars are found below said line. This is a result of the selection criteria which excluded nearby runaway stars. Nevertheless, the distribution appears to show a trend of decreasing ejection velocity for higher masses as predicted by theory (the trend is very weak and depends on the three more massive stars, including one of the problematic stars mentioned in Section 6.1.1, the most massive one). This is the reason why the sample is dominated by late type B stars, which is potentially problematic because it means that the stars that we need to observe are also fainter. We note that the surveys used as a source go as deep as  $V = 15$  (considering only runaway star candidates), however the faintest runaway observed has a magnitude of  $V \sim 14.5$ . We also note that the trend of increasing distance to the disc (and corresponding decrease in brightness) for higher ejection velocities appears to be true only up to about  $300 \text{ km s}^{-1}$ , with the maximum ejection velocity being about  $400 - 500 \text{ km s}^{-1}$ . The fact that we find a mix of bright and relatively faint stars, in a magnitude range of  $12 < V < 14.5$ , clustered around  $400 - 500 \text{ km s}^{-1}$  reflects a real drop in ejection velocity distribution. In fact, this is the highest ejection velocity predicted by Leonard and Duncan (1990), Gvaramadze et al. (2009), and Przybilla et al. (2008).

In Figure 6.4 we have plotted the cumulative distribution function (CDF) of the distribution function and the best Maxwellian fit which peaks at  $156 \text{ km s}^{-1}$ . It can be seen that the fit is good for velocities up to  $\simeq 300 \text{ km s}^{-1}$ , however there is a suggestion of bimodality which could indicate the existence of two different populations. If we assume that this group of high velocity runaway stars (velocities higher than  $350 \text{ km s}^{-1}$ , corresponding to 11 stars above this threshold and 85 below) corresponds to a different population and remove them from the distribution, then the fit to a Maxwellian distribution is much better, peaking at  $141 \text{ km s}^{-1}$ , as can be seen in Figure 6.4. Hence, the “slow” group appears to be consistent with the standard ejection scenarios. Moreover, since Leonard (1993) predicts a Maxwellian distribution peaking at  $50 - 100 \text{ km s}^{-1}$  for the ejection velocity, the observed distribution seems to indicate that we could not be missing many objects in the tail of the distribution, if we remember that we are missing many low velocity objects because we have selected only stars high above the Galactic plane.

Note that the selection of high Galactic latitudes may induce an overestimate of the number of high velocity stars, since the observed cone volume increases with distance. Although this effect may explain the strong high velocity tail observed, it does not explain the apparent bimodality. The significance and possible identity of the apparent high velocity population will be discussed later.

## 6.2 Birthplaces

Another relevant output of the orbit determination procedure is the point in Galactic plane from which a runaway star is ejected. These points of origin (com-



(a) Ejection velocity distribution of all runaway stars.

(b) Ejection velocity distribution of “slow” group of runaway stars.

Figure 6.4: Ejection velocity distribution. In (a), the solid line is the empirical cumulative distribution function, the dashed line is the best fit Maxwellian distribution (peaking at  $156 \text{ km s}^{-1}$ ), and the dotted line is the the predicted Maxwellian distribution (Leonard, 1993) (peaking at  $100 \text{ km s}^{-1}$ ). In (b), the solid line is the empirical cumulative distribution function corresponding to the sub-sample of stars with ejection velocities lower than  $350 \text{ km s}^{-1}$  (the “slow” group), the dashed line is the best fit Maxwellian distribution (peaking at  $141 \text{ km s}^{-1}$ ), and the dotted line is the the predicted Maxwellian distribution (same as in (a)).

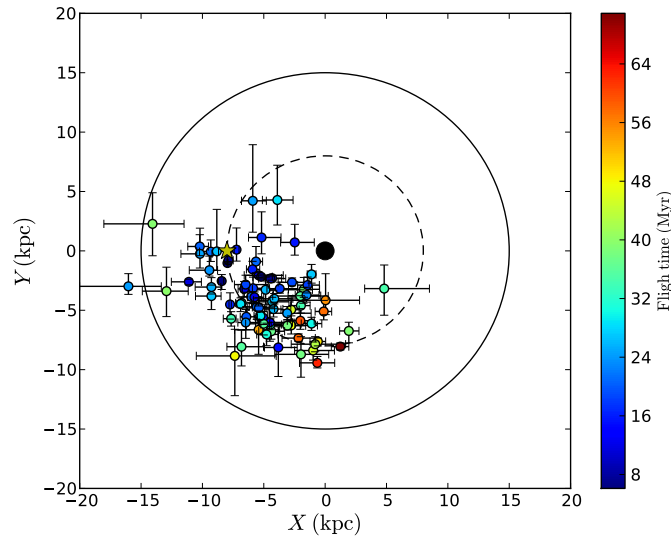


Figure 6.5: Birthplaces of our sample of runaway stars. The solid and dashed lines correspond to the 15 kpc and 8 kpc (distance of the Sun to the Galactic Centre) radii respectively. Only stars with error bars  $< 5 \text{ kpc}$  are shown.

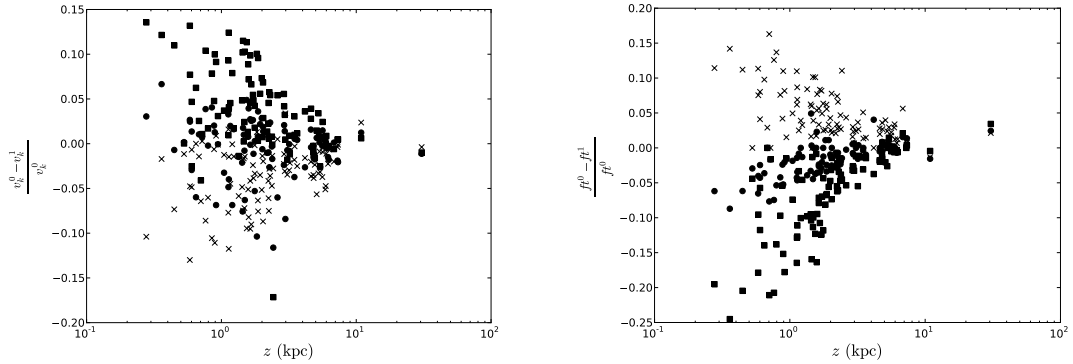
puted through the integration of orbits backwards in time) are what we call the stars' *birthplaces*. In Figure 6.5 the birthplaces of our sample of runaway stars are plotted, although restricted to stars with error bars smaller than 5 kpc, as is it not very relevant to show stars with very large errors (we are already assuming they were ejected from the disc of our Galaxy). The relevance of the birthplaces will be discussed later in connection to two problems: the link between hypervelocity stars and runaway stars, and the location and dynamics of the spiral arms.

## 6.3 Discussion

### 6.3.1 Influence of the gravitational potential

The model of the Galactic potential is an obvious source of uncertainty in the final results. A detailed analysis of the Galactic potential parameter space is outside the scope of our study. However we have tested a number of alternative models as an attempt to quantify the effect on the flight times and ejection velocities, by choosing different, reasonable, parameters, starting from the base model (cf. Section 4.2.3). We have tested three modified models: one with a disc scale-length shorter by 50 per cent, one with a disc scale-length longer by 50 per cent, and one with a total mass of the Galaxy higher by 30 per cent. In all cases the disc component mass, and the halo component mass and power law index were changed to fit the galaxy's circular rotation curve to the observed value of  $220 \text{ km s}^{-1}$  at the position of the Sun. This simplified procedure was used, instead of the more thorough employed in Section 4.2.3, because we were interested in testing the sensitivity of our results to extreme changes in the potential.

The plot of the relative difference of each model to the updated model, as a function of height above the Galactic plane, is shown in Fig. 6.6. It is noticeable that the difference between the models drops with distance to the disc, although it is not surprising that the influence of the disc component becomes less significant for large distances. Note in particular that the model with a heavier halo only affects the outcome because the choice of a heavier halo forces a much lighter disc in order to keep the local circular velocity unchanged. However, in the outer regions, where the disc component loses its influence, the results are almost unchanged which suggests that the mass of the halo is not crucial for the obtained results, as long as the local orbital velocity is kept at  $\simeq 220 \text{ km s}^{-1}$ . The fact that the results for the stars which are further away are mostly insensitive to the choice of potential is particularly important, since these are the stars that have the highest ejection velocities. The difference is more dramatic for the flight times which reach a difference of 25 per cent. Nevertheless, most cases in both the ejection velocities and flight times are contained in the interval 10–15 per cent in relative difference.



(a) Relative difference of the ejection velocities.

(b) Relative difference of the flight times.

Figure 6.6: Relative difference between the tested Galactic potential models. The circles represent the short scale length disc model, the crosses represent the long scale length disc model, and the squares represent the heavier halo model

### 6.3.2 Comparison with other studies

In this section we divide the literature overlapping with our work in four groups, noting that we are interested in comparing results regarding the kinematical analysis:

1. the papers dealing with the Palomar-Green sample, here abbreviated to PG papers (Rolleston et al., 1999; Lynn et al., 2004a);
2. the papers dealing with the Edinburgh-Cape sample, here abbreviated to EC papers (Rolleston et al., 1997; Magee et al., 2001; Lynn et al., 2004b);
3. the papers dealing with the Hipparcos sample (Allen and Kinman, 2004; Conlon et al., 1990; Martin, 2004, 2006);
4. the remaining papers (Conlon et al., 1992; Ramspeck et al., 2001b; Behr, 2003a).

The studies focused on the Hipparcos sample are by themselves unsuitable to study the ejection velocity distribution, given that we are interested in the tail of the aforementioned distribution, where the difference between the BEM and DEM should be more evident. The Hipparcos brightness limit (see Table 6.2) is crippling if we want to have an estimate of the ejection velocity for the more distant, therefore potentially faster, objects. This means that although proper motions are used in the kinematical analysis performed by Allen and Kinman (2004) and Martin (2006), these studies do not give a full picture regarding the nature of the ejection velocity distribution.

On the other hand, the studies dealing with the EC and PG surveys suffer from the fact that they explore only a narrow range of brightnesses (see Table 6.2) and proper motion information was not used for the kinematical analysis of the studied objects. In the EC series of papers, the kinematical analysis is incomplete

Table 6.2: Limiting magnitudes and completeness estimates. The completeness estimates have a dependency on Galactic latitude and spectral type.

Survey	limiting magnitudes	completeness range
Hipparcos	$V \sim 12.4$	$7.3 \lesssim V \lesssim 9$
Edinburgh-Cape (EC)	$V = 15$	$11 \lesssim V \lesssim 15^*$
Palomar-Green (PG)	$11 \lesssim V \lesssim 14.5$	$13 \leq B_{\text{PG}} \leq 14.6^{**}$

\* – for the spectral type interval B0 – B5 (Lynn et al., 2004b)

\*\* – Photographic magnitudes  $B_{\text{PG}}$  given for PG survey

in the sense that proper motion data was not available for the stars EC 20011–5005 and EC 20105–2944. Similarly in the PG series of papers, the kinematical analysis lacked proper motion data for five stars (40 per cent). The other studies are not systematic, consisting of observations of only a small number of objects. The stars from the studies by Behr (2003a) and Conlon et al. (1992) cover a range in magnitude that is barely higher than the limiting magnitude from the Hipparcos sample and they do not include proper motion data in the kinematical analysis. On the other hand, the sample studied by Ramspeck et al. (2001b) covers the range  $10 \lesssim V \lesssim 14$  in brightness and does include proper motion data in the kinematical analysis performed for all but four stars: PHL 159, PG 1511+467, SB 357, and HS 1914+7139. The star SB 357 is also analysed by Conlon et al. (1992).

By combining these samples we were able to better constrain the ejection velocity distribution, because we cover the near objects (Hipparcos sample) and distant objects (the other samples), corresponding to a range in distance of 0.57 – 35 kpc. The fact that our kinematical analysis includes proper motion data for all stars also constitutes an improvement over previous analysis, because it has permitted us to compute the orbits with all information necessary (position and velocity). In relation to the Hipparcos sample nothing new has emerged from our study, which is not surprising given the fact that the proper motion data from Hipparcos was already included in the previous investigations. On the other hand, we have new results on stars from the other samples. All the stars mentioned earlier in this section lacking proper motion data on previous studies have now more precise estimates of the flight times and ejection velocities. The comparison of the flight times with the estimated evolutionary ages confirms that most stars are consistent with the runaway hypothesis, whereas the computed ejection velocities suggest a limit of 400 – 500 km s<sup>-1</sup> for the ejection. This is consistent with the theoretical predictions of Leonard and Duncan (1990) and Gvaramadze et al. (2009). The stars SB 357 and HS 1914+7139 were estimated to have flight times larger than their evolutionary ages by Conlon et al. (1992) and Ramspeck et al. (2001b), in the case of SB 357, and by Ramspeck et al. (2001b) in the case of HS 1914+7139. The inclusion of proper motion data in the kinematical analysis permits us to confirm that SB 357 appears to be incompatible with ejection from the disc, whereas

HS 1914+7139 now appears to have a flight time compatible with an ejection from the disc scenario. It is important to mention that the star HS 1914+7139 was also studied by Heber et al. (1995) who confirmed a flight time much higher than the estimated age, based on an analysis lacking proper motion data. Similarly, the star BD -2 3766, analysed by Conlon et al. (1992), who found a flight time higher than the estimated age of the star, appears to be compatible with ejection from the disc after the inclusion of proper motion data in the analysis.

### 6.3.3 The link with hypervelocity stars

Hypervelocity stars are stars traveling on unbound orbits, generally believed to be ejected by the Supermassive Black Hole in the centre of the Milky Way (Brown et al., 2007b), the so-called Hills mechanism (Hills, 1988). The apparent maximum ejection velocity in our sample is very close to the escape velocity in the solar neighbourhood ( $555.3 \text{ km s}^{-1}$  for the adopted gravitational potential). This means that the group of stars with the highest ejection velocities (the high velocity group discussed on Section 6.1.2, hereafter abbreviated to high velocity group) are near the regime of hypervelocity stars. Note that, depending on the direction of ejection, some of them could – in principle – exceed the escape velocity. It is however unclear if they constitute a low velocity tail of the hypervelocity population, or if they are simply extreme cases of runaway stars. It could also be the case that the distinction between hypervelocity and runaway stars is artificial and they all should be considered part of the same population, the former being just an extreme case of the latter.

There are at least two cases of hypervelocity stars which were shown to have been ejected far from the Galactic Centre. These are HD 271791 (Heber et al., 2008; Przybilla et al., 2008) and HIP 60350 (Irrgang et al., 2010), having ejection velocities of  $\simeq 400 \text{ km s}^{-1}$  and  $379 \text{ km s}^{-1}$ , respectively. These velocities correspond to the observed limit in our study, as discussed in Section 6.1.2, which makes the case for the existence of a real limit even stronger. Interestingly, from the stars in our sample with ejection velocities greater than  $350 \text{ km s}^{-1}$ , only two have points of origin in the disc compatible with, although not necessarily coinciding with, the centre of the galaxy, HIP 105912 and EC 19596–5356. A Galactic Centre origin can be ruled out for the other nine cases. Our results, combined with the results for HD 271791 and HIP 60350, imply that the high velocity group of runaway stars could not, in its entirety, have been ejected by the Hills mechanism.

Both the DEM and the BEM scenarios are able to produce stars with the required velocities of  $\simeq 400 \text{ km s}^{-1}$ . The mechanism proposed by Gvaramadze et al. (2009), which is a variation of the classical DEM where the dynamical interaction is between a binary and a very massive star (mass greater than  $50 M_{\odot}$ ) instead of another binary, can also produce both runaway and hypervelocity stars. In fact it is argued by Gvaramadze (2009) that the star HD 271791 achieved its high velocity due to the DEM. However, the predicted velocity distribution is continuous in DEM models, with no existence of a natural velocity limit (with the exception

of the  $1400 \text{ km s}^{-1}$  limit established by Leonard, 1991). These predictions are at odds with the observed distribution, where both a limit velocity and a gap in the distribution are apparent. A variation of the classical BEM as described by Przybilla et al. (2008) has been proposed to explain the ejection of both HD 271791 and HIP 60350. In this case a very close binary, composed of a massive star (mass  $> 40 M_{\odot}$ ) and a B type main sequence, undergoes a common envelope phase until the primary loses the envelope due to the deposition of the spiraling secondary's orbital energy, stopping the merger. The system will then be composed of a Wolf-Rayet star and a B type main sequence, with a very small separation between the two components, which can be as small as  $13 - 15 R_{\odot}$ . When the Wolf-Rayet ends as a supernova, the B type companion is released with a velocity close to its orbital velocity. This scenario establishes then a natural limit for the ejection velocity of around  $400 \text{ km s}^{-1}$ , close to the observed limit. Moreover, the small separation achieved during the common envelope phase, coupled with the fact that a Wolf-Rayet star is more compact than a main sequence star with the same mass, would explain the observed gap in the ejection velocity distribution. This follows because two different populations would correspond to different types of binaries: a binary with a very massive Wolf-Rayet star, evolving into a common envelope phase, as previously described, or the more traditional scenario (e.g. Portegies Zwart, 2000) where the binary evolves either as a detached or semi-detached binary. Note that the shorter separation in the latter case implies higher ejection velocities.

On the other hand, it could be argued that the traditional mechanisms can only accelerate stars up to velocities of about  $200 \text{ km s}^{-1}$  as has been traditionally believed (see for example Hoogerwerf et al., 2001; Gvaramadze et al., 2009), what would mean that the stars with high ejection velocities in our sample were ejected by a different mechanism. This mechanism would be a third mechanism responsible for the ejection of hypervelocity stars far from the Galactic Centre, with the stars with high ejection velocities corresponding to the low velocity tail of the ejection velocity distribution produced by this mechanism. A candidate would be for example the mechanism proposed by Gualandris and Portegies Zwart (2007), which consists in a dynamical encounter between a binary containing the ejected star and an intermediate-mass black hole in the centre of dense cluster. The fact that a gap in the ejection velocity distribution is observed suggests that they may correspond to two different populations, however only a better understanding of all selection effects would permit to draw a firm conclusion. This hypothesis suffers from the fact that direct evidence of the existence of intermediate-mass black holes is still lacking.

In summary, everything considered, the evidence suggests that there is no reason to separate runaway and hypervelocity stars in two separate populations. All mechanisms have to be considered together to understand the whole picture, including the BEM, the DEM, the Hills mechanism, and possibly the intermediate-mass black hole interaction mechanism. The most extreme ejection velocities are better explained by the Hills mechanism when they occur in the Galactic Centre, and by the BEM when ejection occurs far from the Galactic Centre.



# Chapter 7

## Tracing the spiral arms

### 7.1 Introduction

If we assume that most stars are born in the spiral arms, then the birthplaces of the runaway stars would indicate the position of the spiral arms at the time of their ejection, roughly corresponding to the stars' ages. In other words, by tracing back in time the orbits of these stars we are essentially computing the position of the spiral arms at the time of the stars' birth. However, this conclusion is strictly true only when the flight times are equal to the evolutionary ages, as the stars start drifting away from the spiral arms as soon as they are born. Nevertheless, in the case of runaway stars the difference is not very significant (cf. Figure 6.2).

Some structure is apparently visible in the distribution of runaway stars' birthplaces (Figure 6.5). In particular, just outside the solar circle (8 kpc radius) there appears to be a curve extending roughly from  $X \simeq 8$  kpc to  $Y \simeq 10$  kpc, and maybe one or two other such structures inside the solar circle. Although we know that the birthplaces do not correspond to the present position of the spiral arms, it motivates the use of runaway stars as tracers of the spiral arms.

The method to trace the spiral arms would consist then in using the technique developed in Chapter 5. The use of high Galactic latitude runaway stars as tracers of the spiral arms has two advantages over more traditional methods:

1. Since high Galactic latitude stars are not obscured by dust, they are potentially observable up to very large distances even beyond the Galactic Centre. Furthermore, they move at high speeds from their birthplaces. These two facts combined imply that this method permits, in principle, to cover most of the disc, including the most distant arms.
2. Time dependence is inherent to the method. Thus, it is possible to determine the position of the arms at different time instants which allows, in principle, the determination of the pattern speed (Section 2.2).

However, our sample of high Galactic latitude runaway stars is not the most appropriate for this task, due to its limitations. As can be seen in Figure 6.5 the

errors are quite large, caused by the uncertainties in the input parameters: the proper motions and distances in particular. Our aim is to show that this method is feasible and can be applied in the future to a larger sample of runaway stars with better quality measurements of all relevant parameters (distances, proper motions, radial velocities) as will become available from the astrometric Gaia satellite mission (Lindegren, 2010 and references therein). A way to test the feasibility of the method is to select a large sample of stars with accurate measurements of the relevant quantities, in particular distances and proper motions. For this reason, a second sample was selected as is explained below.

## 7.2 The Hipparcos sample

Our hypothesis is that it is possible to use observations of runaway stars to identify the position of the spiral arms at different moments in time. In order to test this idea we have selected a second sample composed of nearby early-type stars and applied the same the technique to identify the places of birth. The advantages of testing the method with this sample are two-fold: bright nearby stars have much better quality kinematical data (proper motions and parallaxes from Hipparcos) than our sample of runaway stars, and it is immediate to confirm their evolutionary status<sup>1</sup>. This sample was then used to determine the pattern velocity – assuming a given position of the spiral arms in the present – and then the results were compared with the ones obtained for our sample of runaway stars. Further references to an “Hipparcos sample” will be referring to this new sample.

### 7.2.1 Sample selection

Since we were interested in good quality kinematical data, the sample was drawn primarily from the Hipparcos catalogue (new reduction by van Leeuwen, 2007). However we needed to supplement data derived from spectroscopic analyses for two reasons: radial velocity estimates are needed to obtain the total spatial velocity and to detect possible spectroscopic binaries<sup>2</sup>. The steps that were undertaken were then the following:

1. We cross-matched the Hipparcos catalogue with the Bright Star catalogue (Hoffleit and Jaschek, 1991). The cross-matching was performed with the software TOPCAT, using the routine SKY with a maximum error of 12 arcsec. The number of stars appearing in both catalogues is 9063.
2. From the this initial number of 9063 we removed all stars identified as spectroscopic binaries in the Bright Star catalogue, and all stars that appeared

<sup>1</sup>Since the distance is determined by a geometrical method (parallax) independent of any assumptions on the nature of the stars it is possible to compute the luminosity, constraining the position in the H-R diagram (because the colours are also known).

<sup>2</sup>Spectroscopic binaries are not suitable for our purposes since they will have brightness and colours corresponding to a mixture of the stars in the system.

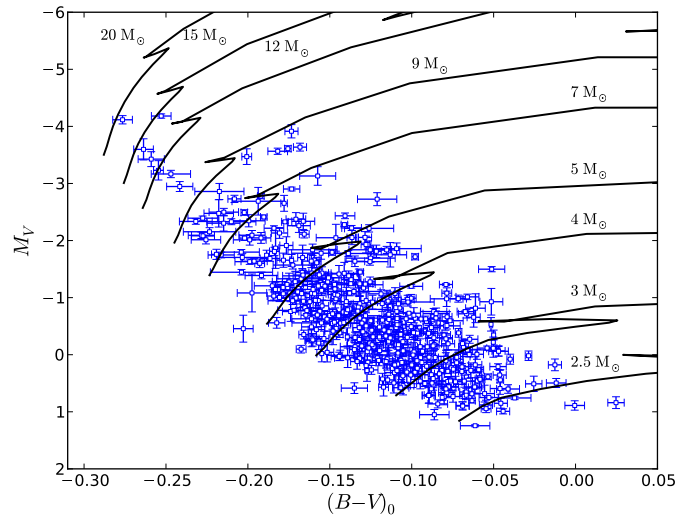


Figure 7.1: Colour-magnitude diagram of the local Hipparcos sample. Magnitudes are absolute magnitudes in the Johnson  $V$ -filter and colours are dereddened  $B - V$ . The theoretical tracks (Schaller et al., 1992) used to estimate the ages are shown as black solid lines.

as a single star in the Bright Star catalogue but that actually corresponded to two or three different stars in the Hipparcos catalogue, reducing the size of the sample to 8505.

3. Then we applied two criteria (cuts in parallax-colour space) in order to reduce our sample to stars with spectral type B or earlier. The Bright Star catalogue is complete only down to brightness  $V = 6.5$ . Note that this brightness corresponds to a distance of 200 pc for a star with an absolute magnitude  $M_V = 0$ . Hence we limited our sample to stars with distances equal or lower than this, corresponding to a minimum parallax of 5 mas. The limiting colour was decided in such way that we would include only stars hotter than 9500 K, as our focus is only stars with spectral type earlier than A0. Using Equation (7.3) (see next Section) we can see that this temperature corresponds to  $(B - V) = 0.05$ , so this was the limiting colour. From the previous number of 8505 stars, we found 556 fitting our criteria (minimum parallax and maximum  $(B - V)$  colour).
4. Using the spectral type information from the Bright Star catalogue we further removed stars which were identified as having spectral types later than B. In many instances, these were stars with peculiar abundance patterns. This step reduced the sample of 556 stars to 516.
5. Later, at the analysis stage (cf. Section 7.2.2), we discarded stars with large measurement errors, i.e. the stars with absolute errors in parallaxes and  $(B - V)$  colours greater than 1 mas and 0.02 respectively. Consequently, the final sample had 470 stars.

The data for each of the 470 stars consisted in: proper motions, parallax (hence distance),  $V$  magnitudes,  $(B - V)$  colours and coordinates from the Hipparcos

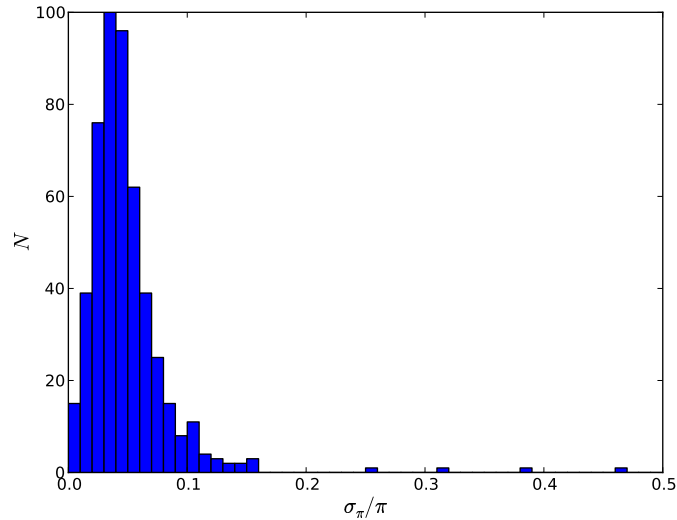


Figure 7.2: Distribution of the relative error in parallax measurements of our local Hipparcos sample.

catalogue, and radial velocities from the Bright Star catalogue.

### 7.2.2 Lutz-Kelker bias

Samples selected by a lower limit in parallax are subject to a bias, introduced by the random measurement errors, that causes, on average, parallaxes to be overestimated.

To understand the bias, imagine a star with a parallax close to the lower limit, and with a Gaussian measurement error. Sometimes this situation will correspond to a true parallax (the quantity we wish to estimate) greater than the limit, and sometimes it will correspond to a true parallax lower than the lower limit. But, since there are more stars outside the limit than inside the limit, there will more stars with true parallaxes lower than the lower limit entering the sample than stars with true parallaxes higher than the lower limit leaving the sample. The result is an average of the observed parallaxes higher than the the average of true parallaxes (Lutz and Kelker, 1973). The Lutz-Kelker bias is, in sense, dual to the Malmquist bias present in magnitude limited samples (Smith, 1987), so that parallax limited (sometimes called “volume limited”) samples suffer from the former, whereas magnitude limited samples suffer from the latter.

The first formal study of this bias was done by Lutz and Kelker (1973), who derived a numerical correction to the absolute magnitudes of a parallax-limited sample. This correction depends only on the relative measurement error of the parallax,  $\sigma_\pi/\pi$ .

In principle, parallax-limited samples should be corrected for this bias, so we investigated the effect it would have in our sample. In Figure 7.2 we have a plot of the relative measurement error of the parallax. As can be seen, most of our sample

(more than 98 per cent) has  $\sigma_\pi/\pi < 0.1$ , and about 88 per cent of the sample has  $\sigma_\pi/\pi < 0.075$ . According to Table 1 of Lutz and Kelker (1973), the correction for  $\sigma_\pi/\pi < 0.1$  amounts to  $-0.11$  mag, and the correction for  $\sigma_\pi/\pi < 0.075$  amounts to  $-0.06$  mag. Considering that a correction of  $-0.05$  in absolute magnitude translates, in the case of a typical B star, to about 2 per cent difference in distance, and that most stars in our sample have corrections that are a fraction of that, we concluded that the bias has a negligible effect only.

Furthermore, note that the four stars with large relative errors (cf. Figure 7.2) were discarded from the sample.

### 7.2.3 Bolometric and reddening corrections

Given the parallax and the apparent magnitude in  $V$  band it is straightforward to compute the absolute magnitude  $M_V$ , from the distance modulus, as in the case of the runaway stars sample. Thus, we can represent this sample in a Colour-Magnitude Diagram (CMD), as can be seen in Figure 7.1. Also represented in the same figure are the theoretical evolutionary tracks by Schaller et al. (1992) that we used to estimate the ages of these stars (the same method used with the runaway stars sample). However, the theoretical tracks were computed for the *bolometric* (integrated over all wavelengths) luminosity and effective temperatures, so they could be represented in an H-R diagram as this is what is natural from the theoretical point of view. Yet, the observational data consists of the brightness and colour of the stars. For this reason it was necessary to convert the theoretical tracks from the  $L - T_{\text{eff}}$  plane into the  $M_V - (B - V)$  plane.

The difference between a star's bolometric magnitude  $m_{\text{bol}}$  and its visual magnitude  $V$  is the *bolometric correction*  $BC$ :

$$BC = m_{\text{bol}} - V = M_{\text{bol}} - M_V. \quad (7.1)$$

So, in order to find a star's visual absolute magnitude, given the bolometric magnitude, is a matter of obtaining the bolometric correction, since the bolometric magnitude is easily obtained<sup>3</sup> from the luminosity (which is the quantity given by the models):

$$M_{\text{bol}} = M_{\odot, \text{bol}} - 2.5 \log \left( \frac{L_{\text{bol}}}{L_{\odot, \text{bol}}} \right). \quad (7.2)$$

The bolometric correction for the theoretical evolutionary tracks were obtained from a polynomial fit to the tables in Flower (1996), corresponding to a sample of 40 main sequence stars (see Table 7.1). The bolometric corrections are a function of the spectral class and are usually computed (together with the effective temperature) by fitting stellar atmosphere models to the observed line profiles (see for example Napiwotzki et al., 1993). A relation between  $(B - V)$  and the effective

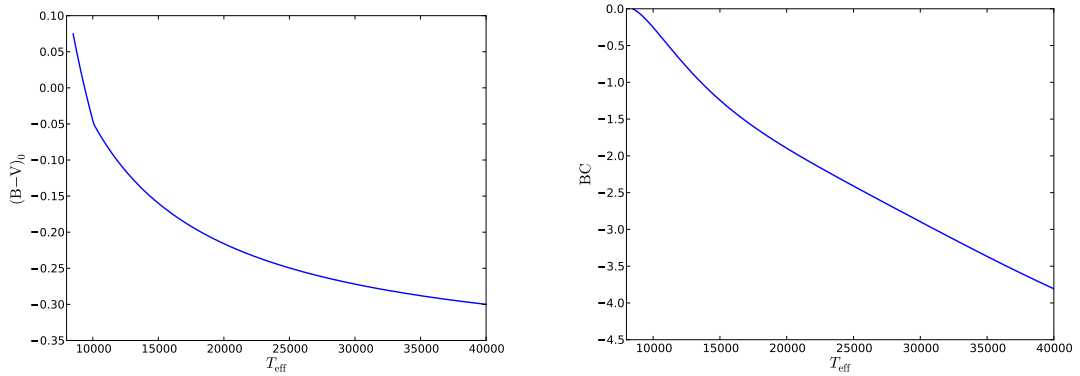
---

<sup>3</sup>We assumed the value of  $M_{\odot, \text{bol}} = 4.74$  for the (bolometric) absolute magnitude of the Sun (Cox, 2000).

Table 7.1: Bolometric corrections according to a polynomial fit to the data in Flower (1996), valid for main sequence stars.

Coefficient	$\log T_{\text{eff}} \geq 3.9$	$3.9 > \log T_{\text{eff}} > 3.7$	$\log T_{\text{eff}} \leq 3.7$
a	$-1.17611442 \times 10^5$	-26038.12007144	-18668.89327387
b	$1.36563653 \times 10^5$	26908.35552847	15191.74918606
c	$-6.33545248 \times 10^4$	-10436.91452813	-4122.5782362
d	$1.46792875 \times 10^4$	1800.73885191	373.07226005
e	$-1.69872981 \times 10^3$	-116.6098363	—
f	78.5443408	—	—

$$BC = a + b \log T_{\text{eff}} + c(\log T_{\text{eff}})^2 + \dots$$



(a)  $(B-V)_0$  colours as a function of effective temperature.

(b) Bolometric correction as a function of effective temperature.

Figure 7.3:  $(B-V)_0$  colours and Bolometric correction as a function of effective temperature.

temperature  $T_{\text{eff}}$  can also be found in Flower (1996), however we have preferred to use the relation from Napiwotzki et al. (1993) instead as its mathematical expression is much simpler:

$$(B-V)_0 = \begin{cases} 0.667\Theta - 0.384 & \text{for } \Theta < 0.5 \\ 1.347\Theta - 0.724 & \text{for } 0.5 < \Theta < 0.6, \\ 1.997\Theta - 1.114 & \text{for } \Theta > 0.6 \end{cases} \quad (7.3)$$

where

$$\Theta = \frac{5040 \text{ K}}{T_{\text{eff}}}. \quad (7.4)$$

Although it appears inconsistent to use the equation from Flower (1996) for the bolometric correction and the equation from Napiwotzki et al. (1993) for the colours  $(B-V)$ , a comparison between the two  $(B-V) - T_{\text{eff}}$  relations reveals they are very similar. The bolometric correction and  $(B-V)$  are shown in Figure 7.3 as a function of  $T_{\text{eff}}$ .

Since it is common for OB stars to be found within dusty star-forming regions,

it is especially important to correct their  $(B - V)$  colours for reddening caused by interstellar absorption. Hence, the  $(B - V)$  colours of these stars were corrected using a procedure based on Strömgren  $uvby\beta$  photometry, as described in Section 5.1.7. The photometry was obtained from the Hauck and Mermilliod (1998) catalogue.

### 7.2.4 Ages

After converting the theoretical tracks by Schaller et al. (1992) from the  $L - T_{\text{eff}}$  plane to the  $M_V - (B - V)$  plane, we estimated the evolutionary ages using an interpolation method analogous to the one described in Section 5.1.6. Errors were also estimated, using a Monte Carlo procedure analogous to the one described in Section 5.2. However, in this case the input variables were the  $(B - V)_0$  colours,  $V$  band magnitudes, parallaxes, and respective measurement errors. The absolute magnitudes  $M_V$  were computed from the parallaxes and  $V$  magnitudes, so the errors of the latter quantities propagated to the former. Then, the  $(B - V)_0$  and  $M_V$  errors were propagated to the ages. The absolute error distribution is shown in Figure 7.4.

## 7.3 Pattern speed determination

Our hypothesis is that it is possible to recover the position of the spiral arms at different time instants by tracing back the orbits of young stars. This hypothesis can be tested by computing the spiral arm pattern speed (cf. Section 2.2) in the manner described in this chapter, because if it is true then we should be able bring all the birthplaces to the present by rotating them by the angle that corresponds to the value of the pattern speed (multiplied by the age of each star) and find a pattern resembling one or more spiral arms (the present position of the spiral arms).

The method adopted to compute the pattern speed consisted in two steps: 1) tracing back the orbit of each star to its birthplace; 2) move the birthplace by an arc of a circle with an angle given by the pattern speed times the age of the star. This is essentially the method used by Amaral and Lepine (1997) and Dias and Lépine (2005): the former traced back the orbits of a sample of open clusters, integrating their orbits in a Galactic potential, and fitted spiral arms to different pattern speeds, choosing as the best estimate the pattern speed which resulted in the best fit; whereas the latter traced back a sample of open cluster along a circular path by an amount equal to their ages times the circular speed value at their positions, and varied the pattern speed until the best fit to an assumed model of the spiral arms was found.

More precisely, our method was a combination of the two aforementioned procedures, although applied to individual stars: we computed the stellar orbits in a Galactic potential, and then searched for a pattern speed that could provide a good fit to an assumed model of the spiral structure in the present. From the

selection of spiral arm structure models reviewed in Section 2.2, the cartographic model by Vallée (2008) was favoured as a representation of the present large scale spiral arm pattern because:

1. it was based on the average properties (pitch angle, number of arms and shape, for example) of previous determinations;
2. it was fitted to recent observational data, including (but not limited to) the observed arm tangents;
3. it has a simple mathematical representation (logarithmic spiral).

The Vallée (2008) model consists in four arms with a logarithmic shape given, in  $(r, \theta)$  polar coordinates, by (see also Section 2.2):

$$r(\theta) = r_0 e^{b\theta + n \times 90^\circ + \phi}, \quad (7.5)$$

where  $b = \tan p$  and  $n = 0, 1, 2, 3$ . The derived model parameters were: the pitch angle,  $p = 12.8^\circ$ , the initial radius  $r_0 = 2.1$  kpc and the initial phase  $\phi = -20^\circ$ . A detailed description of the pattern speed fitting procedure follows:

1. The first step was to compute the birthplaces of all stars. To this end, a procedure similar to the one described in Section 5.2 was used, with the following differences: the distances were determined directly from the parallaxes, ages were determined from the absolute magnitudes and  $(B - V)$  colours as described in Section 7.2.4, and the orbit was integrated from the present instant until the time instant corresponding the evolutionary age. The uncertainties in parallaxes, colours, proper motions and brightness, were propagated in the Monte Carlo procedure.
2. To each star corresponds a birthplace  $(x_i(0), y_i(0), z_i(0))$  and an evolutionary age  $\bar{t}_i$ . However, since the orbits are mostly confined to the Galactic plane we assumed  $z_i(0) \simeq 0$ . The uncertainties in the coordinates were given by  $\sigma_x(i)$  and  $\sigma_y(i)$ , plus an extra term depending on the age uncertainty,  $\sigma_t(i)$ . This last uncertainty was not considered in the fitting procedure for reasons that will be explained later.
3. We assumed that the spiral arm pattern in the present is adequately reproduced by the previously mentioned model by Vallée (2008). In Cartesian coordinates we have:

$$x_s(n, \theta, \psi) = r(\theta) \cos(\theta + \phi_n) \quad (7.6)$$

and

$$y_s(n, \theta, \psi) = r(\theta) \sin(\theta + \phi_n), \quad (7.7)$$

where  $\phi_n$  is the  $n$ th arm initial phase. In general,  $\phi_n = \psi + n \times 90^\circ$  for the  $(n + 1)$ th arm ( $n$  is an integer between 0 and 3), and we call  $\psi$  the *phase* of the spiral arm structure. We also assumed that the spiral arm structure rotates as a rigid body with pattern speed  $\Omega_p$ .

4. The birthplaces were rotated by the angle  $\Omega_p \bar{t}_i$  to find their positions in the present (that we assume to be comoving with the spiral arms). Thus, the coordinates of these points are given by:

$$x_i(t_i) = x_i(0) \cos(\Omega_p \bar{t}_i) - y_i(0) \sin(\Omega_p \bar{t}_i) \quad (7.8)$$

and

$$y_i(t_i) = x_i(0) \sin(\Omega_p \bar{t}_i) + y_i(0) \cos(\Omega_p \bar{t}_i). \quad (7.9)$$

5. The minimum distances of each point  $(x_i(t_i), y_i(t_i))$  to each spiral arm ( $d_1(i)$ ,  $d_2(i)$ ,  $d_3(i)$  and  $d_4(i)$ ), weighted by the uncertainties  $\sigma_x(i)$  and  $\sigma_y(i)$ , were computed and the minimum of these four distances chosen as the distance of the point to the spiral structure. Thus, assuming the coordinates are independent:

$$d_n(i) = \frac{(x_i(t_i) - x_s(n, \theta_{\min}, \psi))^2 + (y_i(t_i) - y_s(n, \theta_{\min}, \psi))^2}{\sigma_x(i)^2 + \sigma_y(i)^2}, \quad (7.10)$$

where  $\theta_{\min}$  is the angle corresponding to the minimum distance. The angle  $\theta_{\min}$  was computed using a bisection method: in the  $j$ th quadrant the distances to the end points  $(x_s(n, (j - 1) \times 90^\circ, \psi), y_s(n, (j - 1) \times 90^\circ, \psi))$  and  $(x_s(n, j \times 90^\circ, \psi), y_s(n, j \times 90^\circ, \psi))$  were determined, then the point corresponding to the smallest of these distances and the midpoint became the new end points and this process was repeated until the difference between the end points became smaller than  $\epsilon$  (a small positive number). The minimum distance is then given by:  $\mathcal{D}(i) = \min(d_1(i), d_2(i), d_3(i), d_4(i))$ .

6. The target function

$$\mathcal{F}(\Omega_p, \psi) = \frac{\sum_i \mathcal{D}(i)}{\sum_i 1/(\sigma_x(i)^2 + \sigma_y(i)^2)} \quad (7.11)$$

was minimised using an implementation of the Nelder-Mead simplex algorithm in PYTHON called FMIN, part of the SCIPY package. The final result were estimates of the parameters  $\Omega_p$  and  $\psi$  which produces a maximum clustering of birthplaces around the assumed present position of the spiral arms. Note that  $\mathcal{F}(\Omega_p, \psi)$  is a weighted mean of the distances from the birthplaces to the assumed model, hence it is measure of the dispersion of the observed points relative to the model. For this reason,  $\mathcal{F}(\Omega_p, \psi)$  is also an estimate of the half-width of the spiral arms.

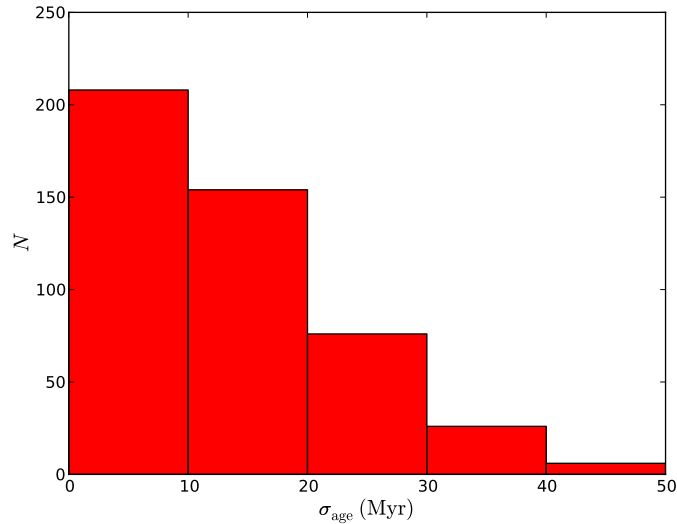


Figure 7.4: Distribution of the Hipparcos sample absolute errors in the evolutionary age determination.

### 7.3.1 Effect of age uncertainty

Contrary to what happens when the orbits of runaway stars are computed, in this case the uncertainties in the determination of evolutionary ages propagate to uncertainties in the location of the birthplaces,  $(x_i(0), y_i(0), z_i(0))$ . In principle, one could think that this does not represent any problem and that it is only a matter of propagating the uncertainties through the Monte Carlo code. However, the absolute errors in the estimated ages of the Hipparcos sample can be as high as 50 Myr, as can be seen in Figure 7.4. This is quite problematic when we note that a star in the solar neighbourhood does a full revolution around the Galaxy in roughly 220 Myr which is only about four times the worst absolute errors.

Since the orbits of these stars are nearly circular, the uncertainties in ages propagate mostly to uncertainties in the azimuthal coordinate along the orbit. Therefore, when the absolute errors are a large percentage of the total orbital period, a systematic effect appears that causes the average birthplace location (in Cartesian coordinates) to “drift” away from the orbital path. This is really a manifestation of the breakdown of the first-order approximation used in the derivation of the usual error propagation formula, i.e. second-order and maybe higher-order effects become important. Thus, it does not help to compute the average in polar coordinates.

Nevertheless, this systematic deviation is partially cancelled once the birthplaces are rotated back to their present position by  $\Omega_p t_i$ . Hence, a possible solution could be to propagate the age uncertainties throughout the fitting procedure, up to the stage where the present positions of the birthplaces are computed, after being rotated by the pattern speed. However, this method would not work because the systematic effect is cancelled by an amount proportional to  $|v_c(r)/r - \Omega_p|$ . As a consequence, the fit would result in a pattern speed as close to  $v_c(8)/8$  (the value of

---

the local circular speed) as possible, i.e. the systematic effect would be introduced in the fit.

For the reasons stated, and considering that most of the influence of age uncertainty is cancelled in the end, we decided to do a fit using only the average evolutionary ages. However, after finding the pattern speed we were still able to compute the total error (i.e. including the contribution of the ages' uncertainties) in the coordinates of the birthplaces, assuming the pattern speed obtained.



# Chapter 8

## Spiral arms and pattern speed

### 8.1 Results

In this section, we present the results of the fitting procedure described in Section 7.3. The first step of the procedure was the determination of the Hipparcos sample stars' birthplaces. The result of this first step is shown in Figure 8.1. An important conclusion that can be extracted from this plot is that almost all stars appear to be on similar quasi-circular orbits, with radius oscillating with an amplitude of  $\simeq 2$  kpc (between 6 kpc and 8 kpc). From the fit to the Hipparcos sample we derived a spiral arm pattern speed and corresponding present phase  $\psi_0$ . We have also estimated the errors in the two quantities using a Monte Carlo method: we repeated the same procedure 1000 times, varying the initial position of the stars according to the respective uncertainties (assumed Gaussian), obtaining a distribution of pattern velocities and initial phases in the end (the errors correspond to the standard deviations of these distributions). For the purpose of this Monte Carlo procedure we assumed that the error in age determination introduces an factor of 0.5 kpc extra uncertainty in the position.

The position of the birthplaces in the present (i.e., after being rotated by the estimated pattern speed  $\Omega_p = 24.9 \text{ km s}^{-1} \text{ kpc}^{-1}$  times the corresponding evolutionary ages) is shown in Figures 8.2 and 8.3. Note that the statistical uncertainties in the evolutionary ages estimates were propagated to the errors in the position of the birthplaces after the determination of the pattern speed, as explained in Section 7.3.1. These plots suggest that the estimated pattern speed produces a reasonable fit to the present position of the spiral arms (this is analysed in more detail in Section 8.2.1). For this reason we have some confidence that we are able to trace the position of the spiral arms using the method proposed (tracing back the orbits of early type stars).

Having established the pattern speed and the present phase of the spiral arms using the Hipparcos sample, we applied the same method (cf. Section 7.3) to a sample of high Galactic latitude runaway stars to test whether similar results could be obtained using these stars. From our original sample of high Galactic latitude runaway stars, we selected only stars whose birthplaces had coordinates with

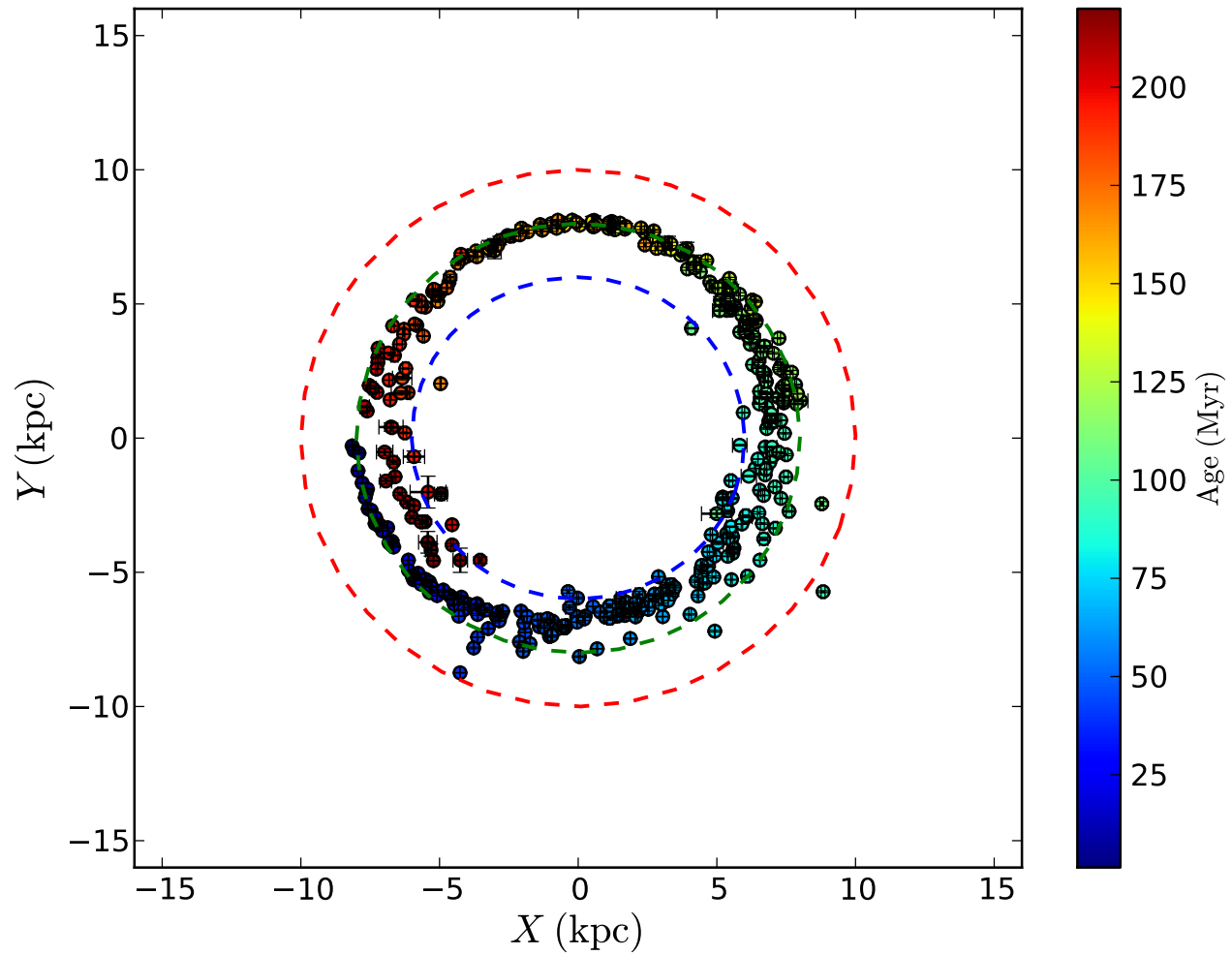
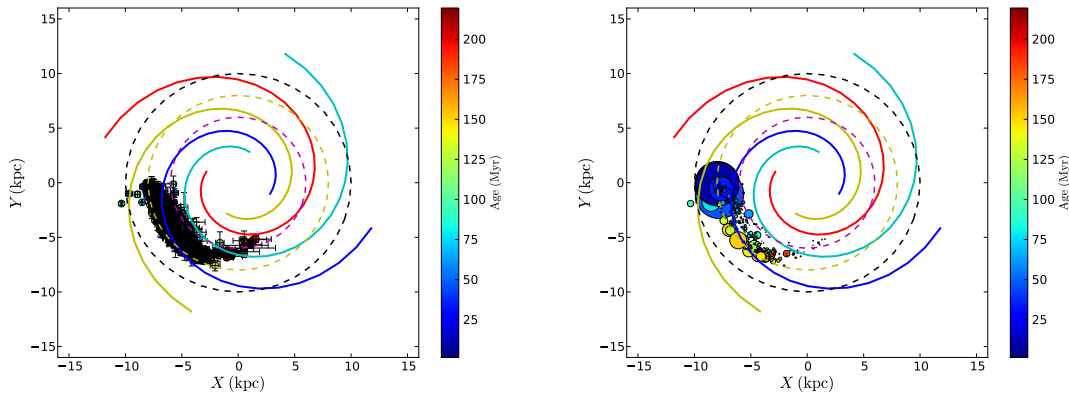


Figure 8.1: Birthplaces of Hipparcos sample stars shown in a galactocentric frame of reference. The three dashed circles correspond to the 6 kpc, 8 kpc and 10 kpc radii in ascending order.

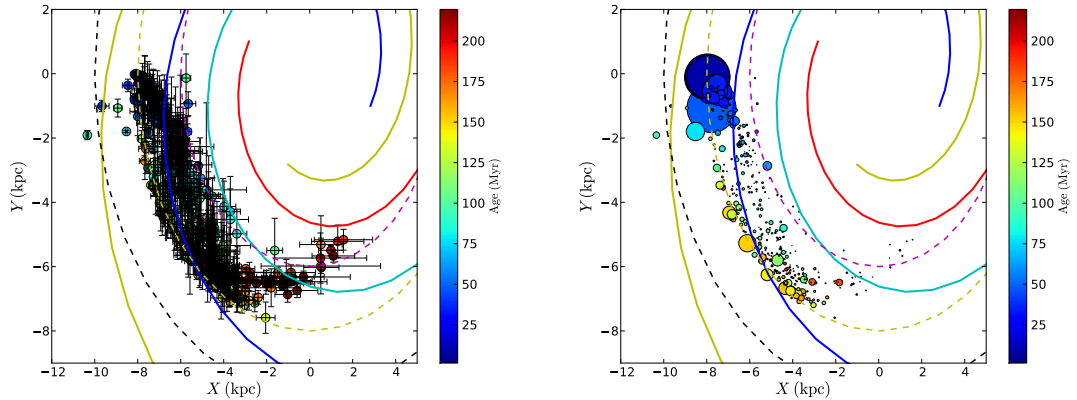


(a) Birthplaces of Hipparcos sample stars after rotation by  $\Omega_p = 24.9 \text{ km s}^{-1} \text{ kpc}^{-1}$  times the evolutionary age (with error bars).

(b) Birthplaces of Hipparcos sample stars after rotation by  $\Omega_p = 24.9 \text{ km s}^{-1} \text{ kpc}^{-1}$  times the evolutionary age (scatter plot).

Figure 8.2: Plot showing the result of the birthplaces' fit to the present position of the spiral arms. The birthplaces were rotated by the computed pattern speed multiplied by each star's evolutionary age. Also plotted are the spiral arms in their present position and the same dashed circles seen in Figure 6.5. The position of the spiral arms is rotated by the phase derived from the fit:  $\psi = -19.5^\circ$ . In (a) the birthplaces are plotted with respective error bars, whereas in (b) they are represented as circles, for better visualisation. The size of the circles is inversely proportional to the error.

errors smaller than 1.5 kpc (cf. Figure 6.5). This is a quite small sample with only 29 stars but our intention was merely to do a qualitative comparison between the two samples, as our objective was to show whether the proposed technique may work when applied to high Galactic latitude runaway stars. A summary of the comparison between the two samples can be seen in Table 8.1: the sample of runaway stars produces estimates that are similar to the ones obtained with the Hipparcos sample, especially if we take into account that, if we consider a given sample, a lower fitted value of the phase implies a higher pattern speed, and vice-versa. In fact, when taking the respective errors into account we conclude that the estimates obtained from the two different samples are consistent (note that the errors for the Hipparcos sample estimate depend mostly on the errors in the age determination, whereas the errors for the runaway stars sample result mostly from the comparatively poorer quality of the astrometric data). The estimated errors also imply that our estimates of the pattern speed are consistent with most values derived in other studies, which range from  $\Omega_p \simeq 20 \text{ km s}^{-1} \text{ kpc}^{-1}$  (Amaral and Lépine, 1997) and  $\Omega_p \simeq 24 \pm 1 \text{ km s}^{-1} \text{ kpc}^{-1}$  (Dias and Lépine, 2005), to  $\Omega_p \simeq 30 \text{ km s}^{-1} \text{ kpc}^{-1}$  (Fernández et al., 2001, with an uncertainty varying between  $2 \text{ km s}^{-1} \text{ kpc}^{-1}$  and about  $7 \text{ km s}^{-1} \text{ kpc}^{-1}$  depending on the specific tracer). Although our own estimates, considering the errors, would agree with any value in the range  $20 - 30 \text{ km s}^{-1} \text{ kpc}^{-1}$ , when put in the context of these other estimates in the literature indicate that a value on the lower side of the range (i.e.  $\sim 20 - 25 \text{ km s}^{-1} \text{ kpc}^{-1}$ ) is more probable. Perhaps more indicative is a plot of the birthplaces from both samples, after being rotated by the pattern speed estimated



(a) Birthplaces of Hipparcos sample stars after rotation by  $\Omega_p = 24.9 \text{ km s}^{-1} \text{ kpc}^{-1}$  times the evolutionary age (with error bars).

(b) Birthplaces of Hipparcos sample stars after rotation by  $\Omega_p = 24.9 \text{ km s}^{-1} \text{ kpc}^{-1}$  times the evolutionary age (scatter plot).

Figure 8.3: Detailed view of the same data presented in Figure 8.2.

Table 8.1: Pattern speed  $\Omega_p$  and present phase  $\psi_0$  obtained by fitting the Hipparcos sample and the runaway stars sample.

Sample	$\Omega_p \text{ (km s}^{-1} \text{ kpc}^{-1}\text{)}$	$\psi_0$
Hipparcos	$24.9 \pm 5.2$	$-19.5^\circ \pm 8.4^\circ$
Runaways	$22.8 \pm 7.8$	$-17.8^\circ \pm 14.3^\circ$

from the Hipparcos sample as shown in Figure 8.4. As can be seen, if we assume this pattern speed for the birthplaces of the high Galactic latitude runaway stars they provide a reasonable (although not perfect) fit to the present position of the spiral arms (assuming the phase derived from the Hipparcos sample:  $\psi_0 = -19.5^\circ$ ).

## 8.2 Discussion

### 8.2.1 Large scale structure and small scale substructures

As can be seen in Figures 8.2 and 8.3, the fit of the birthplaces to the assumed present position of the spiral arms, although not perfect, is acceptable within the errors. This is particularly clear in the scatter plot in Figure 8.3, since the larger circles (which correspond to smaller errors) tend to be clustered around the arms rather than inside the inter-arm regions. Furthermore, the arms, as traced by young stars, have finite width so it should not be expected that all points lie exactly on the curve. In fact, the average arm width estimated from Equation (7.11) was  $\overline{W} = 1.58 \text{ kpc}$ , which is comparable to the  $\overline{W} = 1.32 \text{ kpc}$  estimated by Russeil (2003), but much higher<sup>1</sup> than the  $0.5 \text{ kpc}$  suggested by Lépine et al. (2011). Nevertheless, the presence of spiral arm tracers in regions between the arms is

<sup>1</sup>Note that the width is not the same for all tracers: the arms traced by gas are narrower than the arms traced by the stellar content.

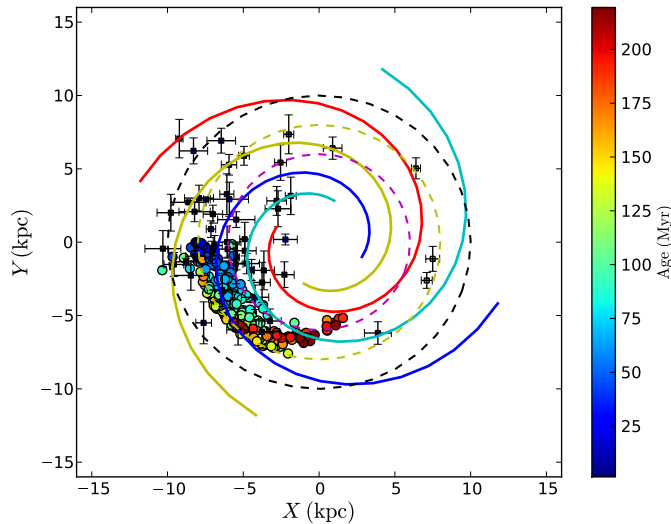


Figure 8.4: Plot showing both the Hipparcos sample and runaways sample stars’ birthplaces after being rotated by the computed pattern speed  $\Omega_p = 24.9 \text{ km s}^{-1} \text{ kpc}^{-1}$  times their evolutionary ages. Hipparcos sample and runaway stars are plotted as coloured circles and squares with error bars, respectively. Only runaway stars with standard deviations  $< 1.5 \text{ kpc}$  are shown. The spiral arms are also plotted in their current position, as in Figure 8.2.

common to most studies (e.g. Russeil, 2003; Dias and Lépine, 2005), and may be caused by the measurement errors or star formation episodes outside the spiral arms.

Indeed, it is worth noting that the fit of the spiral structure by a logarithmic curve was intended as a rough approximation to the large scale structure, as it is well known that spiral arm patterns do not have a perfectly regular design (Elmegreen and Elmegreen, 1995): arm bifurcations, spurs, and other local substructures are common in other spiral galaxies. In the case of our Galaxy, large scale continuous arms appear to coexist with smaller-scale structures (Vallee, 1995 and references therein) as exemplified by the local Galactic disc and the Gould Belt (Elias et al., 2006 and references therein).

It is interesting to note that most stars appear to have originated from the “blue” arm (the arm closest to the Sun that should be identified with the Carina-Sagittarius arm, cf. Vallée, 2008). This arm is also the most prominent in other studies, using a variety of tracers: HII star forming complexes (Russeil, 2003), Cepheid stars (Majaess et al., 2009), and CS sources (Lépine et al., 2011). In other words, this arm appears to be a major arm, similar to the well defined arms usually seen in grand design spiral galaxies. On the other hand, very few stars were apparently born in the other arms, and in particular there is a paucity of birthplaces in the “yellow” arm relative to the “cyan” arm (to be identified with Crux-Scutum and Perseus arms, respectively, cf. Vallée, 2008), even though the former is closer to the Sun than the latter. This is probably related to the position relative to the corotation radius (cf. Section 8.2.2) and possibly the decrease of stellar density with radius (the subject is further developed in Section 8.3).

Nevertheless, many birthplaces, corresponding to the younger ( $\lesssim 50$  Myr) stars, are poorly fitted by the spiral arms, since their short lifetimes mean that they remain in the solar neighbourhood. These stars are better understood as members of local star formation features, in particular the aforementioned local Galactic disc and the Gould Belt, instead of a product of the spiral arms. In fact, Westin (1985) argues that the Gould Belt feature has an age of  $\lesssim 60$  Myr and that local young stars have different kinematics according to their ages: the system consisting of the younger Gould Belt stars is expanding, whereas the older stars have circular orbits typical of disc stars. The birthplaces of stars belonging to these local features have generally small uncertainties (as can be seen in Figure 8.3), consequently they have a large influence in the quality of the fit, especially because they are so far from the spiral arms. This fact probably explains why the estimated arm width was so large.

## 8.2.2 Corotation radius

The circular speed  $v_c(r)$  in our Galaxy is roughly constant for a wide range of radii (see Section 4.2.1). Thus, the angular speed  $\Omega(r) = v_c(r)/r$  is a decreasing function of radius. On the other hand, the pattern speed  $\Omega_p$  is assumed to be constant, hence, there is a radius  $R_c$  for which  $\Omega(R_c) = \Omega_p$ , called the *corotation radius*. According to our estimate  $\Omega_p = 24.9 \text{ km s}^{-1} \text{ kpc}^{-1}$ , hence the corotation radius derived from the adopted rotation curve (Section 4.2.3) is 8.7 kpc, or  $R_c = 1.088R_0$ , where  $R_0$  is the distance of the Sun to the Galactic Centre (Section 4.2.1).

There is an important implication of a corotation radius close to the value of the distance of the Sun to the Galactic Centre: episodes of star formation in the solar neighbourhood are connected to the passage of the spiral arms through the Sun's position (as can be inferred from star formation rate studies, e.g. Rocha-Pinto et al., 2000; de la Fuente Marcos and de la Fuente Marcos, 2004). It has been argued (Leitch and Vasisht, 1998) that the passage of the Sun through a spiral arm is a trigger of mass extinction episodes on Earth<sup>2</sup>. For this reason, the position of the Sun near the corotation radius is probably a necessary condition for the existence of life on Earth. Marochnik (1983) had already speculated that life-supporting planets are probably concentrated in the corotation ring around the Galaxy.

Thus, the existence of a great diversity of life forms could be by itself an argument that the computed pattern speed value,  $\Omega_p = 24.9 \text{ km s}^{-1} \text{ kpc}^{-1}$  is a good estimate.

Another estimate of the corotation radius was obtained by Amôres et al. (2009), who observed a gap in the density distribution of HI gas predicted by theory to

---

<sup>2</sup>It is proposed (Leitch and Vasisht, 1998) that the extinction events are the result of encounters with supernovas or collisional encounters with gas/dust clouds, which may scatter Oort cloud bodies triggering comet impacts in the Earth's surface. Both these events are far more likely in the environment within a spiral arm.

occur at the corotation radius. The estimated value,  $R_c = 1.1R_0$ , also agrees quite well with our own estimate.

### 8.2.3 Error associated with age determination

As we have seen, the orbits of the Hipparcos sample stars are almost circular, consequently the determination of the birthplaces depends on the estimated evolutionary ages in two ways: a greater evolutionary age produces a greater azimuthal displacement and, as can be seen in Figure 8.1, there is a radial oscillation as a function of time. For this reason, the uncertainties in age determinations are propagated to the final position of the birthplaces (see Section 7.3.1) and may cause the estimated birthplace to deviate from the real position of the corresponding spiral arm. However, the azimuthal component will not have a critical influence in the final result since the ages are used first to find the birthplace, and then the birthplace is rotated to its present position<sup>3</sup>. Thus, a large fraction of the face value uncertainties cancel out. However, the age uncertainty is an important source of error in the in the spiral arm fit, and thus in the pattern speed estimation.

There are not many methods available to determine the ages of isolated stars. The available methods are evaluated in a recent review by Soderblom (2010). In the case of the Hipparcos sample (large sample of main sequence stars), we are limited to the method used in our study: fitting to theoretical evolutionary tracks. According to Soderblom (2010), random errors of 20 to 50 per cent should be expected, although early type stars should correspond to the lower limit of this range (compare with the 20 per cent estimate in Dias and Lépine, 2005). However systematic effects should also be expected (caused by the degeneracy discussed in Section 5.1.6, for example). Furthermore, in our analysis of the Hipparcos sample we have ignored the metallicities which also affects the age estimates: stars with lower metallicities stay longer on the main sequence implying longer lifetimes. Nevertheless, it is possible to constrain the effect of age errors on the positions to a maximum of about 2 kpc, as we have already seen.

However, in the case of high Galactic latitude runaway stars we have a second method available to us to estimate the ages. The orbits are traced back to a specific  $z$  coordinate (corresponding to the Galactic plane), defining the flight times. It is expected from theory, and can be verified to some extent in Figure 6.1, that the flight times correlate well with the ages, i.e. runaway stars are ejected soon after they are born. Ages estimated using this method are called *kinematical* ages (Soderblom, 2010). Furthermore, an abundance analysis is usually part of any study on high Galactic latitude runaway stars, thus usually evolutionary ages can be estimated with greater accuracy. Nevertheless kinematical ages are in principle better estimates (Soderblom, 2010).

In summary, in principle high Galactic latitude runaway stars are probably better suited to serve as spiral arm tracers than normal field stars, in terms of the

---

<sup>3</sup>However, note that there is a dependency of the radial oscillations with the azimuthal “phase”. Thus, the azimuthal component still influences the outcome.

quality of age estimates. However, the quality of the observational data is still critical and even more so than in the case estimates from fits to theoretical evolutionary tracks, since kinematical age estimates depend not only on atmospheric parameters but also on astrometric parameters to achieve maximum precision.

### 8.3 Comparison with a simulated sample

Even a cursory glance at Figures 8.2 and 8.3 immediately raises a few questions: why are there so few data points in the region of the “yellow” arm? Is this an artifact of the fitting procedure? Can a model based on our assumptions about the shape of the spiral arms and the gravitational potential produce this result?

To answer this last question we decided to perform a simulation based on our assumptions relative to the dynamics of the arms and stars. We essentially start in the past with stars distributed along the spiral arms and follow the movement of both the stars and the spiral arms (who create more stars in their wake) until we arrive at the present. Then we select a sample of simulated stars using the same *criteria* we used to select the real sample in Section 7.2.

For our assumptions to be self-consistent both samples must have roughly similar properties. In other words, using the observed local velocity distribution to find the pattern speed and arm membership distribution, and using the computed pattern speed to find the local velocity distribution and arm membership distribution, should produce compatible results (because the same assumptions about the nature of the spiral arms and gravitational potential are made in both cases).

#### 8.3.1 The simulation

The simulation was implemented in FORTRAN. It was based on a Monte Carlo method, with successive generations of stars being created in random positions, and with random initial velocities, along the moving spiral arms. We should note that the objective was not to produce a realistic model of the Galaxy, but only to test the assumptions in the determination of the spiral pattern speed. The following assumptions and simplifications were made:

- the spiral arms are adequately represented by the same logarithmic four-arm spiral model used in Section 7.3, and rotate as a rigid body with the pattern speed  $\Omega_p$ ;
- stars are created in the position occupied by the spiral arms at any given instant according to the theoretical framework presented in Section 2.2;
- the Galaxy’s gravitational potential and associated rotation curve are the ones given in Section 4.2.3, and the perturbation induced in the potential by the spiral arms is ignored;

- the velocity of a star can be represented by the vector  $(v_x, v_y + v_c(r), v_z)$ , where  $v_c(r)$  is the speed of the standard of rest at a distance  $r$  from the Galactic Centre (determined from the rotation curve), and  $v_x$ ,  $v_y$  and  $v_z$  are the components of the velocity of the star relative to its standard of rest, which are assumed to follow a Gaussian distribution (i.e. the speed has a Maxwellian distribution);
- the stars only move along the orbits as determined by the chosen potential and do not interact with each other or with the spiral arms;
- effects caused by stellar evolution are ignored and all stars are considered equal to each other.

The simulation starts at an instant  $T_0$  with the creation of  $N$  stars along each spiral arm (generation 1). As was already mentioned, the initial positions and velocities are random (within certain constraints).

Then it advances to the instant  $T_1 = T_0 + \Delta T$ , where  $\Delta T$  is the time step, by moving all generation 1 stars along their orbits a distance corresponding to the interval  $\Delta T$ , and rotating the spiral arms by an angle  $\Omega_p \Delta T$ . Moreover, still in instant  $T_1$ ,  $N$  generation 2 stars are created along the new position of the spiral arms in the same conditions as population 1 stars. Thus, at this point there are  $8N$  stars in total, with half of them located in the position of the spiral arms and another half having moved from the previous position of the spiral arms along their orbits, which are function of their initial positions and velocities.

When the simulation advances to the instant  $T_2$ , generation 1 and generation 2 stars move from the positions occupied at instant  $T_1$  along their orbits and the spiral arms rotate again by an angle  $\Omega_p \Delta T$ , marking the positions for the creation of generation 3 stars. By this point, generation 1 and generation 2 stars have moved away from their original positions a distance along their orbits corresponding to the time intervals  $2\Delta T$  and  $\Delta T$  respectively, whereas the spiral arms have rotated by an angle  $2\Omega_p \Delta T$  in total, relative to their original position. This procedure is repeated until the  $j$ th generation is created, with the spiral arms having rotated  $(j - 1)\Omega_p \Delta T$  in total.

In the end, all stars located in the solar neighbourhood (in the same region as the observed sample, cf. Section 7.2) are selected to serve as the simulated sample for comparison purposes.

A detailed description of each step in the implementation of the simulation follows.

**Initialization** The first step was to initialize the variables defining the spiral arms, and other parameters of the simulation. The chosen initial parameters were: number of stars per spiral arm per time step  $N = 10000$ , time step  $\Delta T = 20$  Myr and number of time steps  $n_{\text{steps}} = 10$  (thus corresponding to a total time of 200 Myr, close to a full rotation of the disc). As in Section 7.3,

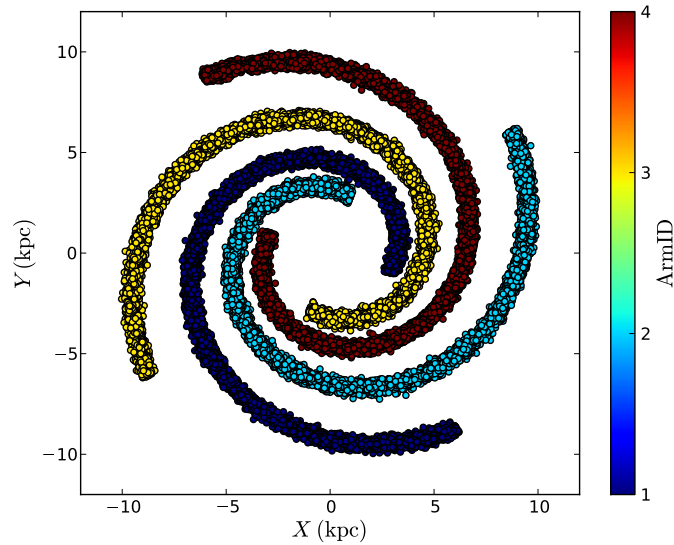


Figure 8.5: The position of newly-created stars in the final iteration (10th generation) of the simulation. The position of the arms corresponds to what we assume is the present position (phase  $\psi = -19.5^\circ$ .)

the spiral arms were defined by two parameters: pitch  $p = 12.8^\circ$  and initial radius  $r_0 = 3$  kpc. The pattern speed was the one computed in this work:  $\Omega_p = 24.9 \text{ km s}^{-1} \text{ kpc}^{-1}$ . The initial phase,  $\psi_0$ , was chosen in such way as to make the spiral arms coincide with their present position by the end of the simulation, thus  $\psi_0 = 200\Omega_p - 19.5^\circ$ .

**Spatial distribution** Having defined the shape and initial position of the spiral arms, the next step was to distribute stars along them. They were distributed randomly in the plane according to the following method: first a point P belonging to a spiral arm was chosen at random; then a second point Q was chosen randomly from the line perpendicular to the spiral arm at P. In order to generate point P only an angle is needed according to Equation (7.5), however the *naïve* approach of generating this angle from the uniform distribution is incorrect because of the logarithmic nature of the spiral curve. To ensure an uniform distribution of points along the curve we had to parametrize the curve correctly, i.e. with its natural parametrization (see Section 2.6.2 of Neves, 2009):

$$\theta_P = \frac{1}{\tan p} \ln \left( \frac{u}{\frac{r_0}{\tan p} \sqrt{\tan^2 p + 1}} + e^{\tan p \psi_0} \right), \quad (8.1)$$

where  $u$  is the length along the curve when the angle is  $\theta_P$ . By choosing a value for  $u$  from the uniform distribution in the interval  $0 - 35$  kpc we were able to generate points uniformly distributed along the spiral arms. On the other hand, point Q was simply selected from a Gaussian distribution with mean  $r(\theta_P)$  and standard deviation  $0.1625$  kpc. The standard deviation

was chosen to ensure that the spiral arms had a thickness a bit above 1 kpc (Russeil, 2003). This procedure was repeated  $N$  times for each spiral arm in each generation. In Figure 8.5 the final generation is plotted, exemplifying the way the stars were distributed.

**Velocity distribution** After defining the initial position of each star their initial velocities were generated. The initial velocities were decomposed into two components: the velocity of each star’s standard of rest, and the velocity of the star relative to its standard of rest. The velocity of the standard of rest is simply given by the value of the velocity curve at the star’s position  $v_c(r_P)$ . The three components of a star’s velocity relative to its standard of rest ( $v_x, v_y, v_z$ ) were independently generated from Gaussian distributions with zero averages and standard deviations of 10, 10 and 6 km s<sup>-1</sup>, respectively. The standard deviations were estimated from the distributions of the Hipparcos sample stars (see Figures 8.7, 8.8 and 8.9) as an zero-order approximation to the typical velocities of the stars that end up in the solar neighbourhood.

**Dynamics** The previous two steps were repeated in each iteration to create a new generation of stars. At the same time, in each iteration, the spiral arms were moved by an angle  $\Delta T\Omega_p$  and all stars from previous generations moved along their orbits to new positions which were computed as described in Section 5.2. Thus  $x(i\Delta T) = F(x((i-1)\Delta T), y((i-1)\Delta T), z((i-1)\Delta T), V_x((i-1)\Delta T), V_y((i-1)\Delta T), V_z((i-1)\Delta T), \Delta T)$  and the same for the other variables (positions and velocities).

### 8.3.2 Simulation results and discussion

There are two properties of the simulated local sample (simulated stars within 200 pc of the Sun) relevant in this analysis: the distribution according to arm of origin, and the velocity distribution. The former property is not known *a priori* in the case of the observed local sample, whereas the latter is a direct<sup>4</sup> observation. For this reason, although our main interest is the arm membership distribution, the comparison between velocity distributions is the only direct test of consistency.

As can be seen in Figures 8.7 8.8 and 8.9, the distributions of the simulated and observed samples agree quite well, taking into account the simplicity of the model used in the simulation. Also note that the initial distributions adopted in the simulation were purely Gaussian. Thus, since the simulation is capable of roughly reproducing the velocity distribution of the observed stars, our assumptions appear to be self-consistent. This also means that the simulated arm membership distribution (Figure 8.6) can be compared with the one obtained from the fit to the observed stars (as inferred from the plot in Figure 8.3).

<sup>4</sup>The measurement of this velocities depends on other quantities: the distance, velocity of the Local Standard of Rest (LSR) and the velocity of the Sun relative to the LSR.

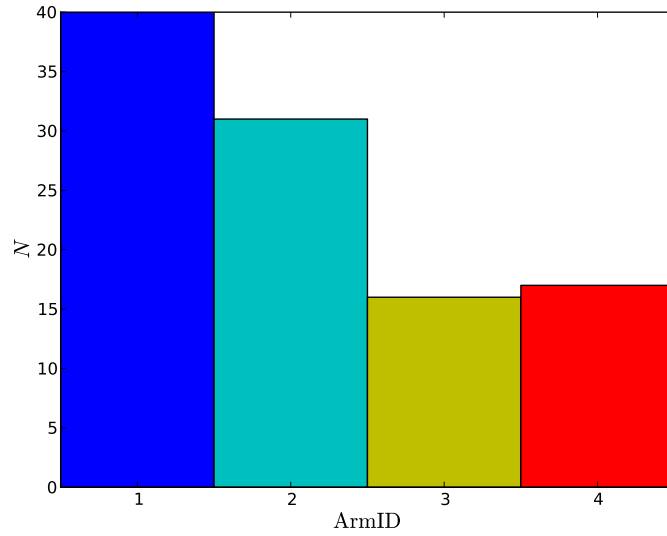


Figure 8.6: Distribution of the simulated stars found in the solar neighbourhood (distance to the Sun  $< 200$  pc) according to the arm they originated from. The numbers and colours are the same as in Figure 8.5.

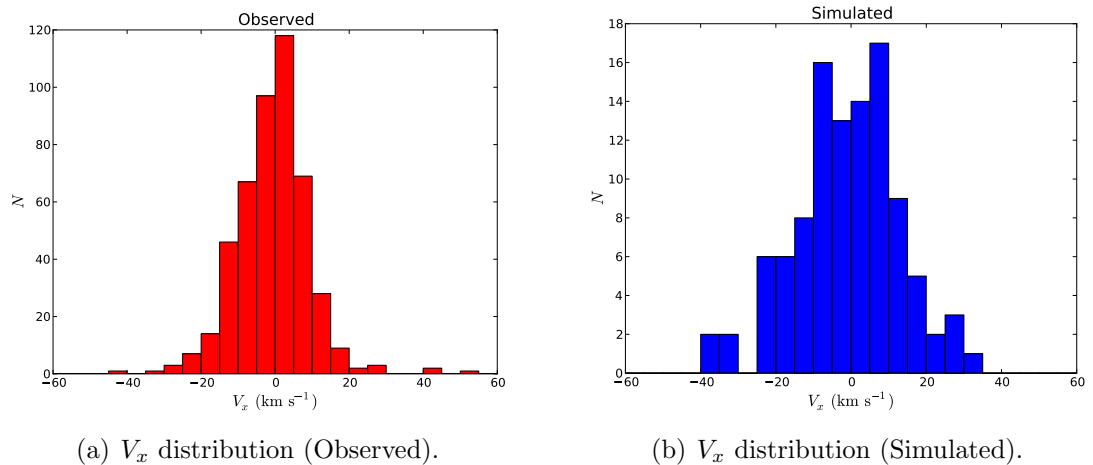


Figure 8.7: Plots comparing the observed and simulated distributions of the velocity's  $x$  component of the local samples.

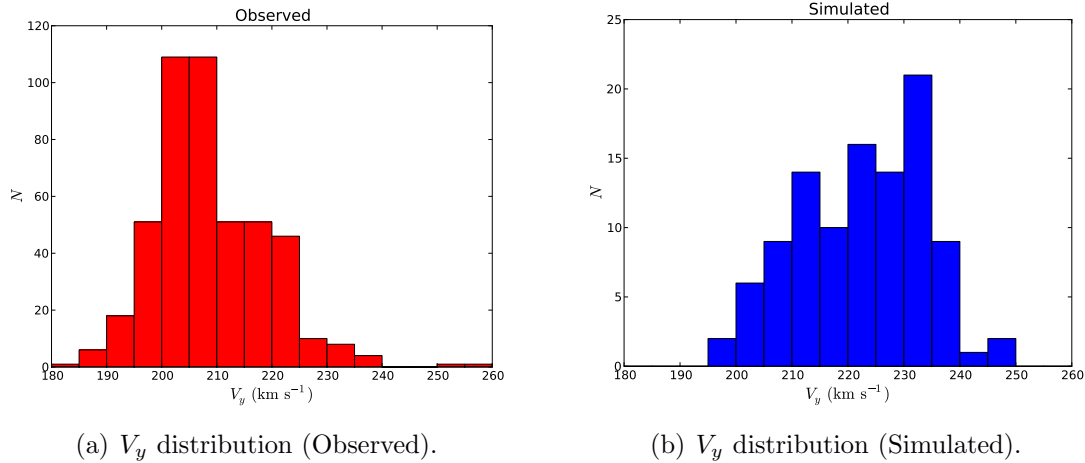


Figure 8.8: Plots comparing the observed and simulated distributions of the velocity's  $y$  component of the local samples.

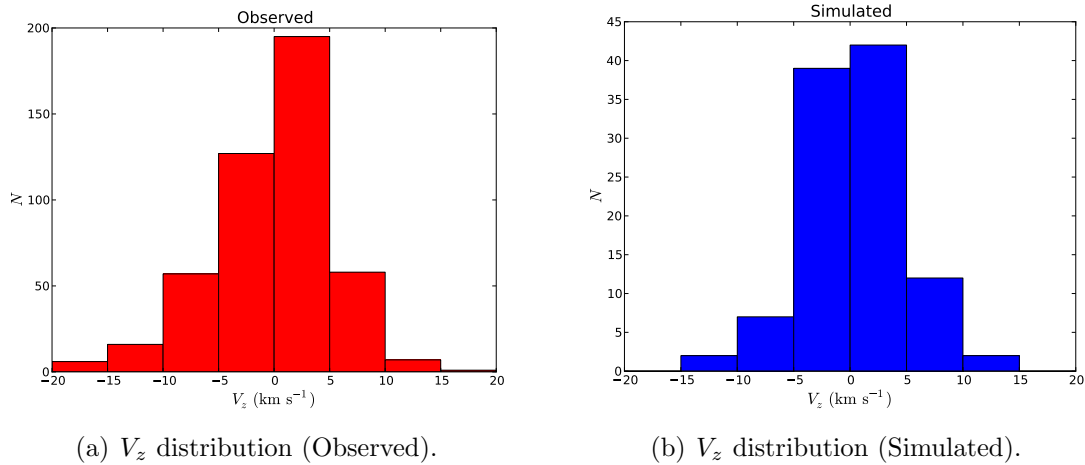


Figure 8.9: Plots comparing the observed and simulated distributions of the velocity's  $z$  component of the local samples.

Our fit of the pattern speed implicates the attribution of the observed stars to different spiral arms, which are assumed to have a certain shape. As can be seen in Figure 8.3, if  $\Omega_p = 24.9 \text{ km s}^{-1} \text{ kpc}^{-1}$ , most stars appear to belong to the arm which is closest to the Sun, the “blue” arm. From the other three arms, the “cyan” arm appears to be the one with most members, with the “red” and “yellow” arms having very few members. This picture roughly agrees with the distribution according to arm of origin in the case of the simulated sample (Figure 8.6), at least in qualitative terms. It is particularly interesting to verify that the local sample includes many more members from the “cyan” arm than the “yellow” arm in spite of being more distant from the Sun. This difference can probably be explained by the effect of differential rotation, the exponential drop in stellar density or a combination of both effects. This question was not pursued further however, as we were satisfied that our model could reproduce this behaviour.

Note that a perfect agreement between the observed and the simulated sample should not be expected, because the simulation was not intended to be an accurate model the Galaxy, but only a test of consistency of our assumptions. In other words, it would only be able to *falsify* the results obtained from the fit, but it would never be able, due to its simplifications, of producing results on its own. The differences between the simulated and observed velocity and arm membership distributions can perhaps be explained by the aspects not included in the simulation, as for example: variation in stellar density along the arms and perturbation in the gravitational potential caused by the arms. It may also be the case that the velocity distribution adopted for newly-born stars is not the most appropriate one.

In summary, the results obtained by fitting spiral arms to a sample of local stars (from Hipparcos) seem to be based on self-consistent assumptions, because we are able to roughly reproduce this sample by performing a simulation that uses the fit results as input. Moreover, the simulated arm membership distribution also resembles (at least qualitatively) the distribution obtained after the fit to the sample of real stars.

# Chapter 9

## Summary and conclusions

### 9.1 Summary

In this dissertation we focused on the study of the kinematical properties of a sample of high Galactic latitude runaway stars, their relationship with hypervelocity stars, and their connection to larger scale structure, as tracers of the spiral arms. High Galactic latitude runaway stars are interesting objects because they are young stars that have traveled long distances away from their birthplaces, into little obscured regions in the Galactic halo. Their atypical positions and kinematical properties raise questions on their exact nature and mechanisms responsible for their ejections.

The main technique used the study of these stars is the determination of their ejection velocities, flight times, and birthplaces (in the Galactic disc) by tracing their orbits back in time, assuming a model for the gravitational potential of the Galaxy, and using good quality measurements of their velocities and positions. However, the large distances of many runaway stars hindered many previous studies, as the accuracy of distance and proper motions measurements is limited in the case of faint, distant stars. Hence, we were able to improve on the results of these studies by combining proper motion measurements from several catalogues, enabling us to improve the accuracy of the proper motion estimates, and to estimate the velocity vector of some high Galactic latitude stars for the first time.

Assuming that star formation occurs preferentially in the spiral arms, and considering that they are found in regions which are largely free from interstellar extinction, we argued that high Galactic latitude runaway stars constitute a good tracer of the spiral arms, capable of tracing even the distant arms on the opposite side of the Galaxy (also because of their high velocities). Hence, the use of runaway stars as tracers of the spiral is a way to address the problem of the shape and structure of the spiral arms. Furthermore, since runaway stars span a wide range in ages, this hypothesis implies they may be used to estimate the spiral arms pattern speed.

Thus, the following questions provide an adequate summary of the problems we wanted to address in this dissertation.

- The high spatial velocities of runaway stars are traditionally explained by two ejection mechanisms: the dynamical ejection mechanism (DEM) and the binary ejection mechanism (BEM). Can these mechanisms explain the ejection of all runaway stars? What can the ejection velocity distribution tell us about the ejection mechanisms? Is there a connection between runaway and hypervelocity stars?
- Assuming that most stars are born in the spiral arms, is it possible to recover their birthplaces by tracing their orbits back in time? Is it possible to trace the position of the spiral arms, and find the corresponding pattern speed, using this information?

## 9.2 Main results and conclusions

A description of the main results and conclusions follows.

**Flight times *versus* evolutionary ages:** most stars in our sample of high Galactic runaways were found to have flight times consistent with their estimated evolutionary ages. Moreover, it was also verified that in most cases stars were ejected from their birthplaces early in their lifetimes, as predicted from theory for both the DEM and the BEM (cf. Leonard and Duncan, 1990; Portegies Zwart, 2000, respectively). However, three stars had flight times exceeding the estimated ages by a large margin: SB 357, EC 20252–3137 and HIP 77131. Possible scenarios capable of explaining this difference were discussed (metallicity overestimation, rapid rotation, blue straggler nature) but no firm conclusion on their nature was achieved.

**Bimodal ejection velocity distribution:** the estimated ejection velocity distribution appears to be bimodal, potentially revealing the presence of two different populations with a cutoff at  $\simeq 350 \text{ km s}^{-1}$ , close to the maximum ejection velocity predicted by theoretical models (Leonard, 1991; Portegies Zwart, 2000). There is a “low” velocity population with a Maxwellian distribution peaked at  $141 \text{ km s}^{-1}$  and a “high” velocity population with ejection velocities of  $400 - 500 \text{ km s}^{-1}$ . A variation of the classical BEM proposed by Przybilla et al. (2008) would be a natural explanation of two features of the distribution: the bimodality, and a limit of the ejection velocity  $\simeq 400 \text{ km s}^{-1}$ . In this variation of the BEM, the very massive companion of the future runaway undergoes a supernova, after passing through a Wolf-Rayet phase, with the system evolving in a common envelope.

**Link with hypervelocity stars:** the possibility that the runaway stars belonging to the high velocity population may be, in fact, hypervelocity stars was also discussed. An origin close to the centre of the Galaxy (the mechanism proposed by Hills, 1988 to eject hypervelocity stars only operates in the Galactic Centre) can be ruled out for most stars, however it cannot be ruled out in the case of the stars HIP 105912 and EC 19596–5356. It is still possible

that they are in fact hypervelocity (or *hyper-runaways*) produced by a third, yet unknown mechanism, capable of ejecting stars with very high velocities away from the Galactic Centre. Gualandris and Portegies Zwart (2007) propose a mechanism consisting of a dynamical encounter between a binary containing the ejected star and an intermediate-mass black hole in the centre of a dense cluster. The main conclusion was that all mechanisms have to be considered together to understand the whole picture, including the BEM, the DEM, the Hills mechanism, and possibly the intermediate-mass black hole interaction mechanism. Ejection velocities up to  $\simeq 300 \text{ km s}^{-1}$  can be explained by both the DEM and the BEM; higher ejection velocities close to  $\simeq 400 \text{ km s}^{-1}$  can be explained by the variation of the BEM proposed by Przybilla et al. (2008) and the most extreme ejection velocities, higher than  $\simeq 450 \text{ km s}^{-1}$  probably need to be explained by the Hills mechanism when they occur in the Galactic Centre, and possibly by the intermediate-mass black hole mechanism when the ejection occurs far from the Galactic Centre.

**Spiral arms pattern speed:** the assumption that it is possible to retrieve the position of the spiral at different time instants, by using the procedure of tracing the orbits of stars back in time, was tested by estimating the pattern speed of the spiral arms and observing whether that estimate corresponded to a good fit to the spiral arm pattern, using a second sample composed of local main sequence B stars (Hipparcos sample). The value of the pattern speed obtained with this second sample was  $\Omega_p = 24.9 \text{ km s}^{-1} \text{ kpc}^{-1}$ . Moreover, the corotation radius derived from this pattern speed agrees with several independent estimates which propose a corotation radius close to the radius of the Solar Circle: e.g Marochnik (1983) suggested that life-supporting planets (like the Earth) are probably concentrated in the corotation ring around the Galaxy. The birthplaces were found to adequately fit the large scale features of the spiral arms, thus the overall conclusion was that is indeed possible to retrieve the position of the spiral arms in different time instants.

**Runaways as spiral arms tracers:** in order to determine the suitability of high Galactic latitude runaway stars as traces of the spiral arms, we estimated the pattern speed using the same method as before, applied to this sample. The value obtained,  $\Omega_p = 22.8 \text{ km s}^{-1} \text{ kpc}^{-1}$ , is not far from the one estimated from the Hipparcos sample of runaway stars. Furthermore, it was noticed that assuming the pattern speed estimated from the Hipparcos sample creates an acceptable fit to the sample of runaway stars. More importantly, we also argued that age uncertainties are one of the main sources of error in application of this method. Thus, high Galactic latitude have the potential of being better tracers of the spiral arms than local OB stars, since it possible to obtain better age estimates (kinematical ages, cf. Soderblom, 2010) of the former considering that it is possible to locate their birthplaces *a priori* (assumed to be in the Galactic disc). Consequently, the use of high Galactic latitude runaway stars as spiral arms tracers is quite promising because it

combines good age estimates with a good coverage of the Galactic plane, since these stars are not obscured by dust and travel far away from their places of birth. At the moment the method is mostly limited by the quality of the astrometric and photometric data, which is bound to increase in the near future due to the expected launch of the Gaia satellite mission. As was already mentioned in Chapter 1, the estimated number of high Galactic latitude runaway stars in our Galaxy is approximately 5000 (as derived in Silva and Napiwotzki, 2011), thus the detection of even a fraction of that number with Gaia would allow us to work with a sample one order of magnitude larger than the current sample. This large number of stars could be binned and used to infer directly the position of the spiral arms in different age bins.

## 9.3 The future

There are essentially two potential directions available for further work (or a combination of both): improve the analysis of the present sample of high Galactic latitude runaway stars, in an attempt to really constraint the theoretical ejection mechanisms; or obtain new samples, either in order to improve the statistics, or to compare different populations of runaways, for example. Here we introduce three projects that we would like to pursue in the future.

### 9.3.1 Simulation of a population of runaway stars

The objective would be to implement updated models for both ejection mechanisms to create a synthetic population of runaway stars to compare with the observed sample, or other samples. This would be an appropriate way to test and constraint the existing theoretical ejection mechanisms. The model for the BEM should include the variation proposed by Przybilla et al. (2008), where the companion star is a Wolf-Rayet star. For the dynamical ejection mechanism we propose the model by Allison et al. (2009) or an improved version. The initial conditions, in particular the spatial distribution, are difficult to chose. Data from the Gaia mission would greatly help this effort.

### 9.3.2 Runaway stars in nearby galaxies

The study of runaway stars in the (resolved) halo of nearby (edge-on) galaxies (NGC 55, for example) has an advantage over the same study in our own Galaxy. Since the external galaxy would be visible in its entirety, a census of all the population of halo runaway stars would be possible. The relevant statistics of the observed population (colour, brightness, and mass, for example) could be compared with the ones observed in our Galaxy and with predictions by theoretical models. The greatest challenge is the background subtraction. In order to identify the runaway stars it is necessary to use an appropriate system of filters, capable of enabling an estimate of the surface gravity through the Balmer discontinuity.

A similar effort was conducted by Bond (2005) with PAGB stars in an attempt to use them as standard candles. We could apply a similar method to the runaway stars problem.

### 9.3.3 Gaia catalogue of runaway stars

The Gaia satellite mission, with launch planned for 2013, promises astrometric data with unprecedented quality, together with broad and medium range photometry, and low resolution spectroscopy. It will permit, in principle, the detection of all stars, including radial velocity and proper motions measurements, up to a brightness  $V = 17$  (up to  $V = 20$  without radial velocities). A  $V = 17$  brightness corresponds to a distance of  $\simeq 25$  kpc for a B9 type star. Moreover, an astrometric accuracy of  $\sim 20 \mu\text{as}$  for  $V = 17$  will be reached (Jordi et al., 2010 and references therein).

These high quality data will permit the identification of many runaway stars, as absolute magnitudes and rotation velocities will be available up to distances of  $\simeq 10$  kpc with an accuracy of 10 per cent (Jordi et al., 2006 and references therein). Thus we would like to use the astrometric, photometric and spectroscopy capabilities of the Gaia satellite in order to build a catalogue of runaway stars that can be used to improve the answers of the questions addressed in this dissertation. In particular, it should be possible to trace the spiral arms using the technique we proposed.



# Appendix A

## Data for main sequence stars

In this Appendix we present the relevant data for the stars classified as main sequence. In Tables A.1 and A.2 the values used as input to compute the orbits are shown for the groups A and B respectively. The proper motions were obtained from a combination of the values from UCAC2 (Zacharias et al., 2004), USNO-B (Monet et al., 2003), Tycho-2 (Høg et al., 2000) and Hipparcos (van Leeuwen, 2007), SuperCOSMOS, SPM (Girard et al., 2004), and NPM2 (Hanson et al., 2003), by a weighted average. The gravities, temperatures and projected rotation velocities were taken from the literature or computed from Strömgren  $uvby\beta$  photometry as indicated. Note that these are the measured gravities and temperatures not corrected for the gravitational darkening effect. The masses were derived from the evolutionary tracks of Schaller et al. (1992).

In Tables A.3 and A.4 data concerning the present condition of the stars (present coordinates  $(X, Y, Z)$ , distances and evolutionary ages) and the condition at the moment of ejection from the disk (point of ejection in the plane  $(X_0, Y_0)$ , flight time and ejection velocities) are shown. All coordinates are given in a galactocentric Cartesian right-handed frame of reference. The evolutionary ages were obtained by interpolating the evolutionary tracks of Schaller et al. (1992).

Table A.1: Input data for stars belonging to group A. The data shown are: the radial velocity, the proper motions in right ascension and declination directions, the surface gravity, temperature, mass and projected rotation velocity.

Name	r.v. (km s <sup>-1</sup> )	p.m. $\alpha \cos \delta$ (mas yr <sup>-1</sup> )	p.m. $\delta$ (mas yr <sup>-1</sup> )	log $g$ (cm s <sup>-2</sup> )	$T_{\text{eff}}$ (K)	Mass (M <sub>⊙</sub> )	$v \sin i$ (km s <sup>-1</sup> )
EC 19337-6743	-17 ± 10 (14)	6.24 ± 0.50	-5.64 ± 0.61	3.90 ± 0.20 (14)	10000 ± 2000 (14)	2.8 <sup>+0.8</sup> <sub>-0.7</sub>	200 (14)
EC 05515-6231	-12 ± 10 (14)	-1.36 ± 0.86	6.49 ± 0.85	4.20 ± 0.20 (14)	14000 ± 2000 (14)	3.8 <sup>+0.3</sup> <sub>-0.3</sub>	65 (14)
EC 20089-5659	-24 ± 10 (14)	3.61 ± 0.70	-7.97 ± 0.72	3.90 ± 0.20 (14)	14000 ± 2000 (14)	4.4 <sup>+0.1</sup> <sub>-0.9</sub>	90 (14)
EC 03462-5813	39 ± 10 (19)	3.33 ± 0.64	21.77 ± 0.65	4.20 ± 0.20 (19)	13500 ± 675 (19)	3.6 <sup>+0.4</sup> <sub>-0.4</sub>	200 (19)
EC 05582-5816	81 ± 10 (19)	9.85 ± 0.91	10.10 ± 0.84	4.00 ± 0.20 (19)	17000 ± 850 (19)	5.6 <sup>+0.7</sup> <sub>-0.6</sub>	170 (19)
EC 10087-1411	105 ± 10 (19)	-9.34 ± 0.76	-5.92 ± 0.80	4.10 ± 0.20 (19)	14500 ± 725 (19)	4.2 <sup>+0.5</sup> <sub>-0.5</sub>	180 (19)
EC 05490-4510	32 ± 10 (19)	-1.75 ± 1.34	2.83 ± 1.37	4.20 ± 0.20 (19)	17000 ± 850 (19)	5.1 <sup>+0.6</sup> <sub>-0.5</sub>	30 (19)
EC 10549-2953	-17 ± 10 (19)	-8.81 ± 1.09	1.03 ± 1.07	4.10 ± 0.20 (19)	14000 ± 700 (19)	4.0 <sup>+0.5</sup> <sub>-0.4</sub>	200 (19)
EC 19071-7643	-20 ± 10 (14)	16.66 ± 0.65	-20.15 ± 0.64	4.20 ± 0.20 (14)	21500 ± 2000 (14)	7.5 <sup>+1.5</sup> <sub>-1.2</sub>	30 (14)
EC 19476-4109	-19 ± 10 (14)	-3.70 ± 0.61	-4.51 ± 0.62	4.00 ± 0.20 (14)	17000 ± 2000 (14)	5.6 <sup>+1.2</sup> <sub>-1.1</sub>	120 (14)
EC 20292-2414	15 ± 10 (19)	1.36 ± 0.78	-11.32 ± 0.85	4.10 ± 0.20 (19)	25000 ± 1250 (19)	10.3 <sup>+1.4</sup> <sub>-1.3</sub>	160 (19)
EC 13139-1851	23 ± 10 (19)	-9.15 ± 1.39	-3.80 ± 1.52	4.20 ± 0.20 (19)	17000 ± 850 (19)	5.1 <sup>+0.6</sup> <sub>-0.6</sub>	50 (19)
EC 20140-6935	17 ± 10 (19)	8.81 ± 0.51	1.79 ± 0.62	3.70 ± 0.20 (19)	20500 ± 1025 (19)	8.8 <sup>+1.5</sup> <sub>-1.1</sub>	65 (19)
EC 09414-1325	71 ± 10 (19)	-2.36 ± 1.03	-1.47 ± 1.10	4.10 ± 0.20 (19)	14000 ± 700 (19)	3.9 <sup>+0.5</sup> <sub>-0.4</sub>	260 (19)
EC 03240-6229	-12 ± 10 (19)	3.27 ± 1.23	4.28 ± 1.28	3.80 ± 0.20 (19)	12000 ± 600 (19)	3.6 <sup>+0.5</sup> <sub>-0.4</sub>	165 (19)
EC 20153-6731	-40 ± 10 (19)	5.07 ± 1.07	-8.76 ± 1.00	3.80 ± 0.20 (19)	14500 ± 725 (19)	4.8 <sup>+0.7</sup> <sub>-0.6</sub>	120 (19)
EC 19586-3823	-102 ± 10 (14)	-0.13 ± 1.04	2.56 ± 1.03	3.90 ± 0.20 (14)	18500 ± 2000 (14)	6.7 <sup>+1.4</sup> <sub>-1.2</sub>	150 (14)
EC 06387-8045	60 ± 10 (19)	-0.99 ± 0.92	6.62 ± 0.94	3.90 ± 0.20 (19)	22500 ± 1125 (19)	9.5 <sup>+1.4</sup> <sub>-1.1</sub>	190 (19)
PG 1533+467	33 ± 6 (18)	-11.45 ± 0.53	11.41 ± 0.54	4.09 ± 0.10 (18)	18500 ± 925 (18)	6.0 <sup>+0.5</sup> <sub>-0.5</sub>	215 (18)
EC 20252-3137	26 ± 10 (14)	-6.08 ± 0.89	-3.59 ± 0.91	4.00 ± 0.20 (14)	23000 ± 2000 (14)	9.2 <sup>+1.9</sup> <sub>-1.5</sub>	60 (14)
EC 05438-4741	53 ± 10 (19)	-0.35 ± 1.07	-0.94 ± 1.53	4.10 ± 0.20 (19)	13500 ± 675 (19)	3.8 <sup>+0.5</sup> <sub>-0.4</sub>	30 (19)
EC 20104-2944	135 ± 10 (14)	-0.45 ± 1.70	-1.40 ± 1.98	4.20 ± 0.20 (14)	15000 ± 2000 (14)	4.2 <sup>+1.0</sup> <sub>-0.9</sub>	50 (14)
EC 05515-6107	89 ± 10 (19)	-5.82 ± 1.65	11.57 ± 1.43	4.00 ± 0.20 (19)	22000 ± 1100 (19)	8.6 <sup>+1.1</sup> <sub>-1.0</sub>	290 (19)
PG 1205+228	153 ± 4 (20)	-15.44 ± 0.55	0.05 ± 0.48	4.10 ± 0.20 (20)	16600 ± 1000 (20)	5.2 <sup>+0.7</sup> <sub>-0.6</sub>	165 (20)
EC 23169-2235	82 ± 10 (19)	4.24 ± 1.25	4.35 ± 1.18	4.40 ± 0.20 (19)	15000 ± 750 (19)	3.9 <sup>+0.5</sup> <sub>-0.4</sub>	140 (19)
EC 09452-1403	236 ± 10 (19)	-3.55 ± 1.54	-0.37 ± 1.71	4.30 ± 0.20 (19)	14000 ± 700 (19)	3.6 <sup>+0.4</sup> <sub>-0.4</sub>	70 (19)
PG 2345+241	80 ± 3 (20)	-2.22 ± 0.74	-3.09 ± 0.67	4.20 ± 0.20 (20)	18800 ± 1000 (20)	6.0 <sup>+0.7</sup> <sub>-0.7</sub>	54 (20)
PHL 159	88 ± 3 (18)	-3.02 ± 0.87	-9.38 ± 0.69	3.59 ± 0.10 (18)	18500 ± 925 (18)	7.9 <sup>+0.8</sup> <sub>-0.8</sub>	21 (18)
EC 10500-1358	99 ± 10 (19)	-4.00 ± 0.93	-2.17 ± 1.01	3.80 ± 0.20 (19)	15000 ± 750 (19)	5.1 <sup>+0.7</sup> <sub>-0.6</sub>	100 (19)
PG 1511+367	102 ± 11 (18)	-3.64 ± 0.88	-13.10 ± 0.87	4.15 ± 0.10 (18)	16100 ± 805 (18)	4.7 <sup>+0.4</sup> <sub>-0.4</sub>	77 (18)
EC 20011-5005	-171 ± 10 (14)	2.06 ± 1.61	-3.96 ± 1.83	4.20 ± 0.20 (14)	17000 ± 2000 (14)	5.1 <sup>+1.1</sup> <sub>-1.0</sub>	30 (14)

Continued on next page

Table A.1 – continued from previous page

Name	r.v. (km s <sup>-1</sup> )	p.m. $\alpha \cos \delta$ (mas yr <sup>-1</sup> )	p.m. $\delta$ (mas yr <sup>-1</sup> )	log $g$ (cm s <sup>-2</sup> )	$T_{\text{eff}}$ (K)	Mass (M <sub>⊙</sub> )	$v \sin i$ (km s <sup>-1</sup> )
BD -15 115	93 ± 4 (18)	7.04 ± 1.00	0.46 ± 0.76	3.81 ± 0.10 (18)	20100 ± 1005 (18)	8.0 <sup>+0.8</sup> <sub>-0.8</sub>	35 (18)
PG 2219+094	-24 ± 9 (18)	-3.53 ± 1.17	-8.43 ± 1.16	3.58 ± 0.10 (18)	19500 ± 975 (18)	8.1 <sup>+0.8</sup> <sub>-0.8</sub>	225 (20)
HS 1914+7139	-39 ± 10 (6)	-0.66 ± 1.86	-0.14 ± 2.60	3.90 ± 0.10 (18)	17600 ± 880 (18)	6.1 <sup>+0.5</sup> <sub>-0.5</sub>	250 (18)
PG 0855+294	65 ± 4 (20)	5.86 ± 0.79	-3.98 ± 0.82	3.80 ± 0.20 (20)	18100 ± 1000 (20)	6.8 <sup>+1.0</sup> <sub>-0.8</sub>	110 (20)
PG 0955+291	76 ± 14 (20)	-7.84 ± 0.96	-4.27 ± 1.14	3.80 ± 0.20 (20)	13600 ± 1000 (20)	4.3 <sup>+0.6</sup> <sub>-0.5</sub>	190 (20)
PG 2229+099	-22 ± 5 (20)	-1.22 ± 1.85	-0.98 ± 2.35	4.00 ± 0.20 (20)	17600 ± 1000 (20)	5.9 <sup>+0.8</sup> <sub>-0.7</sub>	16 (20)
PG 1610+239	91 ± 10 (18)	-0.20 ± 2.80	-5.20 ± 1.80	3.72 ± 0.10 (18)	15500 ± 775 (18)	5.6 <sup>+0.5</sup> <sub>-0.5</sub>	75 (18)
PG 2111+023	-153 ± 11 (12)	-6.98 ± 1.76	-4.07 ± 0.97	3.40 ± 0.10 (12)	14000 ± 700 (12)	5.2 <sup>+0.4</sup> <sub>-0.4</sub>	140 (12)
PG 0009+036	142 ± 18 (20)	-0.99 ± 1.88	1.43 ± 2.34	3.60 ± 0.20 (20)	14800 ± 1000 (20)	5.2 <sup>+0.7</sup> <sub>-0.6</sub>	350 (20)
PG 0122+214	26 ± 5 (18)	-1.10 ± 0.58	-3.23 ± 0.84	3.86 ± 0.10 (18)	18300 ± 915 (18)	6.5 <sup>+0.6</sup> <sub>-0.6</sub>	117 (18)
SB 357	58 ± 10 (18)	0.25 ± 1.27	-2.81 ± 1.57	3.90 ± 0.10 (18)	19700 ± 993 (18)	7.4 <sup>+0.7</sup> <sub>-0.6</sub>	180 (18)
EC 04420 -1908	205 ± 10 (14)	-1.27 ± 1.81	-1.65 ± 2.23	3.40 ± 0.20 (14)	14000 ± 2000 (14)	5.5 <sup>+1.3</sup> <sub>-1.1</sub>	180 (14)
PG 1332+137	148 ± 10 (17)	-5.99 ± 0.77	-7.47 ± 0.72	3.50 ± 0.20 (12)	15000 ± 750 (12)	5.9 <sup>+0.8</sup> <sub>-0.7</sub>	140 (12)
EC 19596-5356	200 ± 15 (13)	1.22 ± 1.95	-0.52 ± 2.47	3.75 ± 0.20 (13)	16500 ± 1500 (13)	5.9 <sup>+1.0</sup> <sub>-0.9</sub>	250 (13)
PHL 346	63 ± 4 (18)	4.12 ± 1.23	-7.94 ± 1.17	3.58 ± 0.10 (18)	20700 ± 1035 (18)	9.6 <sup>+1.2</sup> <sub>-1.0</sub>	45 (18)
PG 0914+001	90 ± 20 (20)	1.15 ± 1.80	1.64 ± 2.72	3.10 ± 0.20 (20)	12300 ± 1000 (20)	5.3 <sup>+0.8</sup> <sub>-0.7</sub>	325 (20)
PG 1209+263	52 ± 11 (12)	0.40 ± 1.92	-0.74 ± 2.38	3.00 ± 0.20 (12)	12000 ± 600 (12)	5.5 <sup>+0.8</sup> <sub>-0.8</sub>	70 (12)

References: (1) this study, from Strömgren  $uvby\beta$  photometry; (2) Behr (2003b); (3) Conlon et al. (1989); (4) Conlon et al. (1992); (5) Evans (1967); (6) Heber et al. (1995); (7) Keenan et al. (1982); (8) Keenan and Dufton (1983); (9) Keenan et al. (1986); (10) Kilkenney (1992); (11) Levenhagen and Leister (2006); (12) Lynn et al. (2004a); (13) Lynn et al. (2004b); (14) Magee et al. (2001); (15) Martin (2003); (16) Martin (2004); (17) Martin (2006); (18) Ramspeck et al. (2001b); (19) Rolleston et al. (1997); (20) Rolleston et al. (1999).

Table A.2: Input data for stars belonging to group B. The data shown are: the radial velocity, the proper motions in right ascension and declination directions, the surface gravity, temperature, mass and projected rotation velocity.

Name	r.v. (km s <sup>-1</sup> )	p.m. $\alpha \cos \delta$ (mas yr <sup>-1</sup> )	p.m. $\delta$ (mas yr <sup>-1</sup> )	log $g$ (cm s <sup>-2</sup> )	$T_{\text{eff}}$ (K)	Mass (M <sub>⊙</sub> )	$v \sin i$ (km s <sup>-1</sup> )
HIP 81153	146 ± 7 (17)	-8.64 ± 0.65	-13.35 ± 0.65	4.05 ± 0.45 (16)	29891 ± 684 (16)	15.4 <sup>+7.1</sup> <sub>-3.1</sub>	80 (16)
HIP 1241	0 ± 5 (17)	5.98 ± 0.63	-0.43 ± 0.49	3.98 ± 0.15 (1)	11489 ± 574 (1)	3.1 <sup>+0.3</sup> <sub>-0.3</sub>	130 (16)
HIP 28132	54 ± 3 (17)	-3.90 ± 0.65	8.35 ± 0.71	4.00 ± 0.15 (16)	16948 ± 140 (16)	5.5 <sup>+0.4</sup> <sub>-0.3</sub>	100 (16)
HIP 2702	-26 ± 10 (14)	-5.23 ± 0.56	-5.77 ± 0.57	4.20 ± 0.20 (14)	15500 ± 2000 (14)	4.4 <sup>+1.1</sup> <sub>-0.9</sub>	30 (14)
HIP 55051	20 ± 10 (8)	28.82 ± 0.50	20.03 ± 0.41	4.06 ± 0.25 (1)	25518 ± 1276 (1)	10.7 <sup>+1.8</sup> <sub>-1.5</sub>	150 (11)
HIP 114690	83 ± 7 (7)	4.98 ± 0.71	-12.56 ± 0.51	3.50 ± 0.25 (9)	20008 ± 1000 (1)	9.3 <sup>+1.9</sup> <sub>-1.4</sub>	238 (7)
HIP 11844	-45 ± 6 (17)	6.13 ± 0.90	-2.76 ± 0.95	4.14 ± 0.08 (16)	11202 ± 68 (16)	2.9 <sup>+0.1</sup> <sub>-0.1</sub>	130 (16)
HIP 16130	28 ± 6 (17)	8.65 ± 0.63	2.59 ± 0.70	4.11 ± 0.15 (1)	14061 ± 703 (1)	4.0 <sup>+0.1</sup> <sub>-0.4</sub>	60 (16)
HIP 58046	20 ± 2 (17)	8.12 ± 0.83	6.73 ± 0.82	4.25 ± 0.25 (16)	13357 ± 668 (16)	3.5 <sup>+0.5</sup> <sub>-0.4</sub>	230 (16)
BD +36 2242	2 ± 4 (2)	-5.92 ± 0.52	1.68 ± 0.50	3.87 ± 0.15 (1)	11806 ± 590 (1)	3.4 <sup>+0.4</sup> <sub>-0.3</sub>	77 (2)
HIP 98136	29 ± 6 (17)	-3.78 ± 0.72	-10.84 ± 0.56	3.42 ± 0.20 (1)	21570 ± 1079 (1)	11.6 <sup>+2.3</sup> <sub>-1.7</sub>	140 (16)
HIP 111396	-33 ± 6 (17)	-0.76 ± 0.62	2.89 ± 0.62	3.62 ± 0.15 (1)	13662 ± 683 (1)	4.9 <sup>+0.5</sup> <sub>-0.5</sub>	35 (16)
HIP 77131	-9 ± 5 (5)	-4.59 ± 0.75	-1.76 ± 0.71	3.86 ± 0.25 (16)	32089 ± 536 (16)	19.5 <sup>+5.5</sup> <sub>-2.7</sub>	250 (16)
HIP 113735	-31 ± 10 (9)	10.12 ± 0.49	18.42 ± 0.49	4.12 ± 0.20 (1)	21645 ± 1082 (1)	7.9 <sup>+1.0</sup> <sub>-0.9</sub>	?
HIP 59955	28 ± 10 (17)	-10.82 ± 0.72	-2.41 ± 0.59	3.66 ± 0.15 (1)	13860 ± 693 (1)	4.7 <sup>+0.5</sup> <sub>-0.4</sub>	225 (16)
HIP 76161	-51 ± 7 (15)	0.61 ± 0.76	-0.39 ± 0.71	3.43 ± 0.20 (1)	22331 ± 1117 (1)	12.7 <sup>+3.0</sup> <sub>-2.0</sub>	?
HIP 96130	-51 ± 6 (17)	1.32 ± 0.72	-0.04 ± 0.58	3.63 ± 0.21 (16)	23141 ± 239 (16)	11.8 <sup>+2.0</sup> <sub>-1.6</sub>	60 (16)
HIP 61800	-48 ± 13 (17)	0.07 ± 0.45	-5.11 ± 0.43	3.24 ± 0.15 (1)	12247 ± 612 (1)	4.8 <sup>+0.6</sup> <sub>-0.5</sub>	150 (16)
HIP 114569	94 ± 5 (17)	46.35 ± 0.79	32.73 ± 0.74	4.12 ± 0.15 (1)	18518 ± 926 (1)	6.1 <sup>+0.2</sup> <sub>-0.6</sub>	70 (16)
HIP 11809	0 ± 10 (17)	-18.90 ± 0.88	-13.46 ± 0.87	4.25 ± 0.25 (16)	13265 ± 663 (16)	3.5 <sup>+0.5</sup> <sub>-0.4</sub>	240 (16)
HIP 16758	98 ± 10 (14)	7.37 ± 0.48	10.04 ± 0.53	3.60 ± 0.20 (14)	23453 ± 1173 (1)	12.1 <sup>+2.5</sup> <sub>-1.8</sub>	90 (14)
HIP 108215	-79 ± 7 (7)	8.23 ± 0.59	-8.49 ± 0.38	3.06 ± 0.15 (1)	13996 ± 700 (1)	7.0 <sup>+1.2</sup> <sub>-0.9</sub>	169 (7)
HIP 115347	23 ± 7 (7)	-6.30 ± 0.59	-7.01 ± 0.46	3.49 ± 0.20 (1)	21106 ± 1055 (1)	10.6 <sup>+2.0</sup> <sub>-1.6</sub>	27 (7)
HIP 115729	26 ± 3 (17)	3.05 ± 0.72	-1.21 ± 0.61	3.46 ± 0.15 (1)	17966 ± 898 (1)	7.8 <sup>+1.1</sup> <sub>-0.9</sub>	25 (16)
HIP 3812	19 ± 10 (14)	0.80 ± 0.70	-1.73 ± 0.73	4.00 ± 0.20 (14)	19000 ± 2000 (14)	6.7 <sup>+1.3</sup> <sub>-1.2</sub>	219 (7)
PG 1530+212	-7 ± 25 (2)	4.04 ± 0.52	6.60 ± 0.53	4.00 ± 0.25 (2)	15000 ± 500 (2)	4.6 <sup>+0.7</sup> <sub>-0.5</sub>	104 (12)
HIP 79649	19 ± 6 (17)	-0.48 ± 0.57	-2.97 ± 0.62	3.69 ± 0.20 (1)	21721 ± 1086 (1)	9.8 <sup>+1.7</sup> <sub>-1.3</sub>	90 (16)
HIP 12320	24 ± 12 (17)	4.33 ± 0.84	-1.25 ± 0.92	4.00 ± 0.25 (16)	13382 ± 669 (16)	3.9 <sup>+0.6</sup> <sub>-0.5</sub>	225 (16)
HIP 109051	72 ± 8 (17)	1.43 ± 0.72	-0.88 ± 0.74	3.85 ± 0.20 (1)	21021 ± 1051 (1)	8.2 <sup>+1.3</sup> <sub>-1.0</sub>	105 (16)
HIP 111563	42 ± 7 (7)	5.13 ± 0.47	-17.86 ± 0.36	3.11 ± 0.20 (1)	22545 ± 1127 (1)	17.3 <sup>+6.0</sup> <sub>-3.6</sub>	105 (7)
HIP 13800	-6 ± 2 (2)	4.69 ± 0.68	-3.63 ± 0.80	3.67 ± 0.15 (1)	16632 ± 832 (1)	6.3 <sup>+0.7</sup> <sub>-0.7</sub>	12 (2)

Continued on next page

Table A.2 – continued from previous page

Name	r.v. (km s <sup>-1</sup> )	p.m. $\alpha \cos \delta$ (mas yr <sup>-1</sup> )	p.m. $\delta$ (mas yr <sup>-1</sup> )	log $g$ (cm s <sup>-2</sup> )	$T_{\text{eff}}$ (K)	Mass (M <sub>⊙</sub> )	$v \sin i$ (km s <sup>-1</sup> )
HIP 48394	14 ± 12 (17)	3.34 ± 0.93	-5.69 ± 0.72	3.75 ± 0.25 (16)	20021 ± 1001 (16)	7.8 <sup>+1.4</sup> <sub>-1.0</sub>	225 (16)
HIP 107027	117 ± 8 (17)	-6.18 ± 0.77	-11.99 ± 0.64	3.65 ± 0.21 (16)	21959 ± 231 (16)	10.5 <sup>+1.8</sup> <sub>-1.3</sub>	150 (16)
HIP 1904	-37 ± 10 (9)	2.95 ± 0.47	-6.27 ± 0.49	3.03 ± 0.15 (1)	12894 ± 645 (1)	6.8 <sup>+1.2</sup> <sub>-0.9</sub>	?
HIP 55461	72 ± 6 (17)	-0.97 ± 0.74	-5.36 ± 0.69	4.00 ± 0.20 (3)	15600 ± 1000 (3)	4.9 <sup>+0.7</sup> <sub>-0.6</sub>	140 (16)
HIP 112790	15 ± 4 (17)	-18.34 ± 0.67	-13.53 ± 0.69	3.53 ± 0.15 (1)	15628 ± 781 (1)	5.9 <sup>+0.4</sup> <sub>-0.5</sub>	70 (16)
HIP 59067	35 ± 5 (17)	-8.47 ± 0.83	-5.87 ± 0.70	3.89 ± 0.15 (16)	14974 ± 98 (16)	4.8 <sup>+0.4</sup> <sub>-0.3</sub>	70 (16)
BD +20 3004	22 ± 14 (2)	-10.91 ± 0.51	5.28 ± 0.55	3.40 ± 0.15 (1)	14070 ± 704 (1)	5.6 <sup>+0.8</sup> <sub>-0.6</sub>	105 (2)
HIP 105912	-17 ± 7 (7)	10.16 ± 0.57	-11.61 ± 0.47	3.29 ± 0.20 (1)	22201 ± 1110 (1)	13.6 <sup>+3.5</sup> <sub>-2.4</sub>	102 (7)
HIP 45904	36 ± 14 (17)	3.27 ± 0.79	-9.63 ± 0.60	3.48 ± 0.20 (1)	21016 ± 1051 (1)	10.7 <sup>+2.0</sup> <sub>-1.5</sub>	277 (12)
HIP 37903	84 ± 10 (17)	2.32 ± 0.83	-5.77 ± 0.76	3.00 ± 0.25 (16)	18000 ± 900 (16)	10.8 <sup>+3.3</sup> <sub>-2.2</sub>	150 (16)
HIP 70275	241 ± 6 (2)	4.24 ± 0.69	-10.74 ± 0.64	3.64 ± 0.20 (1)	22790 ± 1140 (1)	11.3 <sup>+2.1</sup> <sub>-1.6</sub>	68 (2)
BD -2 3766	41 ± 10 (4)	1.77 ± 0.59	17.26 ± 0.62	3.70 ± 0.20 (4)	22000 ± 1000 (4)	10.1 <sup>+1.7</sup> <sub>-1.3</sub>	200 (16)
PB 5418	152 ± 10 (4)	8.25 ± 1.48	-4.74 ± 1.63	4.00 ± 0.20 (4)	19310 ± 966 (1)	6.8 <sup>+0.9</sup> <sub>-0.8</sub>	150 (10)
HIP 56322	254 ± 9 (17)	3.54 ± 0.73	11.52 ± 0.69	3.57 ± 0.25 (1)	25501 ± 1275 (1)	14.2 <sup>+4.2</sup> <sub>-2.5</sub>	160 (16)
Ton S 308	89 ± 10 (4)	-0.38 ± 1.57	-0.96 ± 1.76	4.00 ± 0.20 (4)	17821 ± 891 (1)	6.0 <sup>+0.8</sup> <sub>-0.7</sub>	120 (4)
PHL 2018	108 ± 10 (4)	3.87 ± 1.19	-11.27 ± 1.17	3.70 ± 0.20 (4)	19095 ± 955 (1)	7.7 <sup>+1.1</sup> <sub>-0.9</sub>	150 (4)
HIP 52906	84 ± 11 (17)	-7.39 ± 0.61	1.34 ± 0.60	3.39 ± 0.15 (1)	18898 ± 945 (1)	9.0 <sup>+1.2</sup> <sub>-1.0</sub>	160 (16)

References: (1) this study, from Strömberg *uvby* photometry; (2) Behr (2003b); (3) Conlon et al. (1989); (4) Conlon et al. (1992); (5) Evans (1967); (6) Heber et al. (1995); (7) Keenan et al. (1982); (8) Keenan and Dufton (1983); (9) Keenan et al. (1986); (10) Kilkeny (1992); (11) Levenhagen and Leister (2006); (12) Lynn et al. (2004a); (13) Lynn et al. (2004b); (14) Magee et al. (2001); (15) Martin (2003); (16) Martin (2004); (17) Martin (2006); (18) Ramspeck et al. (2001b); (19) Rolleston et al. (1997); (20) Rolleston et al. (1999).

Table A.3: Computed values for stars belonging to group A. The values shown are: the present coordinates of the star ( $X, Y, Z$ ) (in galactocentric Cartesian coordinates), the distance, the evolutionary age, the flight time, the ejection velocity and the coordinates ( $X_0, Y_0$ ) of the point of ejection in the galactic plane.

Name	$X$ (kpc)	$Y$ (kpc)	$Z$ (kpc)	$d$ (kpc)	Age (Myr)	$t_{\text{flight}}$ (Myr)	$v_{\text{ejec}}$ (km s $^{-1}$ )	$X_0$ (kpc)	$Y_0$ (kpc)
EC 19337-6743	-7.60 <sup>+0.20</sup> <sub>-0.10</sub>	-0.30 <sup>+0.10</sup> <sub>-0.10</sub>	-0.30 <sup>+0.10</sup> <sub>-0.10</sub>	0.56 <sup>+0.30</sup> <sub>-0.22</sub>	223.2 <sup>+314.4</sup> <sub>-132.0</sub>	21.0 <sup>+5.8</sup> <sub>-3.8</sub>	28 <sup>+11</sup> <sub>-8</sub>	-5.57 <sup>+0.83</sup> <sub>-0.62</sub>	-4.72 <sup>+0.74</sup> <sub>-1.05</sub>
EC 05515-6231	-8.00 <sup>+0.00</sup> <sub>-0.00</sub>	-0.60 <sup>+0.20</sup> <sub>-0.20</sub>	-0.40 <sup>+0.10</sup> <sub>-0.10</sub>	0.71 <sup>+0.29</sup> <sub>-0.22</sub>	36.7 <sup>+68.1</sup> <sub>-36.7</sub>	31.0 <sup>+5.0</sup> <sub>-4.7</sub>	35 <sup>+10</sup> <sub>-9</sub>	-4.78 <sup>+0.94</sup> <sub>-0.80</sub>	-7.03 <sup>+0.94</sup> <sub>-0.95</sub>
EC 20089-5659	-7.40 <sup>+0.30</sup> <sub>-0.20</sub>	-0.20 <sup>+0.00</sup> <sub>-0.10</sub>	-0.40 <sup>+0.10</sup> <sub>-0.20</sub>	0.81 <sup>+0.35</sup> <sub>-0.25</sub>	83.6 <sup>+65.7</sup> <sub>-37.1</sub>	25.9 <sup>+4.7</sup> <sub>-3.0</sub>	53 <sup>+21</sup> <sub>-14</sub>	-4.21 <sup>+0.77</sup> <sub>-0.74</sub>	-4.90 <sup>+0.58</sup> <sub>-0.67</sub>
EC 03462-5813	-8.00 <sup>+0.00</sup> <sub>-0.00</sub>	-0.60 <sup>+0.20</sup> <sub>-0.20</sub>	-0.60 <sup>+0.10</sup> <sub>-0.20</sub>	0.83 <sup>+0.27</sup> <sub>-0.21</sub>	1.8 <sup>+75.3</sup> <sub>-1.8</sub>	12.2 <sup>+2.2</sup> <sub>-2.1</sub>	79 <sup>+20</sup> <sub>-16</sub>	-6.59 <sup>+0.67</sup> <sub>-0.50</sub>	-3.20 <sup>+0.63</sup> <sub>-0.66</sub>
EC 05582-5816	-8.10 <sup>+0.10</sup> <sub>-0.00</sub>	-1.10 <sup>+0.20</sup> <sub>-0.40</sub>	-0.60 <sup>+0.10</sup> <sub>-0.30</sub>	1.31 <sup>+0.43</sup> <sub>-0.33</sub>	29.0 <sup>+13.4</sup> <sub>-28.4</sub>	35.8 <sup>+6.4</sup> <sub>-7.4</sub>	162 <sup>+24</sup> <sub>-24</sub>	-2.02 <sup>+2.27</sup> <sub>-2.25</sub>	-3.80 <sup>+0.52</sup> <sub>-0.39</sub>
EC 10087-1411	-8.20 <sup>+0.00</sup> <sub>-0.10</sub>	-0.90 <sup>+0.20</sup> <sub>-0.30</sub>	0.60 <sup>+0.20</sup> <sub>-0.10</sub>	1.10 <sup>+0.36</sup> <sub>-0.27</sub>	32.7 <sup>+37.8</sup> <sub>-32.7</sub>	18.7 <sup>+9.7</sup> <sub>-6.9</sub>	141 <sup>+35</sup> <sub>-22</sub>	-6.48 <sup>+1.85</sup> <sub>-0.91</sub>	-2.84 <sup>+0.79</sup> <sub>-0.64</sub>
EC 05490-4510	-8.50 <sup>+0.10</sup> <sub>-0.10</sub>	-1.40 <sup>+0.30</sup> <sub>-0.50</sub>	-0.80 <sup>+0.20</sup> <sub>-0.30</sub>	1.74 <sup>+0.56</sup> <sub>-0.43</sub>	18.3 <sup>+24.7</sup> <sub>-18.2</sub>	23.7 <sup>+7.1</sup> <sub>-4.7</sub>	51 <sup>+10</sup> <sub>-8</sub>	-6.47 <sup>+1.09</sup> <sub>-0.64</sub>	-6.03 <sup>+1.09</sup> <sub>-1.33</sub>
EC 10549-2953	-7.90 <sup>+0.10</sup> <sub>-0.00</sub>	-1.50 <sup>+0.50</sup> <sub>-0.30</sub>	0.80 <sup>+0.20</sup> <sub>-0.20</sub>	1.71 <sup>+0.55</sup> <sub>-0.42</sub>	36.4 <sup>+42.7</sup> <sub>-36.4</sub>	42.9 <sup>+8.9</sup> <sub>-7.2</sub>	56 <sup>+14</sup> <sub>-11</sub>	-0.81 <sup>+2.48</sup> <sub>-1.95</sub>	-7.86 <sup>+0.63</sup> <sub>-0.64</sub>
EC 19071-7643	-6.70 <sup>+0.50</sup> <sub>-0.30</sub>	-1.20 <sup>+0.30</sup> <sub>-0.40</sub>	-0.90 <sup>+0.20</sup> <sub>-0.40</sub>	2.03 <sup>+0.75</sup> <sub>-0.56</sub>	6.2 <sup>+12.7</sup> <sub>-6.2</sub>	6.6 <sup>+0.5</sup> <sub>-0.3</sub>	226 <sup>+82</sup> <sub>-63</sub>	-5.21 <sup>+0.91</sup> <sub>-0.68</sub>	-2.18 <sup>+0.15</sup> <sub>-0.18</sub>
EC 19476-4109	-6.30 <sup>+0.70</sup> <sub>-0.50</sub>	0.00 <sup>+0.00</sup> <sub>-0.10</sub>	-0.90 <sup>+0.20</sup> <sub>-0.40</sub>	1.93 <sup>+0.77</sup> <sub>-0.55</sub>	37.1 <sup>+27.0</sup> <sub>-22.1</sub>	34.3 <sup>+2.0</sup> <sub>-2.1</sub>	111 <sup>+44</sup> <sub>-31</sub>	-1.98 <sup>+0.75</sup> <sub>-0.82</sub>	-4.61 <sup>+0.83</sup> <sub>-0.64</sub>
EC 20292-2414	-6.40 <sup>+0.50</sup> <sub>-0.40</sub>	0.60 <sup>+0.20</sup> <sub>-0.20</sub>	-1.00 <sup>+0.20</sup> <sub>-0.40</sub>	1.97 <sup>+0.67</sup> <sub>-0.49</sub>	7.4 <sup>+4.6</sup> <sub>-7.4</sub>	16.2 <sup>+1.6</sup> <sub>-1.5</sub>	131 <sup>+49</sup> <sub>-36</sub>	-5.92 <sup>+0.59</sup> <sub>-0.49</sub>	-1.55 <sup>+0.67</sup> <sub>-0.51</sub>
EC 13139-1851	-7.20 <sup>+0.30</sup> <sub>-0.20</sub>	-0.90 <sup>+0.20</sup> <sub>-0.30</sub>	1.10 <sup>+0.40</sup> <sub>-0.30</sub>	1.65 <sup>+0.54</sup> <sub>-0.41</sub>	18.7 <sup>+24.5</sup> <sub>-18.7</sub>	26.1 <sup>+4.5</sup> <sub>-4.5</sub>	122 <sup>+45</sup> <sub>-32</sub>	-4.14 <sup>+1.51</sup> <sub>-1.28</sub>	-4.03 <sup>+0.44</sup> <sub>-0.44</sub>
EC 20140-6935	-6.50 <sup>+0.50</sup> <sub>-0.40</sub>	-1.00 <sup>+0.20</sup> <sub>-0.40</sub>	-1.20 <sup>+0.30</sup> <sub>-0.40</sub>	2.14 <sup>+0.79</sup> <sub>-0.55</sub>	22.4 <sup>+4.9</sup> <sub>-4.9</sub>	12.0 <sup>+0.8</sup> <sub>-0.8</sub>	114 <sup>+40</sup> <sub>-27</sub>	-5.76 <sup>+0.76</sup> <sub>-0.56</sub>	-3.90 <sup>+0.45</sup> <sub>-0.52</sub>
EC 09414-1325	-8.90 <sup>+0.20</sup> <sub>-0.30</sub>	-2.30 <sup>+0.60</sup> <sub>-0.70</sub>	1.30 <sup>+0.50</sup> <sub>-0.30</sub>	2.78 <sup>+0.91</sup> <sub>-0.70</sub>	1.2 <sup>+61.6</sup> <sub>-1.2</sub>	35.7 <sup>+14.4</sup> <sub>-10.2</sub>	105 <sup>+27</sup> <sub>-18</sub>	-5.01 <sup>+2.54</sup> <sub>-1.47</sub>	-6.14 <sup>+1.02</sup> <sub>-0.94</sub>
EC 03240-6229	-7.80 <sup>+0.10</sup> <sub>-0.00</sub>	-1.40 <sup>+0.30</sup> <sub>-0.50</sub>	-1.50 <sup>+0.40</sup> <sub>-0.60</sub>	2.12 <sup>+0.73</sup> <sub>-0.54</sub>	140.0 <sup>+33.7</sup> <sub>-31.7</sub>	45.5 <sup>+7.2</sup> <sub>-6.4</sub>	76 <sup>+16</sup> <sub>-13</sub>	-0.98 <sup>+1.73</sup> <sub>-1.51</sub>	-8.39 <sup>+0.72</sup> <sub>-0.81</sub>
EC 20153-6731	-6.10 <sup>+0.70</sup> <sub>-0.50</sub>	-1.20 <sup>+0.30</sup> <sub>-0.40</sub>	-1.50 <sup>+0.40</sup> <sub>-0.50</sub>	2.71 <sup>+0.96</sup> <sub>-0.68</sub>	77.7 <sup>+17.9</sup> <sub>-15.4</sub>	23.1 <sup>+2.8</sup> <sub>-2.4</sub>	154 <sup>+50</sup> <sub>-38</sub>	-1.52 <sup>+1.01</sup> <sub>-0.92</sub>	-3.72 <sup>+0.66</sup> <sub>-0.59</sub>
EC 19586-3823	-5.30 <sup>+1.10</sup> <sub>-0.70</sub>	0.10 <sup>+0.10</sup> <sub>-0.80</sub>	-1.60 <sup>+0.50</sup> <sub>-0.60</sub>	3.20 <sup>+1.25</sup> <sub>-0.91</sub>	30.3 <sup>+16.8</sup> <sub>-11.9</sub>	39.1 <sup>+5.5</sup> <sub>-5.0</sub>	153 <sup>+34</sup> <sub>-23</sub>	1.93 <sup>+0.83</sup> <sub>-0.75</sub>	-6.74 <sup>+0.73</sup> <sub>-1.00</sub>
EC 06387-8045	-6.70 <sup>+0.40</sup> <sub>-0.30</sub>	-3.10 <sup>+0.80</sup> <sub>-1.10</sub>	-1.70 <sup>+0.40</sup> <sub>-0.60</sub>	3.75 <sup>+1.29</sup> <sub>-0.94</sub>	12.4 <sup>+3.9</sup> <sub>-9.0</sub>	24.4 <sup>+5.0</sup> <sub>-4.0</sub>	134 <sup>+17</sup> <sub>-18</sub>	-3.10 <sup>+1.96</sup> <sub>-1.47</sub>	-5.25 <sup>+0.56</sup> <sub>-0.65</sub>
PG 1533+467	-7.70 <sup>+0.00</sup> <sub>-0.00</sub>	1.30 <sup>+0.20</sup> <sub>-0.20</sub>	1.80 <sup>+0.30</sup> <sub>-0.30</sub>	2.23 <sup>+0.34</sup> <sub>-0.33</sub>	0.3 <sup>+9.6</sup> <sub>-0.3</sub>	16.1 <sup>+1.0</sup> <sub>-0.9</sub>	213 <sup>+38</sup> <sub>-30</sub>	-4.32 <sup>+0.77</sup> <sub>-0.65</sub>	-2.30 <sup>+0.19</sup> <sub>-0.17</sub>
EC 20252-3137	-5.40 <sup>+1.00</sup> <sub>-0.70</sub>	0.50 <sup>+0.20</sup> <sub>-0.10</sub>	-1.80 <sup>+0.50</sup> <sub>-0.60</sub>	3.21 <sup>+1.24</sup> <sub>-0.86</sub>	12.5 <sup>+6.5</sup> <sub>-8.4</sub>	45.7 <sup>+7.5</sup> <sub>-5.7</sub>	155 <sup>+59</sup> <sub>-43</sub>	-2.77 <sup>+0.65</sup> <sub>-0.84</sub>	-4.95 <sup>+0.98</sup> <sub>-0.80</sub>
EC 05438-4741	-8.90 <sup>+0.30</sup> <sub>-0.20</sub>	-3.10 <sup>+0.80</sup> <sub>-1.00</sub>	-1.90 <sup>+0.50</sup> <sub>-0.60</sub>	3.67 <sup>+1.26</sup> <sub>-0.91</sub>	82.1 <sup>+32.3</sup> <sub>-80.4</sub>	35.5 <sup>+13.3</sup> <sub>-8.4</sub>	100 <sup>+24</sup> <sub>-18</sub>	-6.82 <sup>+1.79</sup> <sub>-1.19</sub>	-8.07 <sup>+1.39</sup> <sub>-1.62</sub>
EC 20104-2944	-4.70 <sup>+1.30</sup> <sub>-1.00</sub>	0.70 <sup>+0.30</sup> <sub>-0.20</sub>	-1.90 <sup>+0.50</sup> <sub>-0.80</sub>	3.90 <sup>+1.59</sup> <sub>-1.14</sub>	26.7 <sup>+51.2</sup> <sub>-26.7</sub>	17.9 <sup>+5.4</sup> <sub>-3.8</sub>	172 <sup>+49</sup> <sub>-23</sub>	-5.87 <sup>+1.34</sup> <sub>-0.99</sub>	-3.15 <sup>+0.94</sup> <sub>-1.29</sub>
EC 05515-6107	-8.00 <sup>+0.00</sup> <sub>-0.00</sub>	-3.40 <sup>+0.80</sup> <sub>-1.20</sub>	-2.00 <sup>+0.50</sup> <sub>-0.70</sub>	4.01 <sup>+1.33</sup> <sub>-1.00</sub>	4.2 <sup>+9.2</sup> <sub>-4.2</sub>	13.9 <sup>+3.2</sup> <sub>-2.3</sub>	188 <sup>+65</sup> <sub>-39</sub>	-4.51 <sup>+1.84</sup> <sub>-1.17</sub>	-6.02 <sup>+1.24</sup> <sub>-1.59</sub>
PG 1205+228	-8.20 <sup>+0.00</sup> <sub>-0.10</sub>	-0.30 <sup>+0.00</sup> <sub>-0.20</sub>	2.20 <sup>+0.70</sup> <sub>-0.60</sub>	2.22 <sup>+0.76</sup> <sub>-0.56</sub>	18.2 <sup>+24.5</sup> <sub>-18.2</sub>	14.4 <sup>+4.5</sup> <sub>-3.7</sub>	254 <sup>+60</sup> <sub>-40</sub>	-5.42 <sup>+2.01</sup> <sub>-1.18</sub>	-2.06 <sup>+0.28</sup> <sub>-0.17</sub>
EC 23169-2235	-7.30 <sup>+0.20</sup> <sub>-0.20</sub>	0.60 <sup>+0.20</sup> <sub>-0.20</sub>	-2.30 <sup>+0.60</sup> <sub>-0.70</sub>	2.47 <sup>+0.82</sup> <sub>-0.61</sub>	0.0 <sup>+33.3</sup> <sub>-0.0</sub>	20.4 <sup>+3.9</sup> <sub>-3.5</sub>	151 <sup>+34</sup> <sub>-24</sub>	-5.39 <sup>+1.27</sup> <sub>-0.95</sub>	-4.80 <sup>+0.86</sup> <sub>-1.02</sub>
EC 09452-1403	-9.50 <sup>+0.40</sup> <sub>-0.40</sub>	-4.00 <sup>+1.00</sup> <sub>-1.30</sub>	2.40 <sup>+0.80</sup> <sub>-0.60</sub>	4.89 <sup>+1.61</sup> <sub>-1.20</sub>	1.4 <sup>+72.1</sup> <sub>-1.4</sub>	26.1 <sup>+13.5</sup> <sub>-8.7</sub>	272 <sup>+62</sup> <sub>-31</sub>	-4.85 <sup>+3.82</sup> <sub>-1.90</sub>	-3.27 <sup>+1.07</sup> <sub>-1.22</sub>
PG 2345+241	-9.00 <sup>+0.20</sup> <sub>-0.40</sub>	3.80 <sup>+1.30</sup> <sub>-0.90</sub>	-2.90 <sup>+0.70</sup> <sub>-1.00</sub>	4.93 <sup>+1.65</sup> <sub>-1.25</sub>	11.2 <sup>+18.5</sup> <sub>-11.2</sub>	26.7 <sup>+5.4</sup> <sub>-4.4</sub>	149 <sup>+20</sup> <sub>-17</sub>	-9.27 <sup>+0.79</sup> <sub>-1.30</sub>	-3.80 <sup>+0.93</sup> <sub>-1.14</sub>
PHL 159	-6.00 <sup>+0.40</sup> <sub>-0.30</sub>	3.30 <sup>+0.60</sup> <sub>-0.50</sub>	-3.00 <sup>+0.50</sup> <sub>-0.50</sub>	4.87 <sup>+0.88</sup> <sub>-0.74</sub>	31.5 <sup>+6.4</sup> <sub>-5.3</sub>	21.4 <sup>+3.0</sup> <sub>-2.4</sub>	188 <sup>+25</sup> <sub>-20</sub>	-9.32 <sup>+0.63</sup> <sub>-0.92</sub>	-0.07 <sup>+0.99</sup> <sub>-0.82</sub>
EC 10500-1358	-8.40 <sup>+0.10</sup> <sub>-0.20</sub>	-4.20 <sup>+1.10</sup> <sub>-1.50</sub>	3.50 <sup>+1.20</sup> <sub>-0.90</sub>	5.46 <sup>+1.93</sup> <sub>-1.38</sub>	68.7 <sup>+15.6</sup> <sub>-13.8</sub>	55.1 <sup>+17.6</sup> <sub>-13.3</sub>	224 <sup>+53</sup> <sub>-41</sub>	0.04 <sup>+2.77</sup> <sub>-2.80</sub>	-4.16 <sup>+2.23</sup> <sub>-1.21</sub>
PG 1511+367	-6.90 <sup>+0.20</sup> <sub>-0.10</sub>	1.90 <sup>+0.30</sup> <sub>-0.30</sub>	3.60 <sup>+0.70</sup> <sub>-0.50</sub>	4.27 <sup>+0.72</sup> <sub>-0.63</sub>	23.5 <sup>+20.8</sup> <sub>-22.7</sub>	20.5 <sup>+2.6</sup> <sub>-2.2</sub>	256 <sup>+32</sup> <sub>-28</sub>	-10.22 <sup>+0.71</sup> <sub>-0.98</sub>	0.37 <sup>+0.99</sup> <sub>-0.77</sub>

Continued on next page

Table A.3 – continued from previous page

Name	X (kpc)	Y (kpc)	Z (kpc)	d (kpc)	Age (Myr)	$t_{\text{flight}}$ (Myr)	$v_{\text{ejec}}$ (km s <sup>-1</sup> )	$X_0$ (kpc)	$Y_0$ (kpc)
EC 20011-5005	-1.40 <sup>+2.50</sup> <sub>-1.90</sub>	-1.30 <sup>+0.40</sup> <sub>-0.50</sub>	-4.20 <sup>+1.20</sup> <sub>-1.60</sub>	7.87 <sup>+3.12</sup> <sub>-2.24</sub>	16.2 <sup>+31.1</sup> <sub>-16.2</sub>	34.7 <sup>+17.2</sup> <sub>-8.3</sub>	274 <sup>+37</sup> <sub>-33</sub>	4.81 <sup>+3.69</sup> <sub>-1.59</sub>	-3.18 <sup>+1.99</sup> <sub>-2.24</sub>
BD -15 115	-8.30 <sup>+0.00</sup> <sub>-0.10</sub>	1.00 <sup>+0.20</sup> <sub>-0.20</sub>	-4.60 <sup>+0.70</sup> <sub>-0.90</sub>	4.73 <sup>+0.87</sup> <sub>-0.72</sub>	25.4 <sup>+5.1</sup> <sub>-3.9</sub>	30.4 <sup>+2.7</sup> <sub>-2.6</sub>	249 <sup>+48</sup> <sub>-35</sub>	-1.78 <sup>+1.42</sup> <sub>-1.24</sub>	-3.77 <sup>+0.68</sup> <sub>-0.63</sub>
PG 2219+094	-6.30 <sup>+0.30</sup> <sub>-0.30</sub>	5.60 <sup>+1.00</sup> <sub>-0.90</sub>	-4.60 <sup>+0.70</sup> <sub>-0.90</sub>	7.42 <sup>+1.37</sup> <sub>-1.11</sub>	25.3 <sup>+4.7</sup> <sub>-4.0</sub>	39.3 <sup>+11.9</sup> <sub>-7.7</sub>	200 <sup>+58</sup> <sub>-40</sub>	-14.07 <sup>+2.57</sup> <sub>-3.97</sub>	2.28 <sup>+2.62</sup> <sub>-2.69</sub>
HS 1914+7139	-10.50 <sup>+0.40</sup> <sub>-0.40</sub>	10.60 <sup>+1.80</sup> <sub>-1.50</sub>	4.80 <sup>+0.80</sup> <sub>-0.70</sub>	11.87 <sup>+1.95</sup> <sub>-1.71</sub>	22.7 <sup>+9.2</sup> <sub>-11.7</sub>	58.3 <sup>+54.5</sup> <sub>-26.6</sub>	212 <sup>+175</sup> <sub>-84</sub>	-6.37 <sup>+8.60</sup> <sub>-7.78</sub>	-2.60 <sup>+8.02</sup> <sub>-12.79</sub>
PG 0855+294	-13.80 <sup>+1.50</sup> <sub>-2.10</sub>	-1.70 <sup>+0.40</sup> <sub>-0.60</sub>	4.90 <sup>+1.80</sup> <sub>-1.20</sub>	7.81 <sup>+2.80</sup> <sub>-1.99</sub>	34.6 <sup>+8.7</sup> <sub>-7.5</sub>	24.1 <sup>+3.8</sup> <sub>-3.1</sub>	278 <sup>+92</sup> <sub>-62</sub>	-16.03 <sup>+2.68</sup> <sub>-3.98</sub>	-2.99 <sup>+1.07</sup> <sub>-0.68</sub>
PG 0955+291	-11.60 <sup>+0.90</sup> <sub>-1.10</sub>	-1.30 <sup>+0.30</sup> <sub>-0.40</sub>	4.90 <sup>+1.40</sup> <sub>-1.30</sub>	6.14 <sup>+1.87</sup> <sub>-1.51</sub>	85.5 <sup>+28.4</sup> <sub>-25.7</sub>	78.2 <sup>+48.0</sup> <sub>-20.3</sub>	277 <sup>+41</sup> <sub>-39</sub>	8.27 <sup>+11.26</sup> <sub>-4.92</sub>	-1.67 <sup>+2.58</sup> <sub>-1.76</sub>
PG 2229+099	-6.50 <sup>+0.50</sup> <sub>-0.40</sub>	6.00 <sup>+2.00</sup> <sub>-1.50</sub>	-5.10 <sup>+1.30</sup> <sub>-1.70</sub>	7.98 <sup>+2.70</sup> <sub>-1.92</sub>	34.5 <sup>+11.6</sup> <sub>-20.5</sub>	63.1 <sup>+43.8</sup> <sub>-19.6</sub>	178 <sup>+72</sup> <sub>-38</sub>	-3.35 <sup>+4.23</sup> <sub>-5.05</sub>	-7.05 <sup>+5.02</sup> <sub>-9.05</sub>
PG 1610+239	-4.00 <sup>+0.70</sup> <sub>-0.60</sub>	3.40 <sup>+0.60</sup> <sub>-0.50</sub>	5.20 <sup>+0.90</sup> <sub>-0.70</sub>	7.45 <sup>+1.34</sup> <sub>-1.15</sub>	62.1 <sup>+13.0</sup> <sub>-10.4</sub>	42.0 <sup>+29.6</sup> <sub>-13.1</sub>	212 <sup>+38</sup> <sub>-23</sub>	-8.65 <sup>+2.50</sup> <sub>-5.20</sub>	-3.56 <sup>+3.71</sup> <sub>-6.95</sub>
PG 2111+023	-2.40 <sup>+0.80</sup> <sub>-0.80</sub>	7.50 <sup>+1.20</sup> <sub>-1.10</sub>	-5.30 <sup>+0.70</sup> <sub>-0.90</sub>	10.86 <sup>+1.76</sup> <sub>-1.50</sub>	81.0 <sup>+16.3</sup> <sub>-13.1</sub>	186.6 <sup>+44.2</sup> <sub>-61.0</sub>	241 <sup>+29</sup> <sub>-35</sub>	-6.58 <sup>+3.33</sup> <sub>-5.11</sub>	-5.09 <sup>+3.78</sup> <sub>-2.30</sub>
PG 0009+036	-8.90 <sup>+0.20</sup> <sub>-0.30</sub>	3.50 <sup>+1.10</sup> <sub>-0.90</sub>	-5.60 <sup>+1.40</sup> <sub>-1.90</sub>	6.67 <sup>+2.16</sup> <sub>-1.65</sub>	34.2 <sup>+17.7</sup> <sub>-33.3</sub>	40.5 <sup>+20.3</sup> <sub>-10.7</sub>	256 <sup>+60</sup> <sub>-40</sub>	-5.91 <sup>+3.72</sup> <sub>-2.66</sub>	-9.95 <sup>+4.16</sup> <sub>-8.64</sub>
PG 0122+214	-12.50 <sup>+0.70</sup> <sub>-0.80</sub>	4.70 <sup>+0.90</sup> <sub>-0.70</sub>	-5.60 <sup>+0.80</sup> <sub>-1.00</sub>	8.62 <sup>+1.55</sup> <sub>-1.29</sub>	34.5 <sup>+7.6</sup> <sub>-6.3</sub>	39.9 <sup>+7.0</sup> <sub>-5.4</sub>	156 <sup>+30</sup> <sub>-21</sub>	-12.93 <sup>+1.77</sup> <sub>-1.97</sub>	-3.39 <sup>+2.02</sup> <sub>-2.14</sub>
SB 357	-7.50 <sup>+0.10</sup> <sub>-0.10</sub>	-0.80 <sup>+0.10</sup> <sub>-0.20</sub>	-5.90 <sup>+0.80</sup> <sub>-1.10</sub>	6.02 <sup>+1.03</sup> <sub>-0.89</sub>	6.1 <sup>+8.1</sup> <sub>-5.9</sub>	53.3 <sup>+8.0</sup> <sub>-6.5</sub>	198 <sup>+46</sup> <sub>-26</sub>	-5.42 <sup>+1.72</sup> <sub>-1.96</sub>	-6.64 <sup>+2.01</sup> <sub>-2.06</sub>
EC 04420-1908	-14.70 <sup>+2.00</sup> <sub>-2.70</sub>	-5.10 <sup>+1.50</sup> <sub>-2.10</sub>	-6.20 <sup>+1.90</sup> <sub>-2.50</sub>	10.44 <sup>+4.35</sup> <sub>-3.16</sub>	68.6 <sup>+47.6</sup> <sub>-26.0</sub>	29.3 <sup>+17.6</sup> <sub>-8.6</sub>	257 <sup>+94</sup> <sub>-54</sub>	-11.43 <sup>+4.13</sup> <sub>-4.97</sub>	-7.40 <sup>+4.29</sup> <sub>-4.29</sub>
PG 1332+137	-6.20 <sup>+0.60</sup> <sub>-0.40</sub>	-0.60 <sup>+0.20</sup> <sub>-0.20</sub>	6.30 <sup>+2.00</sup> <sub>-1.70</sub>	6.54 <sup>+2.13</sup> <sub>-1.70</sub>	58.2 <sup>+13.4</sup> <sub>-11.8</sub>	32.4 <sup>+9.8</sup> <sub>-6.9</sub>	413 <sup>+38</sup> <sub>-77</sub>	-5.35 <sup>+1.22</sup> <sub>-0.98</sub>	1.99 <sup>+4.08</sup> <sub>-2.22</sub>
EC 19596-5356	3.20 <sup>+4.00</sup> <sub>-2.90</sub>	-3.10 <sup>+0.80</sup> <sub>-1.10</sub>	-7.30 <sup>+1.90</sup> <sub>-2.60</sub>	13.81 <sup>+4.80</sup> <sub>-3.63</sub>	33.5 <sup>+16.6</sup> <sub>-19.5</sub>	29.2 <sup>+20.1</sup> <sub>-9.1</sub>	475 <sup>+74</sup> <sub>-83</sub>	-1.67 <sup>+4.41</sup> <sub>-4.01</sub>	-6.08 <sup>+4.10</sup> <sub>-6.77</sub>
PHL 346	-4.60 <sup>+0.70</sup> <sub>-0.50</sub>	3.00 <sup>+0.60</sup> <sub>-0.50</sub>	-7.30 <sup>+1.20</sup> <sub>-1.40</sub>	8.55 <sup>+1.61</sup> <sub>-1.33</sub>	21.4 <sup>+4.5</sup> <sub>-3.5</sub>	28.5 <sup>+3.7</sup> <sub>-3.1</sub>	418 <sup>+49</sup> <sub>-47</sub>	-3.89 <sup>+1.28</sup> <sub>-1.22</sub>	4.28 <sup>+2.93</sup> <sub>-2.11</sub>
PG 0914+001	-18.90 <sup>+2.90</sup> <sub>-3.50</sub>	-13.80 <sup>+3.70</sup> <sub>-4.50</sub>	10.90 <sup>+3.60</sup> <sub>-2.90</sub>	20.62 <sup>+6.74</sup> <sub>-5.28</sub>	73.8 <sup>+23.2</sup> <sub>-17.7</sub>	45.0 <sup>+61.1</sup> <sub>-18.3</sub>	369 <sup>+240</sup> <sub>-157</sub>	-14.82 <sup>+11.88</sup> <sub>-9.71</sub>	-24.72 <sup>+9.27</sup> <sub>-12.55</sub>
PG 1209+263	-11.80 <sup>+0.90</sup> <sub>-0.90</sub>	-2.90 <sup>+0.60</sup> <sub>-0.80</sub>	30.70 <sup>+7.70</sup> <sub>-7.10</sub>	30.93 <sup>+7.94</sup> <sub>-7.28</sub>	76.1 <sup>+32.6</sup> <sub>-20.1</sub>	192.6 <sup>+37.2</sup> <sub>-43.7</sub>	390 <sup>+293</sup> <sub>-100</sub>	-26.70 <sup>+35.18</sup> <sub>-66.82</sub>	-32.44 <sup>+39.87</sup> <sub>-68.29</sub>

Table A.4: Computed values for stars belonging to group B. The values shown are: the present coordinates of the star ( $X, Y, Z$ ) (in galactocentric Cartesian coordinates), the distance, the evolutionary age, the flight time, the ejection velocity and the coordinates ( $X_0, Y_0$ ) of the point of ejection in the galactic plane.

Name	$X$ (kpc)	$Y$ (kpc)	$Z$ (kpc)	$d$ (kpc)	Age (Myr)	$t_{\text{flight}}$ (Myr)	$v_{\text{ejec}}$ (km s $^{-1}$ )	$X_0$ (kpc)	$Y_0$ (kpc)
HIP 81153	-7.00 $^{+1.20}_{-0.40}$	0.20 $^{+0.20}_{-0.10}$	0.50 $^{+0.60}_{-0.20}$	1.18 $^{+1.20}_{-0.54}$	4.2 $^{+2.1}_{-4.2}$	6.8 $^{+5.3}_{-3.0}$	169 $^{+32}_{-11}$	-7.88 $^{+0.39}_{-0.09}$	-0.79 $^{+0.38}_{-0.15}$
HIP 1241	-8.10 $^{+0.10}_{-0.00}$	0.30 $^{+0.00}_{-0.10}$	-0.60 $^{+0.10}_{-0.10}$	0.64 $^{+0.16}_{-0.13}$	174.8 $^{+44.1}_{-50.8}$	29.1 $^{+2.8}_{-2.9}$	43 $^{+9}_{-8}$	-5.27 $^{+0.56}_{-0.53}$	-5.47 $^{+0.38}_{-0.34}$
HIP 28132	-9.00 $^{+0.20}_{-0.20}$	-1.10 $^{+0.20}_{-0.30}$	-0.60 $^{+0.10}_{-0.10}$	1.59 $^{+0.37}_{-0.29}$	43.5 $^{+4.3}_{-15.5}$	19.9 $^{+3.7}_{-3.0}$	58 $^{+12}_{-7}$	-6.42 $^{+0.72}_{-0.50}$	-5.55 $^{+0.86}_{-1.08}$
HIP 2702	-7.70 $^{+0.10}_{-0.10}$	-0.40 $^{+0.10}_{-0.20}$	-0.70 $^{+0.20}_{-0.30}$	0.87 $^{+0.35}_{-0.25}$	24.9 $^{+44.1}_{-24.9}$	62.6 $^{+10.3}_{-9.1}$	59 $^{+16}_{-11}$	-0.64 $^{+1.42}_{-1.45}$	-9.43 $^{+0.54}_{-0.43}$
HIP 55051	-8.10 $^{+0.00}_{-0.00}$	-0.60 $^{+0.20}_{-0.20}$	0.70 $^{+0.30}_{-0.20}$	0.92 $^{+0.41}_{-0.28}$	6.6 $^{+4.6}_{-6.6}$	6.1 $^{+0.6}_{-0.7}$	188 $^{+77}_{-52}$	-8.43 $^{+0.16}_{-0.26}$	-2.54 $^{+0.55}_{-0.71}$
HIP 114690	-7.90 $^{+0.00}_{-0.10}$	0.60 $^{+0.20}_{-0.20}$	-0.70 $^{+0.20}_{-0.30}$	0.89 $^{+0.40}_{-0.27}$	19.8 $^{+4.4}_{-4.3}$	6.9 $^{+1.5}_{-1.5}$	104 $^{+18}_{-12}$	-7.96 $^{+0.05}_{-0.03}$	-1.02 $^{+0.11}_{-0.09}$
HIP 11844	-8.30 $^{+0.00}_{-0.10}$	-0.10 $^{+0.00}_{-0.00}$	-0.80 $^{+0.10}_{-0.20}$	0.87 $^{+0.10}_{-0.09}$	175.0 $^{+27.2}_{-47.5}$	70.9 $^{+4.6}_{-4.5}$	77 $^{+7}_{-6}$	1.23 $^{+0.69}_{-0.73}$	-8.06 $^{+0.31}_{-0.25}$
HIP 16130	-8.50 $^{+0.10}_{-0.20}$	-0.30 $^{+0.10}_{-0.10}$	-0.90 $^{+0.20}_{-0.20}$	1.10 $^{+0.27}_{-0.22}$	70.3 $^{+26.2}_{-53.3}$	38.2 $^{+6.0}_{-6.0}$	71 $^{+12}_{-11}$	-3.08 $^{+1.49}_{-1.31}$	-6.30 $^{+0.52}_{-0.37}$
HIP 58046	-8.10 $^{+0.00}_{-0.10}$	-0.20 $^{+0.00}_{-0.10}$	0.90 $^{+0.30}_{-0.30}$	0.92 $^{+0.37}_{-0.27}$	1.8 $^{+87.0}_{-1.8}$	16.7 $^{+3.5}_{-3.1}$	86 $^{+26}_{-19}$	-7.75 $^{+0.10}_{-0.09}$	-4.51 $^{+0.98}_{-1.23}$
BD +36 2242	-8.20 $^{+0.00}_{-0.10}$	0.10 $^{+0.00}_{-0.10}$	1.10 $^{+0.30}_{-0.20}$	1.16 $^{+0.29}_{-0.23}$	166.6 $^{+35.8}_{-32.3}$	32.3 $^{+3.9}_{-3.5}$	63 $^{+12}_{-10}$	-4.47 $^{+0.92}_{-0.77}$	-6.20 $^{+0.48}_{-0.43}$
HIP 98136	-5.50 $^{+1.00}_{-0.60}$	1.10 $^{+0.40}_{-0.30}$	-1.10 $^{+0.30}_{-0.40}$	2.98 $^{+1.11}_{-0.80}$	15.5 $^{+3.8}_{-3.3}$	21.0 $^{+2.4}_{-2.1}$	163 $^{+50}_{-45}$	-5.64 $^{+0.54}_{-0.52}$	-0.90 $^{+1.27}_{-0.94}$
HIP 111396	-7.50 $^{+0.10}_{-0.10}$	0.60 $^{+0.20}_{-0.10}$	-1.10 $^{+0.20}_{-0.30}$	1.38 $^{+0.33}_{-0.28}$	91.4 $^{+20.4}_{-17.0}$	49.2 $^{+2.9}_{-2.7}$	79 $^{+11}_{-10}$	-0.59 $^{+0.64}_{-0.64}$	-7.63 $^{+0.29}_{-0.37}$
HIP 77131	-5.50 $^{+1.20}_{-0.80}$	-0.50 $^{+0.10}_{-0.30}$	1.20 $^{+0.60}_{-0.40}$	2.79 $^{+1.39}_{-0.55}$	4.5 $^{+0.6}_{-1.5}$	17.9 $^{+1.7}_{-1.5}$	124 $^{+72}_{-41}$	-3.70 $^{+1.46}_{-1.04}$	-3.18 $^{+0.55}_{-0.38}$
HIP 113735	-7.20 $^{+0.20}_{-0.20}$	-0.50 $^{+0.10}_{-0.20}$	-1.20 $^{+0.30}_{-0.50}$	1.56 $^{+0.55}_{-0.38}$	12.5 $^{+7.3}_{-12.3}$	15.3 $^{+2.0}_{-1.3}$	168 $^{+54}_{-39}$	-5.05 $^{+0.94}_{-0.47}$	-5.63 $^{+0.32}_{-0.57}$
HIP 59955	-7.90 $^{+0.00}_{-0.10}$	-0.50 $^{+0.10}_{-0.10}$	1.40 $^{+0.40}_{-0.30}$	1.50 $^{+0.38}_{-0.30}$	76.1 $^{+15.9}_{-15.0}$	27.3 $^{+4.3}_{-4.3}$	120 $^{+28}_{-22}$	-4.31 $^{+1.37}_{-1.11}$	-4.29 $^{+0.38}_{-0.37}$
HIP 76161	-5.00 $^{+1.20}_{-0.80}$	-0.90 $^{+0.20}_{-0.40}$	1.40 $^{+0.60}_{-0.30}$	3.44 $^{+1.38}_{-0.93}$	14.0 $^{+3.9}_{-3.5}$	30.1 $^{+3.7}_{-3.1}$	109 $^{+41}_{-26}$	-1.11 $^{+0.84}_{-0.84}$	-6.12 $^{+0.53}_{-0.57}$
HIP 96130	-4.20 $^{+1.50}_{-1.00}$	0.90 $^{+0.30}_{-0.20}$	-1.40 $^{+0.30}_{-0.60}$	4.17 $^{+1.58}_{-1.11}$	14.4 $^{+1.4}_{-2.1}$	18.3 $^{+2.7}_{-2.5}$	166 $^{+92}_{-48}$	-1.44 $^{+0.96}_{-0.81}$	-2.88 $^{+0.68}_{-0.66}$
HIP 61800	-8.20 $^{+0.00}_{-0.00}$	0.20 $^{+0.00}_{-0.10}$	1.50 $^{+0.40}_{-0.30}$	1.51 $^{+0.42}_{-0.29}$	100.9 $^{+26.6}_{-24.9}$	58.2 $^{+7.9}_{-7.6}$	94 $^{+18}_{-15}$	-2.17 $^{+1.37}_{-1.34}$	-7.34 $^{+0.36}_{-0.35}$
HIP 114569	-7.50 $^{+0.10}_{-0.10}$	0.40 $^{+0.10}_{-0.10}$	-1.50 $^{+0.30}_{-0.30}$	1.60 $^{+0.40}_{-0.31}$	23.3 $^{+10.8}_{-20.0}$	7.6 $^{+0.7}_{-0.7}$	408 $^{+89}_{-71}$	-4.46 $^{+0.96}_{-0.96}$	-2.33 $^{+0.28}_{-0.34}$
HIP 11809	-9.20 $^{+0.40}_{-0.50}$	0.30 $^{+0.10}_{-0.10}$	-1.60 $^{+0.50}_{-0.60}$	2.01 $^{+0.84}_{-0.60}$	2.0 $^{+89.8}_{-2.0}$	11.6 $^{+0.8}_{-0.8}$	230 $^{+94}_{-66}$	-11.10 $^{+1.02}_{-1.43}$	-2.61 $^{+0.22}_{-0.25}$
HIP 16758	-8.10 $^{+0.00}_{-0.10}$	-1.40 $^{+0.40}_{-0.50}$	-1.60 $^{+0.40}_{-0.70}$	2.13 $^{+0.82}_{-0.57}$	13.5 $^{+3.1}_{-2.7}$	21.0 $^{+5.9}_{-4.9}$	153 $^{+19}_{-20}$	-4.23 $^{+2.59}_{-1.60}$	-4.16 $^{+0.81}_{-0.71}$
HIP 108215	-6.80 $^{+0.30}_{-0.30}$	0.40 $^{+0.10}_{-0.10}$	-1.60 $^{+0.40}_{-0.40}$	2.34 $^{+0.68}_{-0.51}$	42.6 $^{+16.3}_{-11.7}$	27.1 $^{+2.6}_{-2.2}$	256 $^{+78}_{-52}$	-1.11 $^{+0.36}_{-0.35}$	-1.98 $^{+0.84}_{-0.74}$
HIP 115347	-7.70 $^{+0.10}_{-0.10}$	0.80 $^{+0.20}_{-0.20}$	-1.60 $^{+0.40}_{-0.60}$	1.79 $^{+0.66}_{-0.47}$	18.4 $^{+4.7}_{-4.0}$	33.8 $^{+6.6}_{-5.5}$	84 $^{+19}_{-15}$	-7.66 $^{+0.40}_{-0.64}$	-5.71 $^{+0.59}_{-0.62}$
HIP 115729	-7.70 $^{+0.10}_{-0.10}$	0.70 $^{+0.20}_{-0.10}$	-1.60 $^{+0.30}_{-0.50}$	1.82 $^{+0.47}_{-0.36}$	32.9 $^{+7.4}_{-6.6}$	26.6 $^{+2.4}_{-2.4}$	88 $^{+18}_{-14}$	-5.44 $^{+0.60}_{-0.50}$	-4.75 $^{+0.29}_{-0.31}$
HIP 3812	-7.50 $^{+0.20}_{-0.10}$	-0.80 $^{+0.20}_{-0.30}$	-1.70 $^{+0.50}_{-0.60}$	1.91 $^{+0.69}_{-0.52}$	0.2 $^{+15.5}_{-0.2}$	37.2 $^{+6.8}_{-6.4}$	85 $^{+22}_{-17}$	-4.39 $^{+1.09}_{-1.02}$	-6.77 $^{+0.75}_{-0.67}$
PG 1530+212	-6.90 $^{+0.50}_{-0.30}$	0.70 $^{+0.30}_{-0.20}$	1.70 $^{+0.70}_{-0.50}$	2.15 $^{+0.89}_{-0.63}$	63.3 $^{+14.1}_{-52.8}$	37.9 $^{+8.3}_{-8.0}$	139 $^{+49}_{-37}$	-1.97 $^{+2.26}_{-2.14}$	-8.71 $^{+1.48}_{-1.92}$
HIP 79649	-7.90 $^{+0.10}_{-0.00}$	1.90 $^{+0.70}_{-0.50}$	1.90 $^{+0.60}_{-0.50}$	2.70 $^{+0.98}_{-0.70}$	18.3 $^{+4.0}_{-3.6}$	28.7 $^{+5.0}_{-4.2}$	89 $^{+18}_{-15}$	-6.89 $^{+0.37}_{-0.31}$	-4.47 $^{+0.52}_{-0.64}$
HIP 12320	-9.70 $^{+0.50}_{-0.80}$	0.50 $^{+0.10}_{-0.20}$	-2.00 $^{+0.60}_{-0.90}$	2.72 $^{+1.15}_{-0.79}$	72.8 $^{+29.4}_{-72.5}$	47.6 $^{+10.4}_{-9.4}$	105 $^{+38}_{-25}$	-2.76 $^{+2.13}_{-1.77}$	-6.27 $^{+0.80}_{-0.72}$
HIP 109051	-6.80 $^{+0.50}_{-0.30}$	1.20 $^{+0.40}_{-0.30}$	-2.00 $^{+0.50}_{-0.70}$	2.63 $^{+0.92}_{-0.67}$	19.9 $^{+4.8}_{-6.1}$	21.1 $^{+3.3}_{-3.2}$	123 $^{+27}_{-17}$	-6.03 $^{+0.85}_{-0.66}$	-3.87 $^{+0.44}_{-0.49}$
HIP 111563	-7.10 $^{+0.50}_{-0.20}$	0.90 $^{+0.50}_{-0.30}$	-2.00 $^{+0.50}_{-1.00}$	2.40 $^{+1.10}_{-0.70}$	9.4 $^{+3.5}_{-2.8}$	15.8 $^{+1.8}_{-1.7}$	223 $^{+86}_{-62}$	-7.22 $^{+0.31}_{-0.19}$	0.10 $^{+1.83}_{-0.96}$

Continued on next page

Table A.4 – continued from previous page

Name	X (kpc)	Y (kpc)	Z (kpc)	d (kpc)	Age (Myr)	$t_{\text{flight}}$ (Myr)	$v_{\text{ejec}}$ (km s <sup>-1</sup> )	$X_0$ (kpc)	$Y_0$ (kpc)
HIP 13800	-9.80 <sup>+0.30</sup> <sub>-0.50</sub>	0.00 <sup>+0.10</sup> <sub>-0.00</sub>	-2.20 <sup>+0.40</sup> <sub>-0.60</sub>	2.89 <sup>+0.75</sup> <sub>-0.60</sub>	47.7 <sup>+10.6</sup> <sub>-8.3</sub>	59.5 <sup>+5.3</sup> <sub>-4.9</sub>	145 <sup>+41</sup> <sub>-31</sub>	-2.02 <sup>+1.13</sup> <sub>-1.07</sub>	-5.88 <sup>+1.02</sup> <sub>-0.72</sub>
HIP 48394	-9.90 <sup>+0.50</sup> <sub>-0.90</sub>	0.80 <sup>+0.30</sup> <sub>-0.30</sub>	2.20 <sup>+1.10</sup> <sub>-0.60</sub>	3.07 <sup>+1.39</sup> <sub>-0.91</sub>	21.4 <sup>+5.2</sup> <sub>-9.9</sub>	25.4 <sup>+4.7</sup> <sub>-4.1</sub>	122 <sup>+41</sup> <sub>-29</sub>	-9.27 <sup>+1.32</sup> <sub>-1.32</sub>	-3.05 <sup>+0.79</sup> <sub>-0.58</sub>
HIP 107027	-6.20 <sup>+0.70</sup> <sub>-0.50</sub>	1.30 <sup>+0.40</sup> <sub>-0.40</sub>	-2.20 <sup>+0.60</sup> <sub>-0.90</sub>	3.15 <sup>+1.20</sup> <sub>-0.83</sub>	16.2 <sup>+1.2</sup> <sub>-2.3</sub>	23.7 <sup>+7.8</sup> <sub>-5.3</sub>	181 <sup>+34</sup> <sub>-22</sub>	-9.43 <sup>+0.67</sup> <sub>-1.64</sub>	-1.63 <sup>+1.19</sup> <sub>-0.49</sub>
HIP 1904	-7.60 <sup>+0.10</sup> <sub>-0.10</sub>	-0.20 <sup>+0.00</sup> <sub>-0.10</sub>	-2.30 <sup>+0.50</sup> <sub>-0.60</sub>	2.32 <sup>+0.69</sup> <sub>-0.51</sub>	46.2 <sup>+18.8</sup> <sub>-13.2</sub>	57.6 <sup>+3.9</sup> <sub>-3.9</sub>	164 <sup>+45</sup> <sub>-31</sub>	-0.12 <sup>+0.65</sup> <sub>-0.70</sub>	-5.10 <sup>+0.93</sup> <sub>-0.71</sub>
HIP 55461	-8.50 <sup>+0.10</sup> <sub>-0.20</sub>	-1.10 <sup>+0.30</sup> <sub>-0.30</sub>	2.40 <sup>+0.80</sup> <sub>-0.60</sub>	2.64 <sup>+0.90</sup> <sub>-0.67</sub>	54.2 <sup>+20.1</sup> <sub>-27.7</sub>	29.9 <sup>+9.1</sup> <sub>-7.1</sub>	145 <sup>+38</sup> <sub>-24</sub>	-6.79 <sup>+0.80</sup> <sub>-0.50</sub>	-4.39 <sup>+0.50</sup> <sub>-0.42</sub>
HIP 112790	-7.10 <sup>+0.10</sup> <sub>-0.10</sub>	1.20 <sup>+0.10</sup> <sub>-0.20</sub>	-2.40 <sup>+0.40</sup> <sub>-0.30</sub>	2.84 <sup>+0.33</sup> <sub>-0.44</sub>	60.3 <sup>+12.0</sup> <sub>-9.3</sub>	170.1 <sup>+49.6</sup> <sub>-48.3</sub>	169 <sup>+11</sup> <sub>-18</sub>	-19.89 <sup>+5.53</sup> <sub>-6.20</sub>	-14.23 <sup>+2.16</sup> <sub>-2.14</sub>
HIP 59067	-8.10 <sup>+0.10</sup> <sub>-0.00</sub>	-0.90 <sup>+0.20</sup> <sub>-0.20</sub>	2.60 <sup>+0.60</sup> <sub>-0.50</sub>	2.75 <sup>+0.65</sup> <sub>-0.52</sub>	72.7 <sup>+3.2</sup> <sub>-8.6</sub>	39.2 <sup>+3.5</sup> <sub>-3.8</sub>	234 <sup>+59</sup> <sub>-46</sub>	-1.73 <sup>+1.28</sup> <sub>-1.25</sub>	-3.24 <sup>+1.00</sup> <sub>-0.67</sub>
BD +20 3004	-6.70 <sup>+0.40</sup> <sub>-0.20</sub>	0.50 <sup>+0.20</sup> <sub>-0.10</sub>	2.90 <sup>+0.80</sup> <sub>-0.60</sub>	3.23 <sup>+0.90</sup> <sub>-0.63</sub>	71.0 <sup>+19.2</sup> <sub>-17.7</sub>	18.8 <sup>+1.2</sup> <sub>-1.4</sub>	247 <sup>+67</sup> <sub>-46</sub>	-2.70 <sup>+1.38</sup> <sub>-1.13</sub>	-2.65 <sup>+0.37</sup> <sub>-0.29</sub>
HIP 105912	-5.20 <sup>+1.20</sup> <sub>-0.70</sub>	0.70 <sup>+0.30</sup> <sub>-0.20</sub>	-3.00 <sup>+0.80</sup> <sub>-1.20</sub>	4.17 <sup>+1.70</sup> <sub>-1.14</sub>	12.8 <sup>+4.1</sup> <sub>-3.3</sub>	15.3 <sup>+0.7</sup> <sub>-0.6</sub>	457 <sup>+130</sup> <sub>-133</sub>	-2.48 <sup>+1.59</sup> <sub>-1.15</sub>	0.71 <sup>+1.52</sup> <sub>-1.07</sub>
HIP 45904	-11.10 <sup>+0.80</sup> <sub>-1.20</sub>	0.60 <sup>+0.30</sup> <sub>-0.10</sub>	3.10 <sup>+1.10</sup> <sub>-0.80</sub>	4.42 <sup>+1.66</sup> <sub>-1.15</sub>	15.4 <sup>+3.1</sup> <sub>-2.9</sub>	24.8 <sup>+4.3</sup> <sub>-3.7</sub>	240 <sup>+71</sup> <sub>-54</sub>	-10.20 <sup>+0.98</sup> <sub>-1.55</sub>	-0.25 <sup>+2.16</sup> <sub>-1.19</sub>
HIP 37903	-13.10 <sup>+1.70</sup> <sub>-2.60</sub>	2.30 <sup>+1.20</sup> <sub>-0.80</sub>	3.20 <sup>+1.70</sup> <sub>-1.10</sub>	6.42 <sup>+3.36</sup> <sub>-2.11</sub>	19.1 <sup>+8.9</sup> <sub>-6.7</sub>	26.4 <sup>+8.1</sup> <sub>-5.8</sub>	279 <sup>+123</sup> <sub>-80</sub>	-8.83 <sup>+1.21</sup> <sub>-1.64</sub>	-0.04 <sup>+3.54</sup> <sub>-1.60</sub>
HIP 70275	-5.40 <sup>+0.90</sup> <sub>-0.60</sub>	-1.10 <sup>+0.30</sup> <sub>-0.30</sub>	3.20 <sup>+1.10</sup> <sub>-0.80</sub>	4.26 <sup>+1.48</sup> <sub>-1.08</sub>	15.1 <sup>+3.5</sup> <sub>-3.8</sub>	38.3 <sup>+38.4</sup> <sub>-15.8</sub>	271 <sup>+7</sup> <sub>-8</sub>	-13.65 <sup>+2.95</sup> <sub>-8.48</sub>	-2.59 <sup>+0.85</sup> <sub>-0.56</sub>
BD -2 3766	-5.90 <sup>+0.80</sup> <sub>-0.50</sub>	-1.00 <sup>+0.20</sup> <sub>-0.40</sub>	3.50 <sup>+1.30</sup> <sub>-0.90</sub>	4.22 <sup>+1.50</sup> <sub>-1.10</sub>	15.2 <sup>+3.0</sup> <sub>-3.0</sub>	14.8 <sup>+1.2</sup> <sub>-1.3</sub>	425 <sup>+151</sup> <sub>-109</sub>	-3.82 <sup>+1.54</sup> <sub>-1.13</sub>	-8.13 <sup>+1.74</sup> <sub>-2.45</sub>
PB 5418	-7.90 <sup>+0.00</sup> <sub>-0.10</sub>	3.80 <sup>+1.20</sup> <sub>-1.00</sub>	-4.80 <sup>+1.20</sup> <sub>-1.60</sub>	6.09 <sup>+2.03</sup> <sub>-1.49</sub>	24.6 <sup>+7.5</sup> <sub>-15.0</sub>	16.5 <sup>+2.8</sup> <sub>-2.3</sub>	415 <sup>+141</sup> <sub>-100</sub>	-5.18 <sup>+1.58</sup> <sub>-1.06</sub>	1.13 <sup>+2.16</sup> <sub>-1.38</sub>
HIP 56322	-8.60 <sup>+0.20</sup> <sub>-0.30</sub>	-2.90 <sup>+0.90</sup> <sub>-1.40</sub>	5.30 <sup>+2.70</sup> <sub>-1.70</sub>	6.09 <sup>+3.17</sup> <sub>-1.92</sub>	9.2 <sup>+2.1</sup> <sub>-2.2</sub>	13.1 <sup>+3.4</sup> <sub>-2.8</sub>	471 <sup>+189</sup> <sub>-99</sub>	-7.21 <sup>+0.76</sup> <sub>-0.38</sub>	-8.13 <sup>+2.96</sup> <sub>-5.46</sub>
Ton S 308	-10.60 <sup>+0.70</sup> <sub>-0.90</sub>	-2.00 <sup>+0.50</sup> <sub>-0.70</sub>	-5.90 <sup>+1.50</sup> <sub>-2.00</sub>	6.76 <sup>+2.24</sup> <sub>-1.69</sub>	33.0 <sup>+10.3</sup> <sub>-18.9</sub>	47.9 <sup>+14.6</sup> <sub>-10.6</sub>	169 <sup>+43</sup> <sub>-24</sub>	-7.36 <sup>+3.37</sup> <sub>-3.14</sub>	-8.84 <sup>+2.24</sup> <sub>-3.35</sub>
PHL 2018	-5.10 <sup>+1.10</sup> <sub>-0.70</sub>	1.80 <sup>+0.60</sup> <sub>-0.40</sub>	-6.00 <sup>+1.50</sup> <sub>-2.10</sub>	6.93 <sup>+2.39</sup> <sub>-1.77</sub>	26.6 <sup>+5.7</sup> <sub>-5.3</sub>	24.4 <sup>+4.8</sup> <sub>-3.7</sub>	399 <sup>+68</sup> <sub>-66</sub>	-5.90 <sup>+1.11</sup> <sub>-0.92</sub>	4.21 <sup>+4.72</sup> <sub>-2.64</sub>
HIP 52906	-11.60 <sup>+0.70</sup> <sub>-0.80</sub>	-0.10 <sup>+0.00</sup> <sub>-0.10</sub>	6.80 <sup>+1.60</sup> <sub>-1.40</sub>	7.72 <sup>+1.85</sup> <sub>-1.53</sub>	25.3 <sup>+5.4</sup> <sub>-4.4</sub>	90.6 <sup>+46.6</sup> <sub>-23.8</sub>	277 <sup>+25</sup> <sub>-31</sub>	16.67 <sup>+16.54</sup> <sub>-8.09</sub>	-10.62 <sup>+2.44</sup> <sub>-4.90</sub>



# Bibliography

- H. A. Abt, H. Levato, and M. Grosso. Rotational Velocities of B Stars. *ApJ*, 573: 359–365, July 2002. doi: 10.1086/340590.
- C. Allen and T. Kinman. Young Stars far from the Galactic Plane: Runaways from Clusters. In C. Allen and C. Scarfe, editors, *RevMexAA (SC)*, volume 21 of *RevMexAA (SC)*, pages 121–127, August 2004.
- C. Allen and A. Santillan. An improved model of the galactic mass distribution for orbit computations. *RevMexAA*, 22:255–263, October 1991.
- R. J. Allison, S. P. Goodwin, R. J. Parker, R. de Grijs, S. F. Portegies Zwart, and M. B. N. Kouwenhoven. Dynamical Mass Segregation on a Very Short Timescale. *ApJL*, 700:L99–L103, August 2009. doi: 10.1088/0004-637X/700/2/L99.
- L. H. Amaral and J. R. D. Lepine. A self-consistent model of the spiral structure of the Galaxy. *MNRAS*, 286:885–894, April 1997.
- E. B. Amôres, J. R. D. Lépine, and Y. N. Mishurov. The corotation gap in the Galactic HI distribution. *MNRAS*, 400:1768–1774, December 2009. doi: 10.1111/j.1365-2966.2009.15611.x.
- S. M. Andrievsky, D. Schönberner, and J. S. Drilling. Blue stragglers in open clusters. Part II. *A&A*, 356:517–528, April 2000.
- B. B. Behr. Rotation Velocities of Red and Blue Field Horizontal-Branch Stars. *ApJS*, 149:101–121, November 2003a. doi: 10.1086/378352.
- B. B. Behr. Chemical Abundances and Rotation Velocities of Blue Horizontal-Branch Stars in Six Globular Clusters. *ApJS*, 149:67–99, November 2003b. doi: 10.1086/377509.
- B. B. Behr. Chemical Abundances Along the Horizontal Branch. In T. G. Barnes, III and F. N. Bash, editors, *Cosmic Abundances as Records of Stellar Evolution and Nucleosynthesis*, volume 336 of *ASP Conf. Ser.*, page 131, September 2005.
- J. Binney and S. Tremaine. *Galactic Dynamics: Second Edition*. Princeton University Press, 2008.
- J. Binney, O. Gerhard, and D. Spergel. The photometric structure of the inner Galaxy. *MNRAS*, 288:365–374, June 1997.

- A. Blaauw. On the origin of the O- and B-type stars with high velocities (the "run-away" stars), and some related problems. *BAIN*, 15:265, May 1961.
- H. E. Bond. The uBVI Photometric System. I. Motivation, Implementation, and Calibration. *AJ*, 129:2914–2923, June 2005. doi: 10.1086/430052.
- J. Brand and L. Blitz. The Velocity Field of the Outer Galaxy. *A&A*, 275:67, August 1993.
- A. Bressan, F. Fagotto, G. Bertelli, and C. Chiosi. Evolutionary sequences of stellar models with new radiative opacities. II -  $Z = 0.02$ . *A&AS*, 100:647–664, September 1993.
- W. R. Brown, M. J. Geller, S. J. Kenyon, M. J. Kurtz, and B. C. Bromley. Hyper-velocity Stars. II. The Bound Population. *ApJ*, 660:311–318, May 2007a. doi: 10.1086/513595.
- W. R. Brown, M. J. Geller, S. J. Kenyon, M. J. Kurtz, and B. C. Bromley. Hyper-velocity Stars. III. The Space Density and Ejection History of Main-Sequence Stars from the Galactic Center. *ApJ*, 671:1708–1716, December 2007b. doi: 10.1086/523642.
- G. Cescutti, F. Matteucci, P. François, and C. Chiappini. Abundance gradients in the Milky Way for  $\alpha$  elements, iron peak elements, barium, lanthanum, and europium. *A&A*, 462:943–951, February 2007. doi: 10.1051/0004-6361:20065403.
- E. S. Conlon, P. J. F. Brown, P. L. Dufton, and F. P. Keenan. An abundance and kinematical analysis of four early-type high latitude stars. *A&A*, 200:168–174, July 1988.
- E. S. Conlon, P. J. F. Brown, P. L. Dufton, and F. P. Keenan. Peculiar and normal early-type stars in the galactic halo. *A&A*, 224:65–72, October 1989.
- E. S. Conlon, P. L. Dufton, F. P. Keenan, and P. J. T. Leonard. The run-away nature of distant early-type stars in the galactic halo. *A&A*, 236:357–361, September 1990.
- E. S. Conlon, P. L. Dufton, F. P. Keenan, R. J. H. McCausland, and D. Holmgren. The origin of distant B-type stars in the galactic halo. *ApJ*, 400:273–279, November 1992. doi: 10.1086/171994.
- A. N. Cox. *Allen's astrophysical quantities*. 2000.
- M. Creze, E. Chereul, O. Bienayme, and C. Pichon. The distribution of nearby stars in phase space mapped by Hipparcos. I. The potential well and local dynamical mass. *A&A*, 329:920–936, January 1998.
- R. de la Fuente Marcos and C. de la Fuente Marcos. On the recent star formation history of the Milky Way disk. *NewA*, 9:475–502, July 2004. doi: 10.1016/j.newast.2004.02.004.

- W. Dehnen and J. J. Binney. Local stellar kinematics from HIPPARCOS data. *MNRAS*, 298:387–394, August 1998.
- W. S. Dias and J. R. D. Lépine. Direct Determination of the Spiral Pattern Rotation Speed of the Galaxy. *ApJ*, 629:825–831, August 2005. doi: 10.1086/431456.
- B. Dorman, R. T. Rood, and R. W. O’Connell. Ultraviolet Radiation from Evolved Stellar Populations. I. Models. *ApJ*, 419:596, December 1993. doi: 10.1086/173511.
- R. Drimmel and D. N. Spergel. Three-dimensional Structure of the Milky Way Disk: The Distribution of Stars and Dust beyond  $0.35R_{\text{solar}}$ . *ApJ*, 556:181–202, July 2001. doi: 10.1086/321556.
- F. Eisenhauer, R. Schödel, R. Genzel, T. Ott, M. Tecza, R. Abuter, A. Eckart, and T. Alexander. A Geometric Determination of the Distance to the Galactic Center. *ApJL*, 597:L121–L124, November 2003. doi: 10.1086/380188.
- S. Ekström, G. Meynet, A. Maeder, and F. Barblan. Evolution towards the critical limit and the origin of Be stars. *A&A*, 478:467–485, February 2008. doi: 10.1051/0004-6361:20078095.
- F. Elias, J. Cabrera-Caño, and E. J. Alfaro. OB Stars in the Solar Neighborhood. I. Analysis of their Spatial Distribution. *AJ*, 131:2700–2709, June 2006. doi: 10.1086/503110.
- D. M. Elmegreen and B. G. Elmegreen. Inner two-arm symmetry in spiral galaxies. *ApJ*, 445:591–598, June 1995. doi: 10.1086/175723.
- D. S. Evans. The Revision of the General Catalogue of Radial Velocities. In A. H. Batten & J. F. Heard, editor, *Determination of Radial Velocities and their Applications*, volume 30 of *IAU Symposium*, page 57, 1967.
- J. Fabregat and J. M. Torrejón. On the evolutionary status of Be stars. *A&A*, 357:451–459, May 2000.
- F. Fagotto, A. Bressan, G. Bertelli, and C. Chiosi. Evolutionary sequences of stellar models with new radiative opacities. IV.  $Z=0.004$  and  $Z=0.008$ . *A&AS*, 105:29–38, May 1994.
- M. Feast and P. Whitelock. Galactic kinematics of Cepheids from HIPPARCOS proper motions. *MNRAS*, 291:683, November 1997.
- D. Fernández, F. Figueras, and J. Torra. Kinematics of young stars. II. Galactic spiral structure. *A&A*, 372:833–850, June 2001. doi: 10.1051/0004-6361:20010366.
- M. Fich, L. Blitz, and A. A. Stark. The rotation curve of the Milky Way to  $2R(0)$ . *ApJ*, 342:272–284, July 1989. doi: 10.1086/167591.

- P. J. Flower. Transformations from Theoretical Hertzsprung-Russell Diagrams to Color-Magnitude Diagrams: Effective Temperatures, B-V Colors, and Bolometric Corrections. *ApJ*, 469:355, September 1996. doi: 10.1086/177785.
- Y. Frémat, J. Zorec, A.-M. Hubert, and M. Floquet. Effects of gravitational darkening on the determination of fundamental parameters in fast-rotating B-type stars. *A&A*, 440:305–320, September 2005. doi: 10.1051/0004-6361:20042229.
- K. Fuhrmann. Nearby stars of the Galactic disk and halo. III. *Astronomische Nachrichten*, 325:3–80, January 2004. doi: 10.1002/asna.200310173.
- O. Gerhard. Pattern speeds in the Milky Way. *ArXiv e-prints*, March 2010.
- D. R. Gies and C. T. Bolton. The binary frequency and origin of the OB runaway stars. *ApJS*, 61:419–454, June 1986. doi: 10.1086/191118.
- T. M. Girard, D. I. Dinescu, W. F. van Altena, I. Platais, D. G. Monet, and C. E. López. The Southern Proper Motion Program. III. A Near-Complete Catalog to  $V=17.5$ . *AJ*, 127:3060–3071, May 2004. doi: 10.1086/383545.
- L. Girardi, A. Bressan, G. Bertelli, and C. Chiosi. Low-mass stars evolutionary tracks & isochrones (Girardi+, 2000). *VizieR Online Data Catalog*, 414:10371, November 2000.
- R. F. Green, M. Schmidt, and J. Liebert. The Palomar-Green catalog of ultraviolet-excess stellar objects. *ApJS*, 61:305–352, June 1986. doi: 10.1086/191115.
- J. L. Greenstein and A. I. Sargent. The Nature of Faint Blue Stars in the Halo. II. *ApJS*, 28:157, November 1974.
- A. Gualandris and S. Portegies Zwart. A hypervelocity star from the Large Magellanic Cloud. *MNRAS*, 376:L29–L33, March 2007. doi: 10.1111/j.1745-3933.2007.00280.x.
- V. V. Gvaramadze. HD271791: dynamical versus binary-supernova ejection scenario. *MNRAS*, 395:L85–L89, May 2009. doi: 10.1111/j.1745-3933.2009.00648.x.
- V. V. Gvaramadze, A. Gualandris, and S. Portegies Zwart. On the origin of high-velocity runaway stars. *MNRAS*, 396:570–578, June 2009. doi: 10.1111/j.1365-2966.2009.14809.x.
- N. C. Hambly, K. D. Wood, F. P. Keenan, et al. A search for star formation around the Galactic halo B-type star PHL 346. *A&A*, 306:119, February 1996.
- N. C. Hambly, W. R. J. Rolleston, F. P. Keenan, P. L. Dufton, and R. A. Safer. Early-Type Stars in the Galactic Halo from the Palomar-Green Survey. I. A Sample of Evolved, Low-Mass Stars. *ApJS*, 111:419, August 1997. doi: 10.1086/313024.

- N. C. Hambly, A. C. Davenhall, M. J. Irwin, and H. T. MacGillivray. The SuperCOSMOS Sky Survey - III. Astrometry. *MNRAS*, 326:1315–1327, October 2001. doi: 10.1046/j.1365-8711.2001.04662.x.
- R. B. Hanson, A. R. Klemola, B. F. Jones, and D. G. Monet. Lick NPM2 Catalog (Hanson+ 2003). *VizieR Online Data Catalog*, 1283, May 2003.
- R. B. Hanson, A. R. Klemola, B. F. Jones, and D. G. Monet. Lick Northern Proper Motion Program. III. Lick NPM2 Catalog. *AJ*, 128:1430–1445, September 2004. doi: 10.1086/423041.
- B. Hauck and M. Mermilliod. Uvbybeta photoelectric photometric catalogue. *A&AS*, 129:431–433, May 1998.
- U. Heber, K. Hunger, G. Jonas, and R. P. Kudritzki. The atmosphere of subluminescent B stars. *A&A*, 130:119–130, January 1984.
- U. Heber, S. Moehler, and D. Groote. HS 1914+7139: a rapidly rotating massive B-star far away from the galactic plane. *A&A*, 303:L33+, November 1995.
- U. Heber, H. Edelmann, R. Napiwotzki, M. Altmann, and R.-D. Scholz. The B-type giant HD 271791 in the Galactic halo. Linking run-away stars to hyper-velocity stars. *A&A*, 483:L21–L24, May 2008. doi: 10.1051/0004-6361:200809767.
- J. G. Hills. Hyper-velocity and tidal stars from binaries disrupted by a massive Galactic black hole. *Nat*, 331:687–689, February 1988. doi: 10.1038/331687a0.
- D. Hoffleit and C. —. Jaschek. *The Bright star catalogue*. 1991.
- E. Høg, C. Fabricius, V. V. Makarov, et al. The Tycho-2 catalogue of the 2.5 million brightest stars. *A&A*, 355:L27–L30, March 2000.
- J. Holmberg and C. Flynn. The local density of matter mapped by Hipparcos. *MNRAS*, 313:209–216, April 2000. doi: 10.1046/j.1365-8711.2000.02905.x.
- J. Holmberg and C. Flynn. The local surface density of disc matter mapped by Hipparcos. *MNRAS*, 352:440–446, August 2004. doi: 10.1111/j.1365-2966.2004.07931.x.
- R. Hoogerwerf, J. H. J. de Bruijne, and P. T. de Zeeuw. On the origin of the O and B-type stars with high velocities. II. Runaway stars and pulsars ejected from the nearby young stellar groups. *A&A*, 365:49–77, January 2001. doi: 10.1051/0004-6361:20000014.
- I. Iben, Jr. Single and binary star evolution. *ApJS*, 76:55–114, May 1991. doi: 10.1086/191565.

- A. Irrgang, N. Przybilla, U. Heber, M. Fernanda Nieva, and S. Schuh. The Nature of the Hyper-Runaway Candidate Hip 60350. *ApJ*, 711:138–143, March 2010. doi: 10.1088/0004-637X/711/1/138.
- C. Jordi, E. Høg, A. G. A. Brown, L. Lindegren, C. A. L. Bailer-Jones, J. M. Carrasco, J. Knude, V. Straižys, J. H. J. de Bruijne, J.-F. Claeskens, R. Drimmel, F. Figueras, M. Grenon, I. Kolka, M. A. C. Perryman, G. Tautvaišienė, V. Vansevičius, P. G. Willemsen, A. Bridžius, D. W. Evans, C. Fabricius, M. Fiorucci, U. Heiter, T. A. Kaempf, A. Kazlauskas, A. Kučinskas, V. Mal'uyto, U. Munari, C. Reylé, J. Torra, A. Vallenari, K. Zdanavičius, R. Korakitis, O. Malkov, and A. Smette. The design and performance of the Gaia photometric system. *MNRAS*, 367:290–314, March 2006. doi: 10.1111/j.1365-2966.2005.09944.x.
- C. Jordi, M. Gebran, J. M. Carrasco, J. de Bruijne, H. Voss, C. Fabricius, J. Knude, A. Vallenari, R. Kohley, and A. Mora. Gaia broad band photometry. *A&A*, 523:A48+, November 2010. doi: 10.1051/0004-6361/201015441.
- M. Jurić, Ž. Ivezić, A. Brooks, R. H. Lupton, D. Schlegel, D. Finkbeiner, N. Padmanabhan, N. Bond, B. Sesar, C. M. Rockosi, G. R. Knapp, J. E. Gunn, T. Sumi, D. P. Schneider, J. C. Barentine, H. J. Brewington, J. Brinkmann, M. Fukugita, M. Harvanek, S. J. Kleinman, J. Krzesinski, D. Long, E. H. Nielsen, Jr., A. Nitta, S. A. Snedden, and D. G. York. The Milky Way Tomography with SDSS. I. Stellar Number Density Distribution. *ApJ*, 673:864–914, February 2008. doi: 10.1086/523619.
- A. J. Kalnajs. Spiral Structure Viewed as a Density Wave. *Proceedings of the Astronomical Society of Australia*, 2:174, October 1973.
- D. K. Karimova and E. D. Pavlovskaya. O-Star Kinematics. *Soviet Astronomy*, 28:40, February 1984.
- F. P. Keenan and P. L. Dufton. On the nature of early-type stars in the galactic halo. *MNRAS*, 205:435–445, October 1983.
- F. P. Keenan, P. L. Dufton, and C. D. McKeith. Atmospheric parameters and chemical compositions of eighteen halo OB stars. *MNRAS*, 200:673–685, August 1982.
- F. P. Keenan, P. J. F. Brown, and D. J. Lennon. Observations of early-type stars at high galactic latitudes. *A&A*, 155:333–338, February 1986.
- J. Kilian. Chemical abundances in early B-type stars. IV - He, CNO, and Si abundances. *A&A*, 262:171–187, August 1992.
- J. Kilian. Chemical abundances in early B-type stars. 5: Metal abundances and LTE/NLTE comparison. *A&A*, 282:867–873, February 1994.

- D. Kilkenny. High Latitude Blue Stars. In B. Warner, editor, *Variable Stars and Galaxies, in honor of M. W. Feast on his retirement*, volume 30 of *Astronomical Society of the Pacific Conference Series*, page 97, 1992.
- R. J. Klement. Halo streams in the solar neighborhood. *A&ARv*, 18:567–594, October 2010. doi: 10.1007/s00159-010-0034-0.
- K. Kuijken and G. Gilmore. The mass distribution in the galactic disc. I - A technique to determine the integral surface mass density of the disc near the sun. *MNRAS*, 239:571–603, August 1989.
- K. Kuijken and G. Gilmore. The galactic disk surface mass density and the Galactic force  $K(z)$  at  $Z = 1.1$  kiloparsecs. *ApJL*, 367:L9–L13, January 1991. doi: 10.1086/185920.
- R. L. Kurucz. Model atmospheres for G, F, A, B, and O stars. *ApJS*, 40:1–340, May 1979. doi: 10.1086/190589.
- E. M. Leitch and G. Vasisht. Mass extinctions and the sun’s encounters with spiral arms. *NewA*, 3:51–56, February 1998. doi: 10.1016/S1384-1076(97)00044-4.
- P. J. T. Leonard. The maximum possible velocity of dynamically ejected runaway stars. *AJ*, 101:562–571, February 1991. doi: 10.1086/115704.
- P. J. T. Leonard. Mechanisms for Ejecting Stars from the Galactic Plane. In D. D. Sasselov, editor, *Luminous High-Latitude Stars*, volume 45 of *ASP Conf. Ser.*, page 360, January 1993.
- P. J. T. Leonard and R. J. Dewey. Montecarlo Simulations of the Supernova Ejection Mechanism for the Runaway Stars. In D. D. Sasselov, editor, *Luminous High-Latitude Stars*, volume 45 of *ASP Conf. Ser.*, page 239, January 1993.
- P. J. T. Leonard and M. J. Duncan. Runaway stars from young star clusters containing initial binaries. II - A mass spectrum and a binary energy spectrum. *AJ*, 99:608–616, February 1990. doi: 10.1086/115354.
- J. R. D. Lépine, A. Roman-Lopes, Z. Abraham, T. C. Junqueira, and Y. N. Mishurov. The spiral structure of the Galaxy revealed by CS sources and evidence for the 4:1 resonance. *MNRAS*, page 477, April 2011. doi: 10.1111/j.1365-2966.2011.18492.x.
- R. S. Levenhagen and N. V. Leister. Spectroscopic analysis of southern B and Be stars. *MNRAS*, 371:252–262, September 2006. doi: 10.1111/j.1365-2966.2006.10655.x.
- C. C. Lin and F. H. Shu. On the Spiral Structure of Disk Galaxies. *ApJ*, 140:646, August 1964. doi: 10.1086/147955.

- L. Lindegren. Gaia: Astrometric performance and current status of the project. In S. A. Klioner, P. K. Seidelmann, & M. H. Soffel, editor, *IAU Symposium*, volume 261 of *IAU Symposium*, pages 296–305, January 2010. doi: 10.1017/S1743921309990548.
- T. E. Lutz and D. H. Kelker. On the Use of Trigonometric Parallaxes for the Calibration of Luminosity Systems: Theory. *PASP*, 85:573, October 1973. doi: 10.1086/129506.
- B. B. Lynn, F. P. Keenan, P. L. Dufton, R. A. Saffer, W. R. J. Rolleston, and J. V. Smoker. Early-type stars in the Galactic halo from the Palomar-Green survey-III. Completion of a magnitude range limited sample. *MNRAS*, 349:821–832, April 2004a. doi: 10.1111/j.1365-2966.2004.07493.x.
- B. B. Lynn, F. P. Keenan, P. L. Dufton, et al. High-resolution spectroscopic observations of B-type stars from the Edinburgh-Cape Survey - III. Completion of a magnitude range limited survey. *MNRAS*, 353:633–638, September 2004b. doi: 10.1111/j.1365-2966.2004.08091.x.
- A. Maeder and G. Meynet. The Evolution of Rotating Stars. *ARA&A*, 38:143–190, 2000. doi: 10.1146/annurev.astro.38.1.143.
- H. R. M. Magee, P. L. Dufton, F. P. Keenan, et al. Rotational velocities of B-type stars from the Edinburgh-Cape survey. *A&A*, 338:85–90, October 1998.
- H. R. M. Magee, P. L. Dufton, F. P. Keenan, W. R. J. Rolleston, D. Kilkenny, D. O’Donoghue, C. Koen, and R. S. Stobie. Model atmosphere and kinematical analyses of early-type stars from the Edinburgh-Cape Survey. *MNRAS*, 324:747–756, June 2001. doi: 10.1046/j.1365-8711.2001.04367.x.
- D. J. Majaess, D. G. Turner, and D. J. Lane. Characteristics of the Galaxy according to Cepheids. *MNRAS*, 398:263–270, September 2009. doi: 10.1111/j.1365-2966.2009.15096.x.
- S. R. Majewski. Galactic structure surveys and the evolution of the Milky Way. *ARA&A*, 31:575–638, 1993. doi: 10.1146/annurev.aa.31.090193.003043.
- L. S. Marochnik. On the origin of the solar system and the exceptional position of the sun in the galaxy. *Ap&SS*, 89:61–75, January 1983. doi: 10.1007/BF01008385.
- J. C. Martin. The Masses of the B Stars in the High Galactic Latitude Eclipsing Binary IT Librae. *PASP*, 115:49–58, January 2003. doi: 10.1086/345433.
- J. C. Martin. The Origins and Evolutionary Status of B Stars Found Far from the Galactic Plane. I. Composition and Spectral Features. *AJ*, 128:2474–2500, November 2004. doi: 10.1086/425045.

- J. C. Martin. The Origins and Evolutionary Status of B Stars Found Far from the Galactic Plane. II. Kinematics and Full Sample Analysis. *AJ*, 131:3047–3068, June 2006. doi: 10.1086/504079.
- M. V. McSwain and D. R. Gies. The Evolutionary Status of Be Stars: Results from a Photometric Study of Southern Open Clusters. *ApJS*, 161:118–146, November 2005. doi: 10.1086/432757.
- M. Miyamoto and Z. Zhu. Galactic Interior Motions Derived from HIPPARCOS Proper Motions. I. Young Disk Population. *AJ*, 115:1483–1491, April 1998. doi: 10.1086/300292.
- S. Moehler, A. V. Sweigart, W. B. Landsman, and U. Heber. Hot HB stars in globular clusters - Physical parameters and consequences for theory — V. Radiative levitation versus helium mixing. *A&A*, 360:120–132, August 2000.
- D. G. Monet, S. E. Levine, B. Canzian, et al. The USNO-B Catalog. *AJ*, 125:984–993, February 2003. doi: 10.1086/345888.
- T. T. Moon and M. M. Dworetzky. Grids for the determination of effective temperature and surface gravity of B, A and F stars using uvby-beta photometry. *MNRAS*, 217:305–315, November 1985.
- C. J. Mooney, W. R. J. Rolleston, F. P. Keenan, D. J. Pinfield, D. L. Pollacco, P. L. Dufton, and A. C. Katsiyannis. Strömgren uvby photometry of B-type stars from the Palomar-Green Survey. *A&A*, 357:553–556, May 2000.
- R. Napiwotzki. Spectroscopic investigation of old planetaries. V. Distance scales. *A&A*, 367:973–982, March 2001. doi: 10.1051/0004-6361:20000431.
- R. Napiwotzki, D. Schönberner, and V. Wenske. On the determination of effective temperature and surface gravity of B, A, and F stars using Stromgren UVBY beta photometry. *A&A*, 268:653–666, February 1993.
- J.F.C. Neves. *Simulations of High-mass Star Formation in the Milky Way*. PhD thesis, University of Hertfordshire, Hatfield, UK, 2009.
- M. Odenkirchen and P. Brosche. Orbits of galactic globular clusters. *Astronomische Nachrichten*, 313:69–81, March 1992.
- R. P. Olling and W. Dehnen. The Oort Constants Measured from Proper Motions. *ApJ*, 599:275–296, December 2003. doi: 10.1086/379278.
- H. B. Perets. Runaway and Hypervelocity Stars in the Galactic Halo: Binary Rejuvenation and Triple Disruption. *ApJ*, 698:1330–1340, June 2009. doi: 10.1088/0004-637X/698/2/1330.
- A. Pietrinferni, S. Cassisi, M. Salaris, and F. Castelli. A Large Stellar Evolution Database for Population Synthesis Studies. I. Scaled Solar Models and Isochrones. *ApJ*, 612:168–190, September 2004. doi: 10.1086/422498.

- S. F. Portegies Zwart. The Characteristics of High-Velocity O and B Stars Which Are Ejected from Supernovae in Binary Systems. *ApJ*, 544:437–442, November 2000. doi: 10.1086/317190.
- A. Poveda, J. Ruiz, and C. Allen. Run-away Stars as the Result of the Gravitational Collapse of Proto-stellar Clusters. *Boletín de los Observatorios Tonantzintla y Tacubaya*, 4:86–90, April 1967.
- N. Przybilla, M. F. Nieva, U. Heber, and K. Butler. HD 271791: An Extreme Supernova Runaway B Star Escaping from the Galaxy. *ApJL*, 684:L103–L106, September 2008. doi: 10.1086/592245.
- M. Ramspeck, U. Heber, and H. Edelmann. Early type stars at high galactic latitudes. II. Four evolved B-type stars of unusual chemical composition. *A&A*, 379:235–244, November 2001a. doi: 10.1051/0004-6361:20011334.
- M. Ramspeck, U. Heber, and S. Moehler. Early type stars at high galactic latitudes. I. Ten young massive B-type stars. *A&A*, 378:907–917, November 2001b. doi: 10.1051/0004-6361:20011246.
- M. J. Reid. The distance to the center of the Galaxy. *ARA&A*, 31:345–372, 1993. doi: 10.1146/annurev.aa.31.090193.002021.
- M. J. Reid, A. C. S. Readhead, R. C. Vermeulen, and R. N. Treuhaft. The Proper Motion of Sagittarius A\*. I. First VLBA Results. *ApJ*, 524:816–823, October 1999. doi: 10.1086/307855.
- A. C. Robin, C. Reylé, S. Derrière, and S. Picaud. A synthetic view on structure and evolution of the Milky Way. *A&A*, 409:523–540, October 2003. doi: 10.1051/0004-6361:20031117.
- A. C. Robin, R. M. Rich, H. Aussel, P. Capak, L. A. M. Tasca, K. Jahnke, Y. Kakazu, J.-P. Kneib, A. Koekemoer, A. C. Leauthaud, S. Lilly, B. Mobasher, N. Scoville, Y. Taniguchi, and D. J. Thompson. The Stellar Content of the COSMOS Field as Derived from Morphological and SED-based Star/Galaxy Separation. *ApJS*, 172:545–559, September 2007. doi: 10.1086/516600.
- H. J. Rocha-Pinto, J. Scalo, W. J. Maciel, and C. Flynn. An Intermittent Star Formation History in a “Normal” Disk Galaxy: The Milky Way. *ApJL*, 531: L115–L118, March 2000. doi: 10.1086/312531.
- W. R. J. Rolleston, N. C. Hambly, P. L. Dufton, et al. High-resolution spectroscopic observations of B-type stars from the Edinburgh-Cape survey. *MNRAS*, 290:422–430, September 1997.
- W. R. J. Rolleston, N. C. Hambly, F. P. Keenan, P. L. Dufton, and R. A. Saffer. Early-type stars in the Galactic halo from the Palomar-Green Survey II: A sample of distant, apparently young Population I stars. *A&A*, 347:69–76, July 1999.

- D. Russeil. Star-forming complexes and the spiral structure of our Galaxy. *A&A*, 397:133–146, January 2003. doi: 10.1051/0004-6361:20021504.
- R. A. Saffer, F. P. Keenan, N. C. Hambly, P. L. Dufton, and J. Liebert. A Large-Scale Spectroscopic Survey of Early-Type Stars at High Galactic Latitudes. *ApJ*, 491:172, December 1997. doi: 10.1086/304930.
- S. E. Sale, J. E. Drew, C. Knigge, et al. The structure of the outer Galactic disc as revealed by IPHAS early A stars. *MNRAS*, 402:713–723, February 2010. doi: 10.1111/j.1365-2966.2009.15746.x.
- G. Schaller, D. Schaerer, G. Meynet, and A. Maeder. New grids of stellar models from 0.8 to 120 solar masses at  $Z = 0.020$  and  $Z = 0.001$ . *A&AS*, 96:269–331, December 1992.
- D. J. Schlegel, D. P. Finkbeiner, and M. Davis. Maps of Dust Infrared Emission for Use in Estimation of Reddening and Cosmic Microwave Background Radiation Foregrounds. *ApJ*, 500:525, June 1998. doi: 10.1086/305772.
- D. Schönberner. Asymptotic giant branch evolution with steady mass loss. *A&A*, 79:108–114, October 1979.
- D. Schönberner and R. Napiwotzki. The interior structure and evolution of blue straggler stars in open clusters. *A&A*, 282:106–114, February 1994.
- D. Schönberner, S. M. Andrievsky, and J. S. Drilling. Blue stragglers in open clusters. III. NGC 7789. *A&A*, 366:490–497, February 2001. doi: 10.1051/0004-6361:20000213.
- R. Schönrich, J. Binney, and W. Dehnen. Local kinematics and the local standard of rest. *MNRAS*, 403:1829–1833, April 2010. doi: 10.1111/j.1365-2966.2010.16253.x.
- M. D. V. Silva and R. Napiwotzki. Ejection velocities of high Galactic latitude runaway stars. *MNRAS*, 411:2596–2614, March 2011. doi: 10.1111/j.1365-2966.2010.17864.x.
- H. Smith, Jr. The calibration problem. IV - The Lutz-Kelker correction. *A&A*, 188:233–238, December 1987.
- M. C. Smith, G. R. Ruchti, A. Helmi, R. F. G. Wyse, J. P. Fulbright, K. C. Freeman, J. F. Navarro, G. M. Seabroke, M. Steinmetz, M. Williams, O. Bienaymé, J. Binney, J. Bland-Hawthorn, W. Dehnen, B. K. Gibson, G. Gilmore, E. K. Grebel, U. Munari, Q. A. Parker, R.-D. Scholz, A. Siebert, F. G. Watson, and T. Zwitter. The RAVE survey: constraining the local Galactic escape speed. *MNRAS*, 379:755–772, August 2007. doi: 10.1111/j.1365-2966.2007.11964.x.
- D. R. Soderblom. The Ages of Stars. *ARA&A*, 48:581–629, September 2010. doi: 10.1146/annurev-astro-081309-130806.

- R. S. Stobie, D. Kilkenny, D. O'Donoghue, et al. The Edinburgh-Cape Blue Object Survey - I. Description of the survey. *MNRAS*, 287:848–866, June 1997.
- R. C. Stone. Kinematics, close binary evolution, and ages of the O stars. *ApJ*, 232:520–530, September 1979. doi: 10.1086/157311.
- R. C. Stone. The space frequency and origin of the runaway O and B stars. *AJ*, 102:333–349, July 1991. doi: 10.1086/115880.
- B. Strömgren. Spectral Classification Through Photoelectric Narrow-Band Photometry. *ARA&A*, 4:433, 1966. doi: 10.1146/annurev.aa.04.090166.002245.
- W. Tobin. The faint, apparently-normal, high-latitude B stars - What might they be, and what observations are needed? In A. G. D. Philip, D. S. Hayes, and J. W. Liebert, editors, *IAU Colloq. 95: Second Conference on Faint Blue Stars*, pages 149–158, 1987.
- A. Toomre. Theories of spiral structure. *ARA&A*, 15:437–478, 1977. doi: 10.1146/annurev.aa.15.090177.002253.
- J. P. Vallee. The Milky Way's Spiral Arms Traced by Magnetic Fields, Dust, Gas, and Stars. *ApJ*, 454:119, November 1995. doi: 10.1086/176470.
- J. P. Vallée. New Velocimetry and Revised Cartography of the Spiral Arms in the Milky WAY — A Consistent Symbiosis. *AJ*, 135:1301–1310, April 2008. doi: 10.1088/0004-6256/135/4/1301.
- F. van Leeuwen. Validation of the new Hipparcos reduction. *A&A*, 474:653–664, November 2007. doi: 10.1051/0004-6361:20078357.
- V. Wenske and D. Schönberner. Influence of rotation on the stellar parameters. In W. W. Weiss and A. Baglin, editors, *IAU Colloq. 137: Inside the Stars*, volume 40 of *ASP Conf. Ser.*, page 162, January 1993.
- T. N. G. Westin. The local system of early type stars - Spatial extent and kinematics. *A&AS*, 60:99–134, April 1985.
- M. I. Wilkinson and N. W. Evans. The present and future mass of the Milky Way halo. *MNRAS*, 310:645–662, December 1999. doi: 10.1046/j.1365-8711.1999.02964.x.
- X. X. Xue, H. W. Rix, G. Zhao, et al. The Milky Way's Circular Velocity Curve to 60 kpc and an Estimate of the Dark Matter Halo Mass from the Kinematics of ~2400 SDSS Blue Horizontal-Branch Stars. *ApJ*, 684:1143–1158, September 2008. doi: 10.1086/589500.
- C. Yuan. Application of the Density-Wave Theory to the Spiral Structure of the Milky way System. II. Migration of Stars. *ApJ*, 158:889, December 1969. doi: 10.1086/150249.

- 
- N. Zacharias, S. E. Urban, M. I. Zacharias, G. L. Wycoff, D. M. Hall, D. G. Monet, and T. J. Rafferty. The Second US Naval Observatory CCD Astrograph Catalog (UCAC2). *AJ*, 127:3043–3059, May 2004. doi: 10.1086/386353.